AlCr(Si,B)N – Design and Performance of Quaternary Nitride Coatings

Doctoral Thesis

Dipl.-Ing. Christian Tritremmel

being a thesis in partial fulfillment of the requirements for the degree of a

Doctor of Montanistic Sciences (Dr.mont.)

Leoben, July 2013

This thesis was supported by the Christian Doppler Research Association in the framework of the Christian Doppler Laboratory for Advanced Hard Coatings at the Department of Physical Metallurgy and Materials Testing at the Montanuniversität Leoben, Austria, in cooperation with Plansee Composite Materials GmbH in Lechbruck, Germany, and OC Oerlikon Balzers AG in Balzers, Principality of Liechtenstein.

Affidavit

I declare in lieu of oath, that I wrote this thesis and performed the associated research myself, using only literature cited in this volume.

Leoben, July 2013

Acknowledgements

My sincerest gratitude is due to my supervisor Christian Mitterer, head of the Chair of Functional Materials and Material Systems, who give me the opportunity to carry out this work and for his support and guidance throughout the whole project. I am grateful to the opportunity to have experienced you as wonderful boss and teacher.

I am also very grateful to my scientific supervisor and friend Rostislav, supporting me with his advice, patience and encouragement. Beside your scientific expertise, I would like to say a big thank you for your friendship.

I also want to express my gratitude and appreciation to Paul Mayrhofer, who gave me scientific support and encouragement. Thank you for spending a lot of time in answering my questions.

Furthermore, I would like to thank our project partners Plansee and Oerlikon Balzers, in particular Peter Polcik and Conrad Polzer as well as Markus Lechthaler and Helmut Rudigier.

Special thanks to all people from the Thin Film Group, including Angelika, Anna, Corinna, David, Doris, Jörg, Manfred, Marisa, Max, Michael, Nina, Oliver, Richard, Robert F., Robert H., Sabrina, Stephan, Tom, Veli and Vicky, it was a great time working with you.

I am very thankful to the staff and all the friends at the Department of Physical Metallurgy and Material Testing for their support.

Inexpressible thanks to my family who motivated and encouraged me during the whole time. Without their trust and support it would not have been possible to reach the goal.

Contents

1 Introduction

One of the most important inventions of mankind is the automobile. It allows us to cover long distances much faster and in a more convenient manner. Nowadays, life without automobile is hardly to imagine for human race, since almost everybody uses any kind of engine-driven locomotion in daily grind. However, the ever increasing demand on engines with higher power-output and increased longevity on the one side, and reduced fuel consumption associated with lower CO_2 emission on the other side, forces industry and scientists to develop and design materials with outstanding properties.

A critical and important point to improve material performance is the surface condition, since any interaction between two bodies occurs via their surfaces. Hence, surface modifications are needed to fulfill the requirements for special technical applications (e.g., automotive and metal cutting/forming industry). One possibility is the deposition of thin films or coatings on bulk materials (substrates) like high-speed tool steels or cemented carbides. The benefit of film deposition is the possibility to combine coating and substrate materials with often very different properties, e.g. a tough base material coated with a hard film. This thesis focuses on hard and wear resistant coatings applied to cutting and metal forming tools, which are of particular importance for manufacturing in the automotive industry.

There are two main deposition techniques to produce such protective coatings, namely chemical vapor deposition (CVD) and physical vapor deposition (PVD), both utilize condensation from the vapor phase. The CVD process is typically accomplished at high temperatures (~1000 °C), uses one or more volatile precursors, which react and synthesize a solid coating on the substrate. PVD techniques use solid state source materials, which enter the gas phase via physical mechanisms and condense on the substrate. In this thesis, a PVD technique was used, more precisely the cathodic arc evaporation method, to synthesize thin films.

Hard coatings, often used as a protective layer for cutting tools, are characterized by high hardness and wear resistance, good thermal stability and increased oxidation resistance. The first hard coatings developed were binary nitrides and carbides such as TiN, CrN and TiC. Over the years, tool lifetime has dramatically improved due to the development of ternary nitride coatings like TiAlN and AlCrN. However, higher

hardness and improved cutting performance of these coatings are accompanied with a higher level of residual stress. Hence, the adhesion to the substrate is reduced, which leads to spalling of the entire film under applied loads. An alternative to counter this problem seems, however, to be synthesis of film materials having nanocomposite or multilayer structure. Nanocomposite films are of increasing interest due to the possibility to synthesize materials with unique structure resulting in outstanding properties like superhardness, toughness and/or increased wear resistance. In the case of multilayers, alternating layers with different composition and a layer thickness down to a few nanometers result in improved film properties such as high hardness or increased toughness. Moreover, the ever increasing demand on films for high-temperature applications like severe cutting processes stimulate the development of advanced metal nitride films with nanocomposite and/or multilayer structure, resulting in outstanding properties. Nevertheless, since there is a variety of different industrial applications, it will be impossible to develop a single coating for all fields of operation. Hence, a large number of different coatings with properties tailored according to the individual application is necessary to fulfill the requirements demanded by industry.

The focus of this thesis is laid on the correlation between synthesis, structure and morphology, and properties of Al-Cr-N based hard coatings. All coatings were synthesized by means of cathodic arc evaporation using an industrial scale deposition plant from Oerlikon Balzers. Based on AlCrN reference coatings with Al/Cr ratios from 1 to 2.3, two different alloying elements, i.e. Si or B, were added. Al-Cr-Si and Al-Cr-B cathodes with Si contents between 5 and 20 at.% and B in the range of 10 to 30 at.% have been manufactured powder-metallurgically and supplied by Plansee Composite Materials. Si is known to improve hardness and oxidation resistance of transition metal nitrides (MeN) films. Due to limited solubility of Si in various MeN's, the addition of Si causes a pronounced grain refinement and densification of the overall coating structure based on the formation of a dense, amorphous SiN_x grain boundary phase. In the case of B addition, similar to Si, a nanocomposite structure is formed, revealing enhanced mechanical and tribological properties. Moreover, the influence of ion energy (i.e. substrate bias voltage) on structure and mechanical properties was intensively studied. The most promising Al-Cr-B-N films were used to deposit a multilayer structure with Ti-Al-N layers.

The first chapters in this thesis give an overview on the theoretical background of film synthesis and growth as well as the characterization techniques used with regard to the investigated films. Subsequent to a short summary of the main findings, the major experimental research is presented and comprehensively discussed in four publications.

2 Selection of material in engineering applications

The following chapter gives an overview of available literature concerning the base materials. Moreover, recent findings on the influence of Si and B in transition metal nitride coatings as well as the impact of multilayer architecture on mechanical and tribological properties are provided.

2.1 Bulk coarse-grained polycrystalline materials

There is only a small group of commercial used materials consisting of a single crystal, like e.g. diamonds for jewelery, sapphire in medical engineering, silicon in the semiconductor industry, superalloys for turbine blades, etc. However, in general, conventional materials are composed of a large number of crystallites (steels, cemented carbides, intermetallics …). In general, steels are classified in non-alloyed and alloyed as well as construction and tool steels [1]. Non-alloyed steels, for example, contain beside carbon only traces of Si, Mn, Al and Ti.

On the other hand, tool steels, which are used to manufacture tools and molds to form and machine other materials, show improved mechanical and thermal properties fostered by the alloying technology and the high standards in their production. Tool steels possess a complex microstructure consisting of the metallic matrix with precipitates within and embedded in the matrix. The grain size of the tempered martensite (former austenite matrix) is in the range of several microns, whereas the precipitates in the metallic matrix (secondary hardening carbides, intermetallic phases) have a size of 1 to 50 nm [2]. In contrast, particles embedded in the metallic matrix exhibit a size typically from 0.1 to 100 µm. In general, the mechanical, thermal and tribological properties of tool steels are influenced by the martensite grain size and internal defects (dislocations, point defects) and by the volume, size and shape of the precipitates. This kind of steels can be manufactured via the conventional route by means of melting, solidification, hot forging, annealing, machining and the final heat treatment [3]. Another possibility to produce tool steels is found in powder metallurgy. This technology allows the production of a fine grained metallic powder with a uniform distribution of carbides, facilitated by the rapid solidification during gas atomization by using high pressure nitrogen [3]. The resulting powder is then bonded to near net shape by means of hot isostatic pressing (HIP)

with almost full achievable density.

Another kind of materials used in the metal cutting and forming industry are the so called cemented carbides, which consist of hard carbide particles and a metallic binder phase. In general, the hard phase is tungsten carbide (WC), having a proportion between 70 and 96% of the total weight of the composite, and Cobalt (Co) is used as binder [4]. An increased Co content results in higher toughness and bending strength, however, simultaneously hardness and Young's modulus diminish. Cemented carbides are produced by means of mixture of the individual powders, pressing to the corresponding shape and the subsequent sintering process. They are characterized by an average grain size between 0.5 and 10 µm and reveal increased wear resistance with respect to conventional steel.

2.2 Limits of bulk materials in applications

Bulk materials such as tool steels and cemented carbides are exposed to a variety of damage mechanisms during application (turning, milling …), which reveal the limits of usage. Tools are often subjected to high mechanical loads and therefore, hardness must be high enough to avoid local plastic deformation. In general, hardness of tool steels and cemented carbides is limited with ~7-10 and ~15 GPa, respectively [5]. The fatigue behavior due to repeated mechanical loading is strongly influenced by content and size of internal defects (point defects, dislocations …). Moreover, tool materials need sufficient toughness to prevent sudden fracture of the cutting edges due to local overload. In addition to the mechanical load, tools are often exposed to elevated temperatures and hence, high hot hardness and thermal stability of the microstructure is required for reasonable service life. As a consequence, tool steels are restricted to a maximum application temperature of ~600 °C, whereas cemented carbides allow usage up to 1100 °C. However, during cutting of steel the temperature in the contact area may reach values up to 1300 °C [6]. Such high temperatures cause interaction with the surrounding atmosphere, including oxidation of the tool surface. Furthermore, the increased diffusion in this temperature range contributes to faster failure of the tool. Another very important point with respect to lifetime and functional reliability is the wear behavior of tool materials. In general, bulk materials like tool steels and cemented carbides reveal a high coefficient of friction resulting in

heat generation and thus, premature tool-damaging [6]. Another unfavorable effect might be adhesion to the workpiece causing material transfer from the tool surface. The limited hardness of such bulk materials is accompanied with increased abrasive wear, thus diminishing the productivity. For that reason it is necessary to develop possibilities to increase the performance of conventional bulk materials.

2.3 Potential of novel nanostructured materials

Nanocrystalline materials are polycrystalline solids with a typical crystallite size in the order of a few nanometers (1-100 nm), whereas conventional materials (e.g. steels, cemented carbides) reveal grain sizes over a wide range from about 100 nm to several millimeters. In general, polycrystalline materials consist of two types of atoms, in particular crystal atoms with nearest neighbor configuration being placed in the lattice and boundary atoms with a variety of interatomic spacings [7]. In conventional bulk materials, the number of atoms in grains is significantly higher compared to the amount in the boundary regions. The properties and behavior of such materials are mainly affected by their grain size and consequently by the movement and pile-up of dislocations [8]. Hence, increase of the dislocation density and interaction between dislocations results in strengthening of the material [7]. In contrast, nanocrystalline materials typically contain a high fraction of grain boundaries, since the crystallite size is considerably reduced. The characteristics in these materials are strongly influenced by the processes in the boundary regions. In this case, strengthening occurs via increase of grain boundary density (grain size reduction), which inhibits the formation and movement of dislocations [9].

Nanostructured materials can be classified with respect to the chemical composition and the dimensionality of the crystallites (Fig. 2.1) [10]. Thus, they can be categorized in layer-shaped (one dimensional) crystallites, or they can be rod-shaped with a thickness of a few nanometers (two dimensional nanostructure), and they can also be composed of equiaxed crystallites (three dimensional nanostructure). Furthermore, these categories can each be separated depending on the chemical composition of the crystallites. The case of identical chemical composition of crystallites and interfacial area is the simplest one. Multilayer films are representative for nanostructured materials consisting of crystallites with different chemical composition. Another possibility is a different composition of boundary regions and

crystallites, which is characteristic in nanocomposites. Such nanostructured materials are at least composed of two different phases. They can be formed by combination of nanocrystalline (nc) and amorphous (a) phases, by composition of different nc-phases or by combining a nc-phase and a metal [7]. Another family of nanostructured materials is formed by dispersion of nanometer-sized crystallites in a matrix with different composition (e.g.Ni_3Al/Ni alloys) [10].

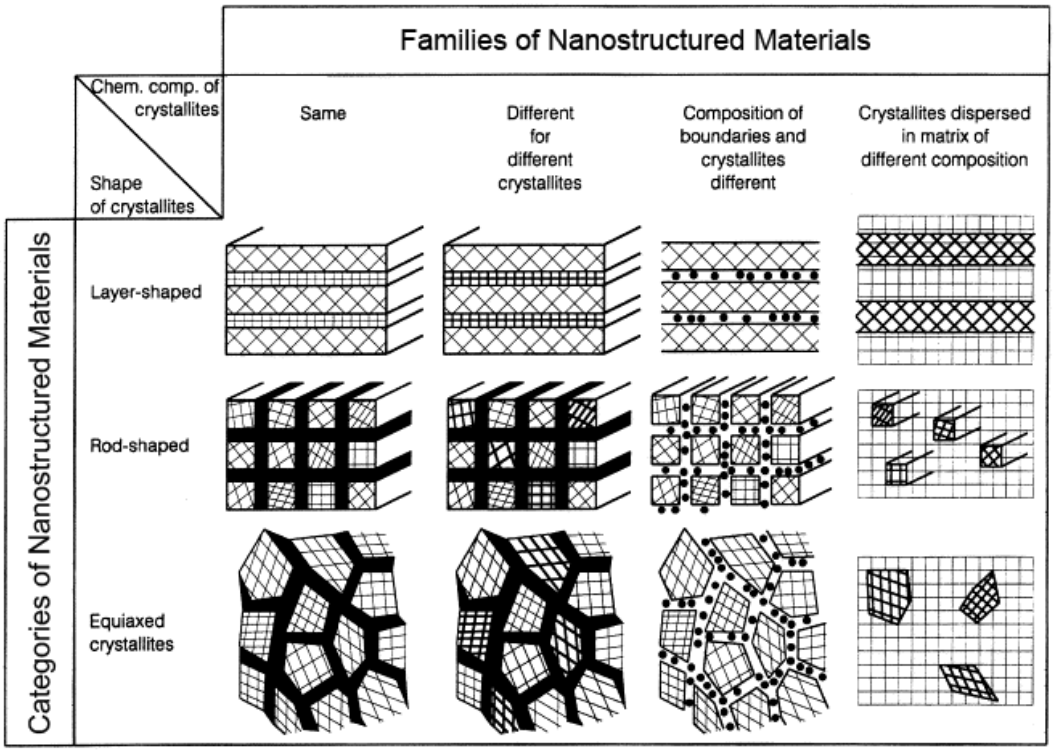

Figure 2.1: Classification of nanostructured materials with respect to their chemical composition and the shape of the crystallites [11].

In contrast to coarse-grained materials, nanocrystalline materials with the same chemical composition and a grain size of ~10 nm reveal significantly different properties, which are improved with respect to magnetic, electronic, optical, mechanical and tribological behavior [12]. Nanocrystalline materials may possess higher strength and hardness, increased toughness and wear performance than conventionally grain sized materials. The combined improvement of toughness and hardness in specific nanocomposites is attributed to the increased fraction of strong interface boundaries [7]. Moreover, the thermal stability and corrosion resistance, as well as the chemical stability is significantly improved in comparison to commercially

used materials. Hence, nanostructured materials with their novel and outstanding properties are potential candidates for applications in different fields of technology.

2.4 Plasma processing for synthesis of nanostructured materials

The production of nanostructured materials uses liquid, solid, or gas precursors, which are the base modules for the synthesis of materials at the nanoscale. The creation of these materials is implemented by means of physical compaction and chemical or physical deposition techniques. The synthesis of nanostructured materials is basically feasible via two different approaches. In the “top-down” approach, the bulk material is pulverized to particles with nanometer-sized grains and then assembled to a new bulk material. Methods for this approach are mechanical processes such as mechanical alloying, high-energy ball milling, equal channel angular pressing and high pressure torsion [12]. In the “bottom-up” approach, individual atoms or molecules agglomerate to nanoparticles. Examples for this approach are the sol-gel method (wet-chemical process) and techniques from the vapor phase including inert-gas condensation, laser beam treatment, CVD and PVD. CVD and PVD are the most widely used procedures to synthesize films with chemical composition, structure and thus, properties different to the bulk material [10]. In case of CVD techniques, thin films are deposited on the substrate surface via chemical reactions between the gaseous precursors. PVD processes controllably dislodge material from the source (target) by means of atomization or vaporization and transfer of the atoms and/or ions to the substrate, where nucleation and film growth take place. The most important PVD methods are sputtering and evaporation.

In general, the development and synthesis of nanocrystalline materials with unique properties requires methods, which ensure a high nucleation rate accompanied by a low growth rate of grains [8]. These preconditions are fulfilled when the nanocrystalline materials are produced in the form of films. Hence, plasma-assisted PVD techniques such as magnetron sputtering and cathodic arc evaporation exhibit high potential for the development of new materials with extraordinary properties. Magnetron sputtering is a process, which evaporates mainly atoms in neutral form from the target (base material of the desired coating) surface by momentum transfer from bombarding highly-energetic inert gas ions (mainly Ar^+ ions) [13]. In the cathodic

arc evaporation process, an arc is ignited on the target surface (cathode) owing to the high current densities. This arc (or more precisely the arc spot) is moving rapidly on the target surface and causes evaporation of the material mainly in the ionized state. Within this work, cathodic arc evaporation was used to synthesize nanocrystalline thin films and therefore this technique is described in more detail in section 3.1. These PVD methods allow also the control of growth mechanisms (determining grain size and crystallographic orientation of the film) via ion bombardment. In the case of ion bombardment, ions with increased energy are impinging on the growing film, resulting in heating at an atomic level. This technique is a non-equilibrium process, which restricts grain growth and allows formation of dense films (see chapter 3.2.3). These PVD techniques allow the preparation of films having a hardness 2 – 3 times higher than conventional cemented carbides [2]. Moreover, this techniques show a high flexibility in film composition and substrate materials. In addition, PVD methods provide excellent film adhesion and the substrate temperature is freely selectable between room temperature and ~600 °C.

2.5 Transition metal nitride films

Ternary metal nitride coatings were first introduced in the 1980s on the basis of the binary TiN. Incorporation of Al into the TiN lattice was found to reveal beneficial effects on their properties [14-16]. TiAlN coatings exhibit higher hardness, improved oxidation resistance and superior wear properties as compared to TiN [17-19]. Also in the case of CrN films, addition of Al results in improved mechanical and tribological properties [20, 21]. Whereas TiAlN films generally provide higher hardness values accompanied with pronounced age hardening at elevated temperatures [16, 22], AlCrN films possess significantly better oxidation resistance [23]. This behavior is attributed to the combined formation of self-passivating protective and dense Al_2O_3 and Cr_2O_3 scales [24, 25]. In contrast, TiAlN films commonly form Al_2O_3 and TiO_2 scales, where the latter one fosters increased oxidation due to the strongly disordered lattice structure [17, 26].

Another important aspect in transition metal nitrides like $Al_xCr_{1-x}N$ and $Ti_{1-x}Al_xN$ is the solubility of AlN in face-centered cubic (fcc) NaCl-like (B1) CrN and (B1) TiN, respectively. In thermodynamic equilibrium, the solubility of wurtzite (w) type AlN in the above mentioned binary nitrides is very limited. However, PVD techniques, such

as magnetron sputtering and arc evaporation (see chapter 3), allow the synthesis of metastable supersaturated $Al_xCr_{1-x}N$ and $Ti_{1-x}Al_xN$ thin films. The critical solubility of fcc AlN in these fcc transition metal nitrides is predicted with 77% and 65%, respectively [27-31]. However, the effective solubility limit depends on the used deposition technique and the process conditions, e.g. substrate bias voltage. Hence, the transition from fcc-AlCrN to w-AlCrN appears in the mole fraction range of 0.6 - 0.77 AlN, whereas in TiAlN the transition zone is found between ~0.5 and 0.65. In Fig. 2.1 the substitution of Cr and Ti atoms, respectively, with the smaller Al atoms is schematically shown. The transition zone is characterized by the simultaneous crystallization of both, fcc and wurtzite phase, before at even higher Al content the wurtzite structure is predominant.

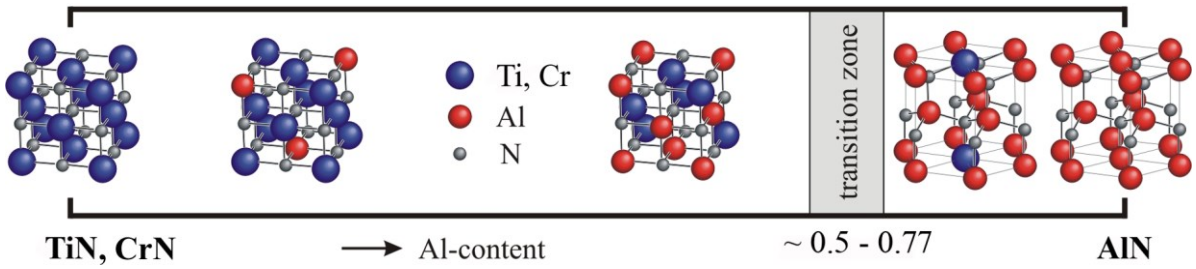

Figure 2.2: Influence of Al content on structural evolution in pseudobinary AlCrN and TiAlN hard coatings (modified after [32]).

The structural evolution in transition metal nitride films strongly affects mechanical and tribological properties as well as the oxidation behavior. In general, hardness of $Al_xCr_{1-x}N$ films is enhanced with increasing Al content. However, this improvement is limited up to a certain Al content, where the fcc B1 structure changes to wurtzite type. Within the fcc crystal structure and depending on the used measurement methods and deposition conditions, $Al_xCr_{1-x}N$ films exhibit a maximum hardness of 2500 Hk (Knoop hardness) [33] and 38 GPa (HU_{pl}) [20]. In this work, a series of $Al_xCr_{1-x}N$ films with x ~ 0.46 - 0.66 were synthesized and investigated with respect to their structure and mechanical properties. The results are presented in Publication I with hardness values from ~26 to ~30 GPa for increasing Al content.

Several authors investigated the tribological behavior of $Al_xCr_{1-x}N$ coatings in terms of coefficient of friction (COF) and wear rate [21, 33, 34]. Franz et al. reported about an

increasing COF during testing against alumina balls with rising Al content irrespective of temperature [21]. The highest COF was found at 500 °C (1.3), while similar values at RT and 700 °C (≤0.8) were observed for all $Al_xCr_{1-x}N$ coatings. Ide et al. demonstrated a reduction of the wear rate by almost two orders of magnitude for $Al_xCr_{1-x}N$ coatings as compared to $Ti_{1-x}Al_xN$ [33]. Moreover, $Al_xCr_{1-x}N$ films revealed increased tool life time in machining like cutting, turning, milling and hobbing [35].

In terms of thermal stability, $Al_xCr_{1-x}N$ coatings with fcc crystal structure reveal a higher onset temperature for N-loss (~1230 °C) with respect to Al-free CrN films [36]. In general, thermal decomposition of fcc $Al_xCr_{1-x}N$ coatings starts by precipitation of w-AlN at grain boundaries (≥850 °C, depending on the Al content), hence, the remaining fcc matrix becomes Cr-rich [20, 37]. Further increase in temperature causes breaking of the unstable Cr-N bonds and the consequential N-loss promotes the formation of hexagonal (hex) Cr_2N, which further reduces to Cr [36]. In contrast, w-AlCrN decomposes via precipitation of CrN and transforms then into Cr_2N and Cr. The oxidation resistance of CrN coatings is significantly improved by addition of Al while preserving the fcc crystal structure [20]. Banakh et al. reported about the formation of a dense corundum type mixed $(Al_xCr_{1-x})_2O_3$ oxide layer at the surface [25]. Hence, the onset of oxidation in fcc $Al_xCr_{1-x}N$ films is in the range of 1100-1150 °C depending on the Al content (see Publication II).

2.6 Effect of alloying elements on structure and properties of transition metal nitrides

Properties of transition metal nitrides like Al-Cr-N and Ti-Al-N can be improved and/or modified by addition of further alloying elements. The main driving force for addition of specific components is to improve the mechanical properties and the tribological behavior. Moreover, increase of thermal stability together with improved oxidation resistance is also a relevant reason for this approach. However, crystallographic structure and morphology are as well affected by compositional modifications.

In this thesis, the effect of Si and B addition, respectively, in the ternary Al-Cr-N coating system was investigated. The individual Al-Cr-Si-N and Al-Cr-B-N films were synthesized using powder-metallurgically produced Al-Cr-Si and Al-Cr-B compound targets (see publication I-III). Addition of Si or B to the AlCrN solid solution results in

incorporation in the fcc lattice either by substitution of Al and/or Cr atoms or by occupying interstitial sites. However, the solubility of Si and B, respectively, in the fcc AlCrN lattice is limited and thus, Si and B atoms segregate to the grain boundaries when exceeding a critical limit. There, they form with nitrogen an amorphous SiN_x or BN_x phase, respectively [22, 38, 39]. Thus, a nanocomposite structure is formed, consisting of nanocrystalline Al-Cr-(Si, B)-N grains embedded in an amorphous $(Si,B)N_x$ matrix. Patscheider et al. proposed a morphological zone model for nc-TiN/Si_3N_4 [40], which is also valid for other nanocomposite films.

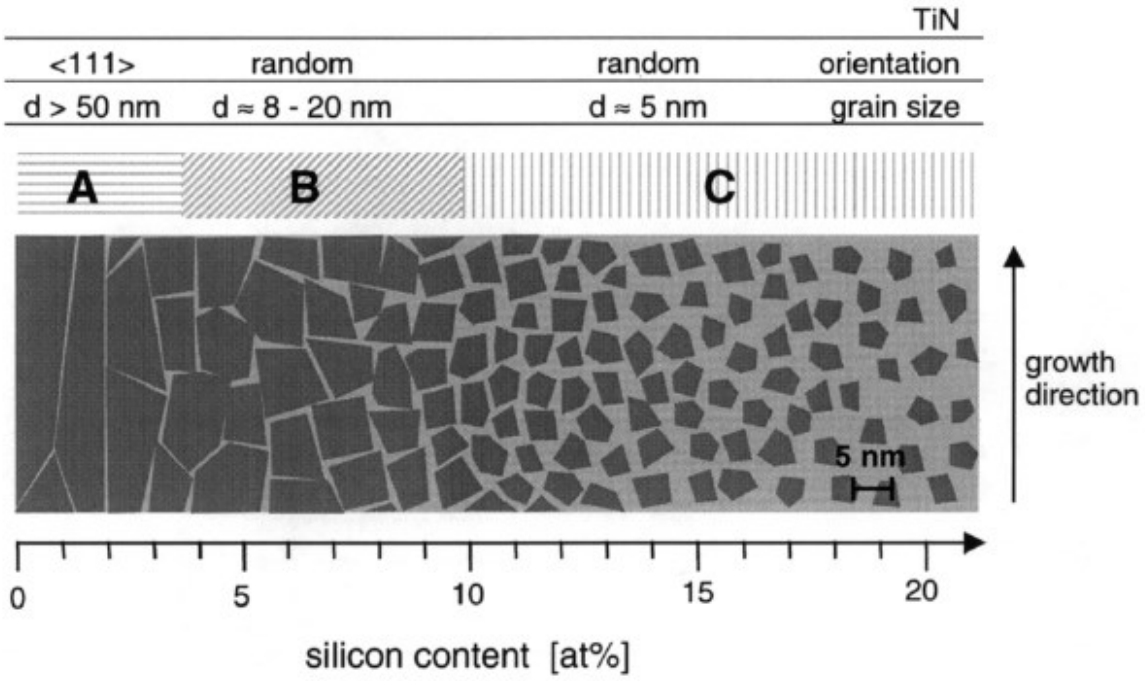

Figure 2.3: Morphological zone model for nc-$TiN/a\text{-}Si_3N_4$ as a function of the Si content, as proposed by Patscheider et al. [40]. The dark areas represent nanocrystals, the lighter zones stand for the amorphous phase.

The presence of the amorphous phase (SiN_x and BN_x) affects significantly the development of film structure and morphology (see Fig. 2.3). It hinders the individual grains in their growth and fosters the formation of a fine-grained and dense structure without pronounced columnar growth (see publication I and III). Full coverage of the crystallites by the amorphous phase promotes formation of an almost randomly oriented structure and further reduction of grain size (<10 nm). The improvement of mechanical properties by addition of Si or B is attributed to a combination of

hardening mechanisms (see publication I and III). Small amounts of the alloying element are incorporated into the fcc AlCrN lattice causing local stress fields, accompanied with an hardness increase induced by formation of a solid solution. The grain size refinement caused by the formation of an amorphous phase results in an additional hardness increase according to the Hall-Petch relationship [41]. Moreover, the amorphous phase effectively restricts generation and propagation of dislocations in the film under loading and thus, promotes further increase in hardness.

Si as an alloying element is also known to improve the thermal stability and oxidation resistance in nitride thin films [42]. Al-Cr-Si-N films with high Si content revealed the highest onset temperature for oxidation accompanied with the lowest weight gain (see publication II). The onset temperature of oxidation is increased from 1100 °C for Si-free Al-Cr-N to 1325 °C for Al-Cr-Si-N coatings. The oxidation rate in Al-Cr-Si-N thin films is determined by the slowly growing dense oxide scale composed of $(Al_xCr_{1-x})_2O_3$ and SiO_x. The incorporation of B into metastable Al-Cr-N reveals a significant improvement in wear resistance with respect to state of the art Al-Cr-N hard coatings [21] (see publication IV).

2.7 Structural design and architecture

Bulk materials like tool steel and cemented carbide are often used in cutting applications. The cutting performance as well as lifetime is significantly increased by depositing a hard coating on the tool (substrate) surface. However, the performance of coated tools is not only affected by the hardness of the coating, but also by its toughness and adhesion to the substrate material. Hence, beside the material selection, structural design and architecture are important aspects for the development of powerful coatings. The most encouraging possibilities to overcome the problem of early coating fatigue, caused by high local stress, is the formation of nanocrystalline and/or multilayer films [43]. The potential of the nanocrystalline films was already described in the sections before and revealed the improvement of mechanical and tribological properties with respect to conventional state of the art ternary nitride thin films.

Functional properties of nanocrystalline films can still be optimized by combining materials with different compositions in a multilayer structure. In general, multilayer

films can be classified in coatings with a low number of layers and coatings with an individual layer thickness in the size of lattice dimensions (superlattice coatings) [44-46]. The multilayers with a limited number of layers acquire their unique properties by interruption of the columnar growth and the combination of different materials. In contrast, superlattice coatings exhibit completely new material properties may be assessed with characteristics not directly related to the individual layers.

Here, the combination of Ti-Al-N and Al-Cr-B-N individual layers in multilayers with different architecture was investigated. Both constituents possess fcc crystal structure and similar lattice constants, and thus, the interfaces between the individual layers are assumed to be coherent. Moreover, Ti-Al-N films exhibit high hardness and good wear and oxidation resistance [15, 17, 18]. Al-Cr-B-N coatings, as mentioned before, reveal superhardness (~43 GPa, see publication III) and superior wear resistance (see publication IV). These preconditions give rise to a coating system with outstanding properties. The hardness of Ti-Al-N/Al-Cr-B-N multilayer films reaches a hardness of almost 50 GPa (see publication IV) This increase in hardness is attributed to a combination of several effects including layer thickness, volume of the interface, grain size, texture and dislocation density. Hence, the extraordinary hardness of Ti-Al-N/Al-Cr-B-N multilayer films can be ascribed to a combination of hindered dislocation motion at the interface, the increased number of interfaces and Hall-Petch hardening [46, 47]. Moreover, the superlattice arrangement results in a significant reduction of residual compressive stress with increasing number of interfaces, being sites of energy dissipation and stress relaxation [43].

The tribological performance of this multilayer arrangement is significantly enhanced in comparison with Ti-Al-N and Al-Cr-B-N single layer films (see publication IV). The improved wear resistance is a consequence of improved adhesion and toughening of the coating, mainly attributed to the increased number of coherent interfaces.

3 Coating synthesis

As already mentioned in section 2.4 the most commonly used PVD techniques are magnetron sputtering and cathodic arc evaporation. However, most industrially applied hard coatings are synthesized by the arc evaporation method, due to the higher deposition and ionization rate compared to magnetron sputtering. In this thesis, all coatings were produced by means of cathodic arc evaporation, and hence, some characteristics of this method followed by details concerning the film growth are described in this chapter.

3.1 Cathodic arc evaporation

PVD processes are basically accomplished in low pressure environment in order to minimize collisions of the vaporized coating material (from the target) during transport to the substrate, where it condenses and forms a solid film. A main advantage of PVD techniques is the possible film synthesis from pure metal (Ti, Cr, AlCr…) and/or compound targets (Al_2O_3, AlN, BN …), but also by applying a reactive gas to the working chamber. Beside a huge variety in coating materials, PVD allows the deposition of thin films on a diversity of substrate materials [13, 48]. However, the PVD process results in synthesis of coatings usually far from their thermodynamic equilibrium.

Cathodic arc evaporation uses a low voltage, high current arc discharge between two electrodes in a vacuum to vaporize the target surface (cathode) [49]. These arc discharges are characterized by low voltages in the range from 20-100 V and high currents between ~30 and a few hundred amperes [50]. The arc discharge process is only enabled by phase transition of the solid cathode material into the plasma state, which is by definition a quasi-neutral medium of positively and negatively charged particles [51]. The ignition of an arc is achieved by a mechanical trigger striking on the cathode surface generating a temporary short circuit. The point where the arc is in contact with the target is denoted as arc spot, which is limited to an area of a few micrometers. The arc spot is, thus, characteristic of a high current density of ~10^{12} A m^{-2}. Spot ignition and explosion is completed after 1 – 10 ns and the total life time is of the order of 100 ns [50]. A schematic drawing of a cathodic arc source and an arc spot is illustrated in Fig. 3.1. Spot ignition most probably occurs at asperities

(roughness tips) on the cathode surface resulting in significant amplification of the electric field. The electric field attracts ions, which bombard and heat the asperity. The high current density promotes further heating of the tip, which results in sublimation and explosion of the surrounding material. In addition, hypersonic jets of highly ionized plasma (up to 100%) are produced. The plasma typically contains multiply charged metal ions, depending on the used cathode material. The kinetic energy of the ions is typically in the range of 20 to 150 eV [50].

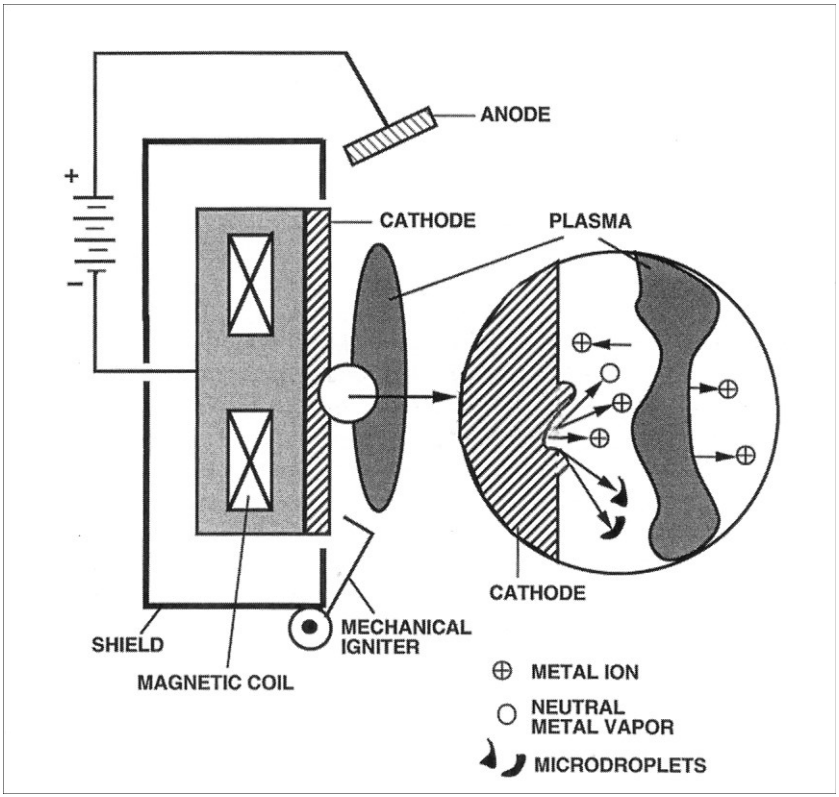

Figure 3.1: Scheme of a cathodic arc source and the arc spot [52].

As mentioned before, the residence time of an individual arc spot is short, and thus, it moves on the cathode surface preferentially alongside the asperities. Basically, the arc can be operated in two different modes, in particular as random or steered arc. The random arc is featured by good target utilization, however suffers from the possibility that the arc is trapped at a small area resulting in melting and hence damaging of the target. Moreover, this random movement requires the installation of a special target housing. Such a housing, often called as confinement ring (mostly of BN), hinders the arc from escaping the target and damaging the vicinity. This behavior can be avoided by using the steered arc technique [53]. Here, coils or

permanent magnets are placed behind the cathode and allow predetermination of the arc spot path. This system enables a specific adjustment with respect to the used cathode material. Hence, the magnetic fields support uniform target erosion, accelerate the plasma, reduce the droplet incorporation and increase the coating adhesion.

Droplet formation is the major drawback in the conventionally conducted arc evaporation process. As illustrated in Fig. 3.1, the generation of a highly ionized plasma is accompanied by ejection of droplets (macroparticles) at the margins of the arc spot. These droplets consist of target material, which is sufficiently heated to become molten but did not evaporate [50]. The size of the macroparticles varies from 0.01 to 10 µm and depends on the cathode material. In general, arc evaporation of cathode materials with higher melting point generate smaller and a lower amount of droplets. Incorporation of macroparticles in the growing film cause growth defects (Fig. 3.2), which increase the surface roughness and diminish the performance of the coating in application.

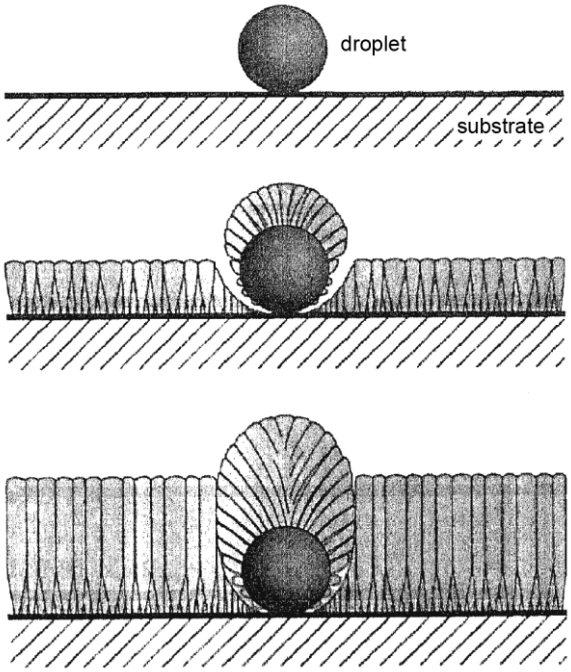

Figure 3.2: Formation of a growth defect by incorporation of a droplet in the film structure [54].

Such macroparticles in the film structure are sites of increased porosity [54] and, thus, can act as diffusion paths resulting in corrosion of the subjacent substrate. However, due to the high ionization level cutting performance of arc evaporated hard coatings with droplets is still comparable or better than films synthesized by magnetron sputtering. Nevertheless, great efforts have been taken to reduce or completely suppress droplet incorporation in the coating structure. A possibility to significantly reduce droplets is the usage of afore mentioned steered arc sources (providing magnetic fields), which increase the speed of arc spot motion and thus, diminish the ejection of macroparticles. A more drastic way to avoid droplets is the use of electromagnetic filters [50]. Here, strong magnetic fields are used to bend the plasma, and thus, the path of the ions is separated from that of the droplets.

In summary, cathodic arc evaporation is a progressive deposition technique, offering much higher deposition and ionization rates than commercially used magnetron sputtering. Coatings synthesized in this way reveal a dense film structure accompanied with enhanced adhesion to the substrate. These features are provided by the high degree of ionization and the high fraction of multiply charged ions.

3.2 Film growth

Similar to bulk materials, the microstructure of thin films substantially affects their mechanical and tribological properties, as well as thermal and oxidation behavior. However, the coating behavior is completely different from properties of their bulk counterpart, since coatings reveal much smaller grain sizes and metastable structures. Film microstructure can be varied over a wide range depending on the deposition method and used process parameters. The characterization of the microstructure comprises analysis of the grain size and crystallographic orientation, phase composition and coating morphology. A detailed description of film growth and fundamentals of structural evolution in thin films exists in several textbooks and publications [13, 52, 55-58]. In the following chapter, only a brief summary of mechanisms influencing film growth and structure will be presented.

Nucleation and modes of film growth

The evaporated atoms and ions (mainly ions in the case of cathodic arc evaporation)

from the target are accelerated towards the substrate and impinge on the surface with a specific arrival rate, where they are adsorbed or directly reflected (Fig. 3.3) [13]. The adsorbed particles can diffuse at the substrate surface, until they are either reevaporated or more commonly become trapped at low-energy lattice sites (i.e. starting points of nucleation).

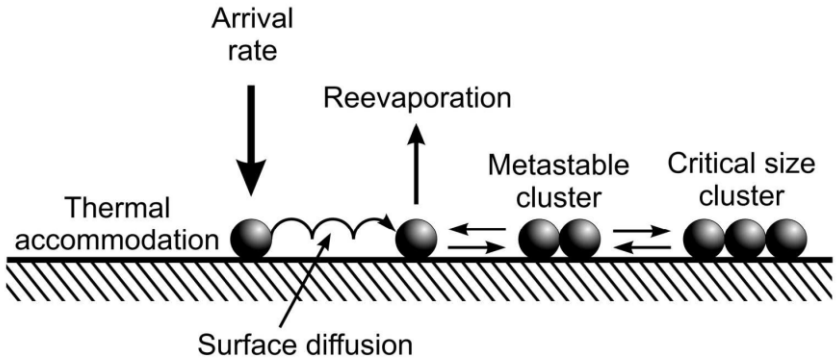

Figure 3.3: Schematic illustration of the nucleation process and film growth on a substrate [58].

Low impingement rates can result in equilibrium between adsorption and desorption, and thus, no nucleation or film formation takes place. In contrast, sufficiently high impingement rates cause formation of stable and metastable clusters, which can grow by binding of diffusing adatoms or by direct catching of atoms from the vapor phase. If the cluster reaches a critical size, adjacent nuclei combine and form a network of connected clusters. Hence, a film with full coverage is created.

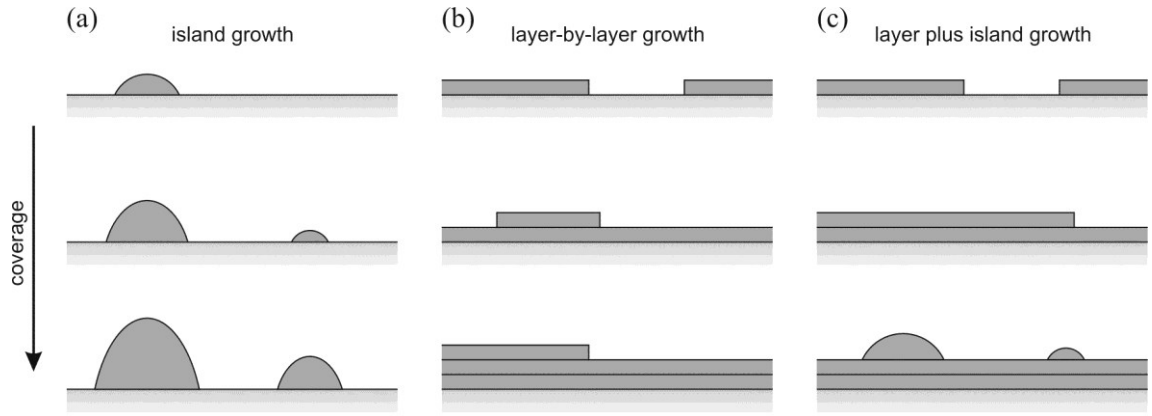

Figure 3.4: Different modes of film growth (a) island growth (Volmer-Weber), (b) layer by layer growth (Frank-van der Merwe, (c) layer + island growth (Stranski-Krastanov) [59].

In general, three modes of film growth can be distinguished, in particular island growth (Volmer-Weber), layer by layer growth (Frank-van der Merwe) and a combined layer-island growth (Stranski-Krastanov) (see Fig. 3.4). The mode which is preferred depends on the predominant energy distribution. If the adatoms are stronger bonded to each other than to the substrate, then small islands are formed on the substrate (Fig. 3.4a). These islands finally coalescence resulting in a fully covered substrate. In the case of layer by layer growth (Fig. 3.4b), the binding energy between the adatoms is equal to or smaller than that between film atoms and substrate. The third growth mode is a combination of both, layer and island growth. At the beginning layer growth is predominant, which changes after forming a few monolayers to the island growth (Fig. 3.4c) [13, 52].

Structure zone models

The different growth modes mentioned before are idealized cases and only valid when the surface diffusion of adatoms is sufficient to minimize the surface energy. Hence, nucleation is not kinetically limited and the equilibrium state can be reached. However, any process that causes a change in the arriving particle flux over the substrate surface affects the evolutionary growth process. Real film growth is influenced by processes like shadowing, the activation energy of surface and bulk diffusion and the bonding energy between surface and adatoms. Shadowing results from the geometric interaction between the surface roughness and the line-of-sight directions of the arriving deposition atoms, and causes voids in the growing film [60]. The shadowing effect can be compensated by surface diffusion, i.e. by increasing the energy of the adatoms. For many metals, the above-quoted energies are related and proportional to their melting point (T_m). Thus, several of the processes, including shadowing, are expected to dominate over different ranges of substrate temperature (T_s) expressed in terms of its homologous temperature (T_s/T_m). This T_s/T_m - ratio is the basis for any structure zone models (SZM). Movchan and Demchishin presented a SZM as a function of T_s/T_m, which allows a classification into three zones, each of them with its own characteristic structure [61]. This model was extended by Thornton [62], who introduced an additional axes to account for the sputtering gas Ar. Messier et al. modified Thornton's model by replacing the pressure axes by the substrate bias

voltage, which influences the energy of impinging ions during film growth [63]. The description and comparison of these individual SZM can be found in literature [13, 56, 60-63].

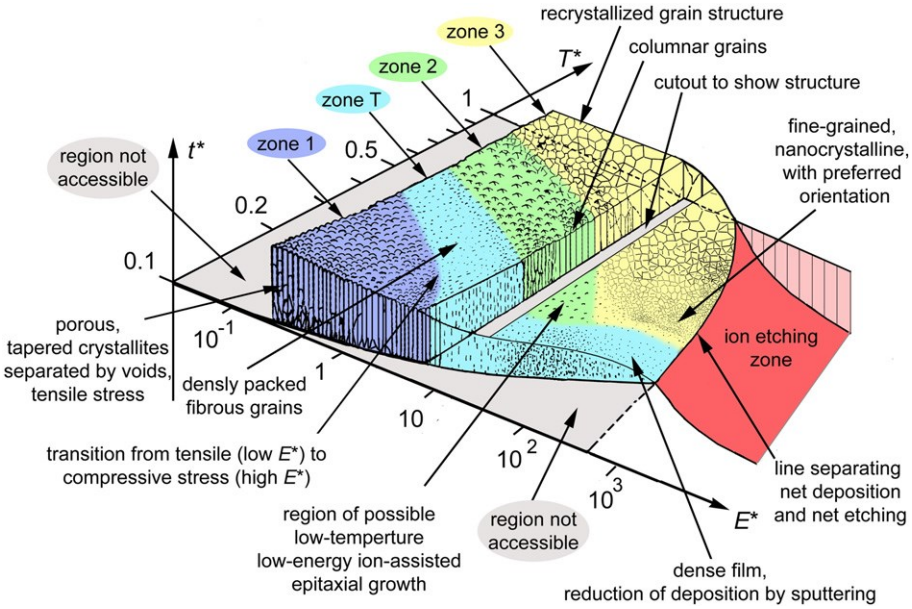

Figure 3.5: Structure zone diagram applicable to energetic deposition [64].

In the following, the recently proposed structure zone model by Anders will be presented briefly (see Fig. 3.5) [64]. In this SZM, the homologous temperature is replaced by a generalized temperature (T^*), which includes beside the T_s/T_m – ratio a temperature shift caused by the potential energy of particles arriving on the surface. The linear pressure (Thornton) or bias voltage (Messier et al.) axis is substituted by a logarithmic axis for a normalized energy (E^*), describing displacement and heating effects caused by the kinetic energy of impinging particles. The z-axis in this SZM is labeled with the net film thickness (t^*), which shows in addition to the qualitative illustration of film structure a thickness reduction by densification and sputtering. Moreover, the SZM allows to include a “negative thickness” due to the effect of ion etching.

The different zones with their structural characteristics are well accepted in the thin film community and illustrated in Fig. 3.5 [61-63]. In Zone 1, the structure is poorly defined and consists of porous, tapered crystallites separated by voids. The transition from Zone 1 to Zone 2 is characterized by a denser structure with poorly defined fibrous grains (Zone T), caused by the limited surface diffusion. Zone 2 consists of

columnar grains separated by dense, intercrystalline boundaries. The main feature of Zone 3 is a recrystallized equiaxed grain structure, since bulk diffusion has a dominant influence on the film structure.

Ion bombardment

Ion bombardment is a powerful tool for modifying the structure and properties of polycrystalline films [55]. In combination with the cathodic arc evaporation deposition technique, which provides a highly ionized plasma, the effect of the impinging energetic ions is even more pronounced. A negative bias voltage applied to the substrate causes an additional acceleration of the positive metal (target) ions towards the substrate surface and if their incoming energy is high enough, film growth is affected by the bombarding ions (see Fig. 3.6a) resulting in generation of lattice defects (see Fig. 3.6b). Incoming ions or knock-on atoms with high energy will knock atoms out of their lattice positions and create secondary collisions resulting in cascades of collisions. Moreover, the impinging particles can be physically implanted into the lattice and surface particles might be incorporated in subsurface sites by means of recoil implantation (Fig. 3.6a). Thus, increased ion bombardment induces collision cascades resulting in atomic displacements and hence, an increasing number of residual interstitials, vacancies and point defects (Fig. 3.6b) [22].

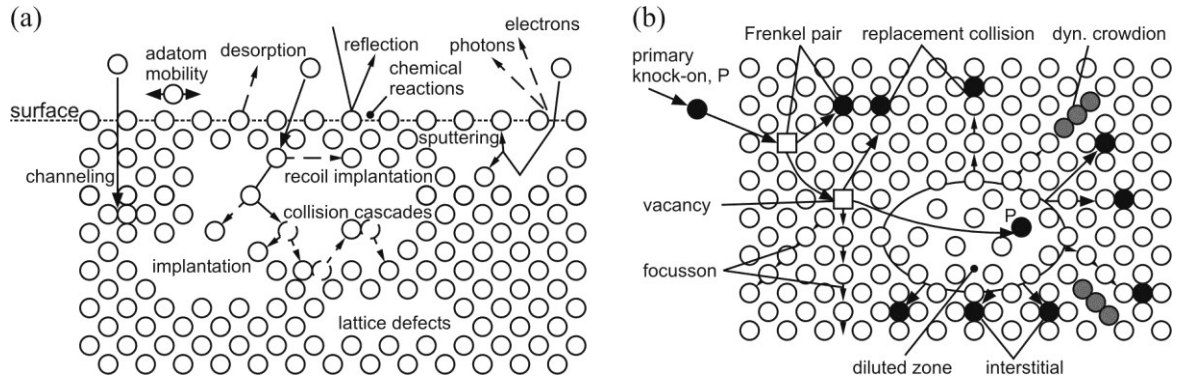

Figure 3.6: (a) Effects of ion bombardment on a growing film and (b) Schematic drawing of possible lattice defects [7].

In addition, ion irradiation in terms of substrate bias voltage increases the number of nucleation sites and supports densification of the film. As a consequence, energetic particles impinging on the film surface promote transition from Zone 1 to Zone T

according to the above mentioned SZM [62-64]. In case of cathodic arc evaporation, the high ion to neutral ratio allows control and modification of film structure and properties even at moderate ion bombardment. Increased ion energy affects also the structure of thin films, as it enables stabilization of metastable phases [65]. The enhanced ion impact causes a change in predominant texture and by means of an increased nucleation rate reduces the average grain size. Moreover, increasing ion bombardment promotes defect generation accompanied with higher residual compressive stress [66] and enhanced hardness. The significant effect of high energetic particles on film growth, structure and mechanical properties was also found for Al-Cr-Si-N and Al-Cr-B-N films, as shown in Publication I and III.

4 Coating characterization

The coatings investigated in this thesis were characterized in terms of their chemical composition and microstructure. Moreover, mechanical and tribological properties as well as the oxidation behavior of selected coatings were analyzed. The following chapter gives an overview of the used characterization techniques.

4.1 Determination of elemental and phase composition

- X-ray photoelectron spectroscopy (XPS)

X-ray photoelectron spectroscopy is a surface sensitive technique and is used to determine the chemical bonding as well as the chemical composition of a material. In the case of XPS, the sample is irradiated with X-rays (usually Al or Mg Kα) of known energy, which causes ejection of electrons from electron levels with binding energies less than the energy of the incident photon [60]. The measured kinetic energy (E_{kin}) of the ejected photoelectron is used to calculate the original electron binding energy (E_b) from

$$E_{kin} = h\nu - (E_b + \Phi), \quad (1)$$

since the photon energy ($h\nu$) and work function (Φ) are known. The binding energy is unique for a given element, and thus, the photoelectrons can be used for elemental identification. Moreover, the binding energy of a core electron is not only influenced by the specific element, but also depends on the adjacent atoms. Hence, peak shifts with respect to the binding energy are caused by different chemical environments. This so called chemical shift can be in the range of a few eV (energy resolution of XPS is ~0.1 - 0.5 eV) and enables determination of the binding state of the investigated element by comparing with reference catalogues [67, 68].

In Publication I, the presence of an amorphous SiN_x phase in Al-Cr-Si-N films was investigated by analysis of the relevant core level spectra. In the case of Al-Cr-B-N films, the influence of increasing B content on the binding state was investigated (see Publication III).

Since the information depth in XPS is below 10 nm, adsorbed surface contaminations interfere with the desired signals. Hence, sample preparation by means of in-situ

heating or sputter cleaning is recommended. Sputter cleaning results in complete removal of these adsorbates, however the significant energy transfer might alter the binding states. Thus, Al-Cr-Si-N and Al-Cr-B-N films were only heated to 350 °C prior to the XPS measurements.

- Raman spectroscopy

Raman spectroscopy is a contact-free analytical method and provides qualitative and quantitative information of materials. Raman scattering was first discovered by Krishna and Raman in 1928 and describes the inelastic scattering of monochromatic light with oscillating molecules [69]. A significant fraction of the incident photons are scattered elastically after collision with a molecule, which results in a unaltered energy state of both, photon and molecule (Rayleigh scattering). Inelastic scattering of the impinging photons results in a loss or gain of energy, depending onto whether the molecule is in an excited vibrational state or not, causing Stokes or anti-Stokes Raman scattering. Although peaks resulting from Stokes and anti-Stokes scattering are symmetrically positioned about the Rayleigh line, the intensities may differ. Furthermore, the anti-Stokes intensity depends strongly on temperature, whereas Stokes scattering is almost unaffected [70].

Raman spectroscopy is used to characterize materials and allows their identification by comparing the recorded spectrum with a database containing reference spectra. Raman spectra are commonly illustrated in terms of the difference between Rayleigh- and the Stokes-scattering, which is the so-called Raman shift given as wave number (cm^{-1}). This analysis technique is sensitive to defects, changes in stoichiometry and stresses in materials. These effects are evident from changes in peak intensity and peak position [69, 71, 72].

Within this work, Raman spectroscopy was used to investigate the oxidized Al-Cr-N and Al-Cr-Si-N coatings to identify the oxidation products (see Publication II). Al-Cr-B-N single layer films in their as-deposited state were also analyzed by means of the Raman scattering technique in order to reveal more details about the influence of increasing B content and ion bombardment, respectively (see Publication III). In Publication IV, Raman spectroscopy was performed to study the wear tracks of Al-Cr-B-N single layer and Ti-Al-N/Al-Cr-B-N multilayer films concerning the formation

of oxides after dry sliding tests at different temperatures.

- Elastic recoil detection analysis (ERDA)

Analysis of materials by means of elastic recoil detection analysis is done by irradiating the sample with a high energy ion beam (e.g. Cl^{7+}) with energies in the MeV range. As a consequence, scattered ions and recoiled atoms from the sample are generated. However, only the recoiled atoms are detected and identified. The particle identification can be applied either by energy loss measurement (Bragg ionization chamber) or by determining the velocity (time-of-flight method). More details concerning this method is found in Reference [73].

ERDA allows the determination of the elemental composition of a material and is able to quantify light elements (e.g. boron) with a high accuracy. Hence, ERDA was applied to identify the chemical composition of Al-Cr-B-N single layer films (Publication III). In addition, compositional depth measurements can be performed with this method. This feature was utilized to determine the elemental composition for different layers in Ti-Al-N/Al-Cr-B-N multilayer films (see Publication IV).

- Energy dispersive X-ray spectroscopy (EDX)

EDX allows determination of the elemental composition of materials. The main advantage with this technique is the fast qualitative identification of elements present in a sample. However, light elements like B or N are difficult to quantify with EDX [73]. For a short description see also in Section 4.2 (Scanning electron microscopy).

4.2 Methods for structural characterization

- X-ray diffraction (XRD)

X-ray diffraction is a powerful and non-destructive technique for determining the structure, texture and phase composition, and allows also the analysis of the stress state and an estimation of the grain size in polycrystalline thin films. XRD uses the correlation between lattice plane spacing and the wavelength of the appropriate X-ray. Irradiation of a polycrystalline sample with a monochromized X-ray beam of wavelength λ results in scattering of the X-rays in several directions. The intensity of the diffracted beam is recorded as a function of the diffraction angle θ and results in a diffractogram. However, emitted beams are only detected in the case of constructive interference of the scattered X-rays along certain directions (see Fig. 4.1). If this is fulfilled, the position of the individual peaks (i.e. the diffraction angles) can be calculated according to Bragg's law $\left(n \cdot \lambda = 2 \cdot d \cdot \sin\theta\right)$, where n is an integer and d describes the lattice plane spacing parameter. Hence, the crystallographic structure of crystalline materials can be described by Bragg's law, which is fulfilled only for special values of the diffraction angle [52, 71].

The XRD measurements carried out within this thesis were implemented in the Bragg-Brentano mode (as described above) and in the grazing incidence mode. In the latter mode the angle of incident X-rays was fixed to 2°, which minimizes the penetration depth into the material. Hence, in the case of a coated substrate the obtained diffraction peaks give exclusively information about the film structure.

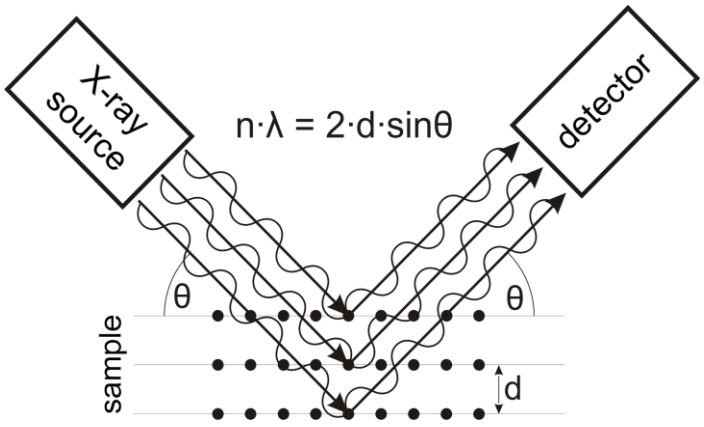

Figure 4.1: Schematic illustration of a constructive interference (Bragg condition) [74].

The position of the peak as well as the broadening gives useful information about the crystal. The broadening of the peak includes contributions from the grain size and the microstresses, whereas macrostresses in the coating cause a deviation of the peak position from the standard position. By fitting the diffraction pattern with a Pseudo-Voigt function, which is a linear combination of a Cauchy and Gaussian function, it is possible to separate the individual contributions to the peak broadening [75]. The Cauchy function describes the peak profile exclusively due to crystallite size, whereas a Gaussian function arises from strain. Consequently, an estimation of the grain size can be made. A detailed description for the determination of the crystallite size is given in Reference [75]. Al-Cr-Si-N and Al-Cr-B-N films, being investigated within this work, reveal augmented peak broadening with increasing Si and B content, respectively (see Publication I and III).

A more detailed description of X-ray diffraction and the individual measurement methods is found in References [76-78].

- Scanning electron microscopy (SEM)

Scanning electron microscopy is a standard technique in materials science and provides high magnification images, which gives information about the structure and morphology of materials. In SEM a focused electron beam is interacting with the material and causes generation of secondary electrons, back-scattered electrons and X-rays [13, 52]. The secondary electrons are used to topographically image the surface. Back-scattered electrons give an elemental contrast, since the amount of back-scattered electrons depends on the atomic number. The X-ray mode is used to determine the chemical composition of the materials. In this work, SEM was primarily used to study fracture cross-sections and the surface morphology of the synthesized films. Moreover energy dispersive X-ray spectroscopy was performed to get qualitative information on the elemental composition of the coatings.

- Transmission electron microscopy (TEM)

In contrast to SEM, transmission electron microscopy requires the preparation of thin films (~30 to 50 nm thickness) to allow transmission of electrons. Moreover, much higher acceleration voltages are required (a few hundred kV) in order to reach a high

resolution. The electrons interact with the material as they pass through and hence provide structural information of the material. The sample preparation for TEM investigation is rather time consuming and can be accomplished by focused ion beam milling and wedge polishing.

A TEM possesses a similar setup like light optical microscopes, however, electrons instead of visible light are used to irradiate the sample. Moreover, optical lenses are substituted by electromagnetic ones to magnify or condense the image. More details concerning the setup and configuration of transmission electron microscopes are given in Reference [79].

In general, a TEM can be operated in the diffraction and in the imaging mode. The diffraction mode uses a parallel electron beam to illuminate the specimen. To determine the orientation of individual crystallites, the diffraction volume must be limited to this area. This is achieved by an aperture, which results in a selected area electron diffraction (SAED) providing information similar to that given by XRD [79]. In the imaging mode, it can be further distinguished between bright field and dark field mode. If both, transmitted and scattered electrons reach the image plane; the resulting image is characterized by poor contrast (Fig. 4.2a). This problem can be overcome by insertion of an aperture in the back focal plane, which blocks all or parts of the diffracted electrons (Fig. 4.2b). In contrast, dark field images are obtained if one or more diffracted beams are displayed (Fig. 4.2c).

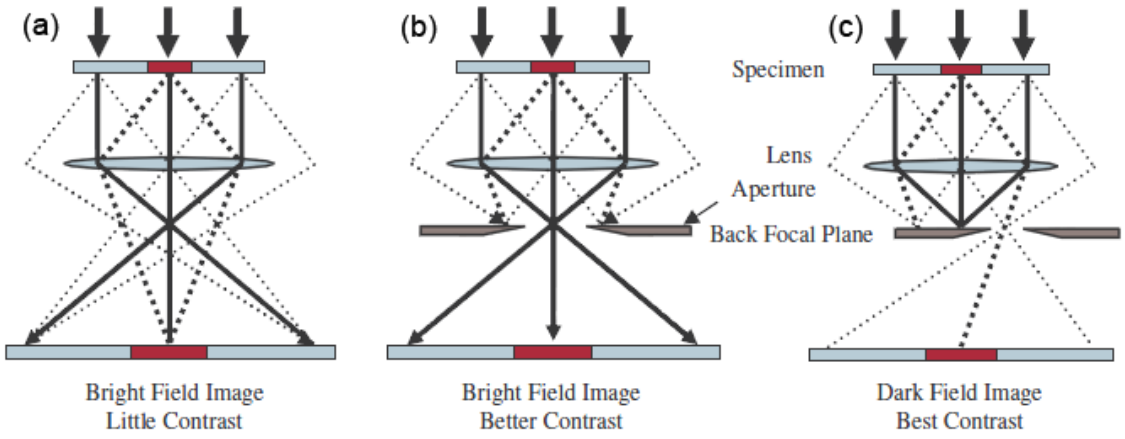

Figure 4.2: Examples of imaging modes. a) bright field with transmitted and diffracted electrons, b) bright field with only transmitted beam with better contrast, c) dark field image where only diffracted beams are displayed [80].

High-resolution (HR) imaging (Fig. 4.3) uses both, the unaltered transmitted and one or several diffracted beams. The resulting image arises from the constructive or destructive interference between both beams, which lead to phase contrast [81].

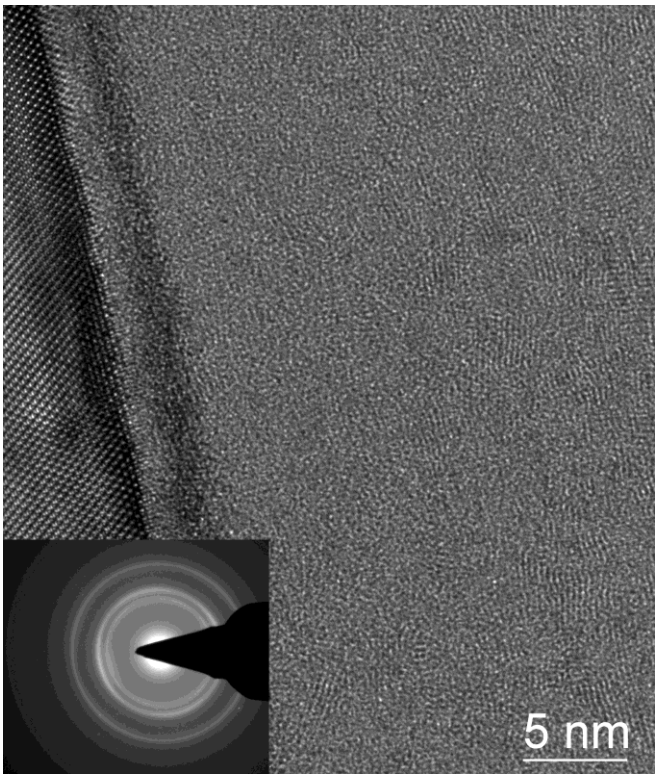

Figure 4.3: Cross-sectional high-resolution TEM micrograph of an Al-Cr-B-N film with 20 at.% B in the target grown at -40 V substrate bias, along with its respective SAED pattern (see also Publication III).

In Publication III, cross-sectional (HR)TEM imaging is used to investigate the microstructure of nanocomposite Al-Cr-B-N thin films. Moreover, the layer by layer growth of Ti-Al-N/Al-Cr-B-N multilayer films was accomplished by TEM (see Publication IV).

4.3 Methods for determination of mechanical properties

- Nanoindentation

Nanoindentation is used to gain information about hardness and Young's modulus of small samples, like e.g. thin films. Hardness is generally defined as the resistance of a material against plastic deformation induced by penetration of a harder material (e.g. a diamond tip). There are a variety of indenters with different tip shapes including spherical (Brinell), pyramidal (Vickers) and the most popular one is the three-sided Berkovich diamond indenter, due to its sharper tip [82, 83]. In contrast to micro- and macro-hardness, where the indentation depth is evaluated via optical microscopy from the projected area, nanoindentation is usually performed using instrumented indentation where the load and the indenter displacement are recorded during the measurement. A typical load-displacement curve with the loading and unloading responses is schematically illustrated in Fig. 4.4.

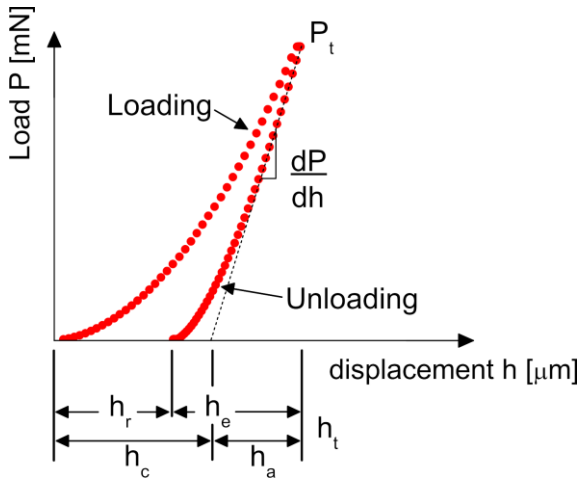

Figure 4.4: Schematic representation of a load-displacement curve [84].

The loading curve typically shows elastic-plastic behaviour, which is followed by an elastic unloading response. From the recorded load-displacement curves, hardness and Young's modulus of the films are evaluated according to the proposed Oliver and Pharr method [85]. A more detailed description on the evaluation and calculation of hardness and elastic modulus can be found in References [82] and [83].

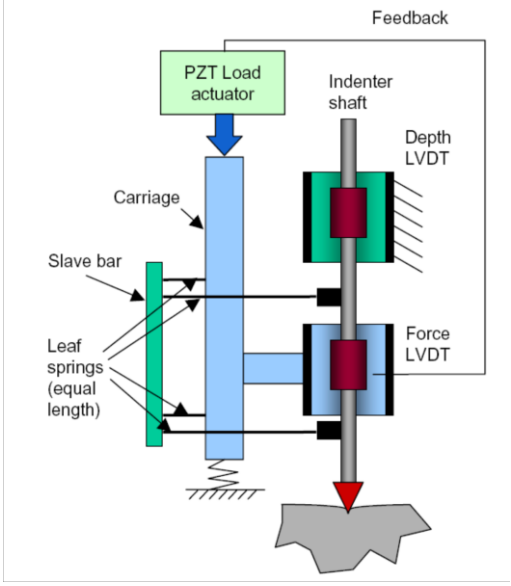

Figure 4.5: Setup of the UMIS nanoindenter (Fischer-Cripps Laboratories).

In this thesis, hardness measurements were accomplished using a Ultra Micro Indentation System (UMIS, Fischer-Cripps Laboratories) equipped with a Berkovich diamond tip. Figure 4.5 shows schematically the setup of the UMIS nanoindenter, where two separate LVDT sensors (linear variable differential transformer) are used to independently measure load and displacement.

The shape of the tip (sharp or already rounded) is critical and requires frequent calibration measurements on standards (fused silica) in order to generate accurate results. The hardness measurements in the Publications I, III and IV were done with a maximum applied load in the range between 5 and 25 mN to avoid the influence of the substrate.

- Stresses

The origin of stresses in thin films is attributed to various sources. These residual stresses within a coating on a substrate are generally composed of intrinsic, thermal and extrinsic stresses. The extrinsic stresses are a result of structural misfit, phase transformation, precipitation etc., and must be considered individually in every specific case. However, the investigated coatings within this work reveal no phase transformation in the temperature range used for stress measurements and therefore this term can be neglected. Intrinsic stresses are generated during nucleation and

film growth, and thus, depend on the used deposition process and conditions. Since the coating and substrate most likely possess different linear thermal expansion coefficients, the thermal stress component varies with temperature. At deposition temperature (500 °C, for all films synthesized within this work) the measured stress corresponds to the intrinsic stress component. However, when after deposition the coatings on substrates cool down to room temperature, the thermal stress is increased according to the individual thermal expansion coefficient of substrate and coating [86].

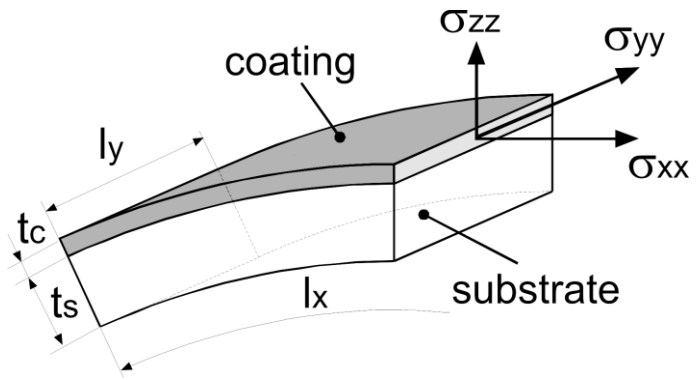

Figure 4.6: Schematic of a bended substrate-coating composite due to the residual stresses [7].

Stresses in thin films are commonly measured by means of the curvature and the X-ray method. Here, the stresses are determined from the curvature of coated substrates as illustrated in Fig. 4.6. If a coating is deposited onto only one side of a thin substrate, the biaxial stress within the coating causes the substrate to deform elastically in biaxial bending (normal stress σ_{zz} can be neglected). The radius of curvature of the coating-substrate composite is determined by means of two parallel laser beams and allows the calculation of the residual biaxial stress using the modified Stoney expression [87]. Moreover, with the curvature method it is possible to calculate the thermal expansion coefficient of the coating from the stress-temperature plot (see Publication III) [88]. More details regarding the used method can be found in Reference [7], whereas more information about stresses in thin films is enclosed in Reference [89].

- Tribological evaluation

There is a wide variety of tribotesting methods available to characterize friction and wear. The wear measurements within this work were obtained by the common ball on disc test. Figure 4.7 shows a schematic illustration of a CSM ball on disc tribosystem [90]. The principle behind this method is that a counterpart ball (Al_2O_3) is pressed with a defined normal load (5 – 10 N) on the rotating coated high-speed steel sample during the total sliding distance of 300 or 1000 m. As a consequence, wear is caused on the coating and on the counterpart itself. The alumina counterpart was chosen due to its high wear resistance and the chemical inertness even at high temperatures. During tribological testing, a Linear Voltage Displacement Transducer measures the friction force at the selected recording rate and calculates the coefficient of friction by dividing the friction force through the applied constant normal load. In this thesis, Al-Cr-B-N single layer and Ti-Al-N/Al-Cr-B-N multilayer films were tested up to 700 °C (see Publication IV).

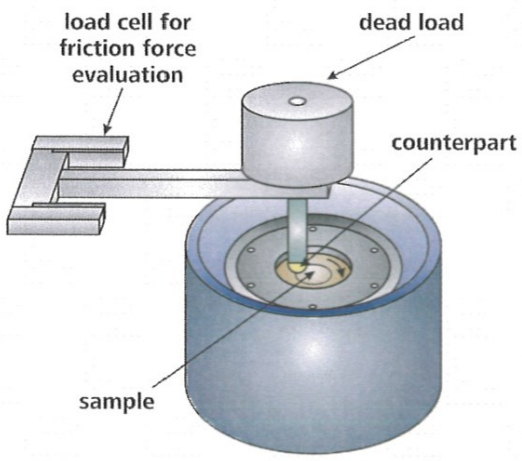

Figure 4.7: Schematic illustration of a CSM ball on disc tribosystem [90].

Subsequent to the ball on disc tests, the obtained wear tracks were analyzed with an optical profiling system using white light interferometry. This technique gives information about the wear depth and the volume of the displaced material. From the total volume of the removed material, the applied load and the sliding distance, the wear coefficient of the individual coatings can be calculated (see Publication IV) [6].

4.4 Analysis of oxidation behavior

- Simultaneous Thermal analysis (STA)

Thermal analysis (TA) offers the possibility to measure the change of a material property evoked by a temperature alteration. There are commonly a variety of methods used, where each of those analyze a specific material property. Simultaneous thermal analysis (STA) combines at least two of these methods, which analyze the same sample under identical conditions at the same time.

In this thesis, STA combining thermo-gravimetric analysis (TGA) and differential scanning calorimetry (DSC) was applied. In addition, the test facility was equipped with a mass spectrometer (MS). Figure 4.8 shows a picture of the used device (Netzsch STA 409C) with its individual components. A detailed description of this apparatus is given in Reference [32].

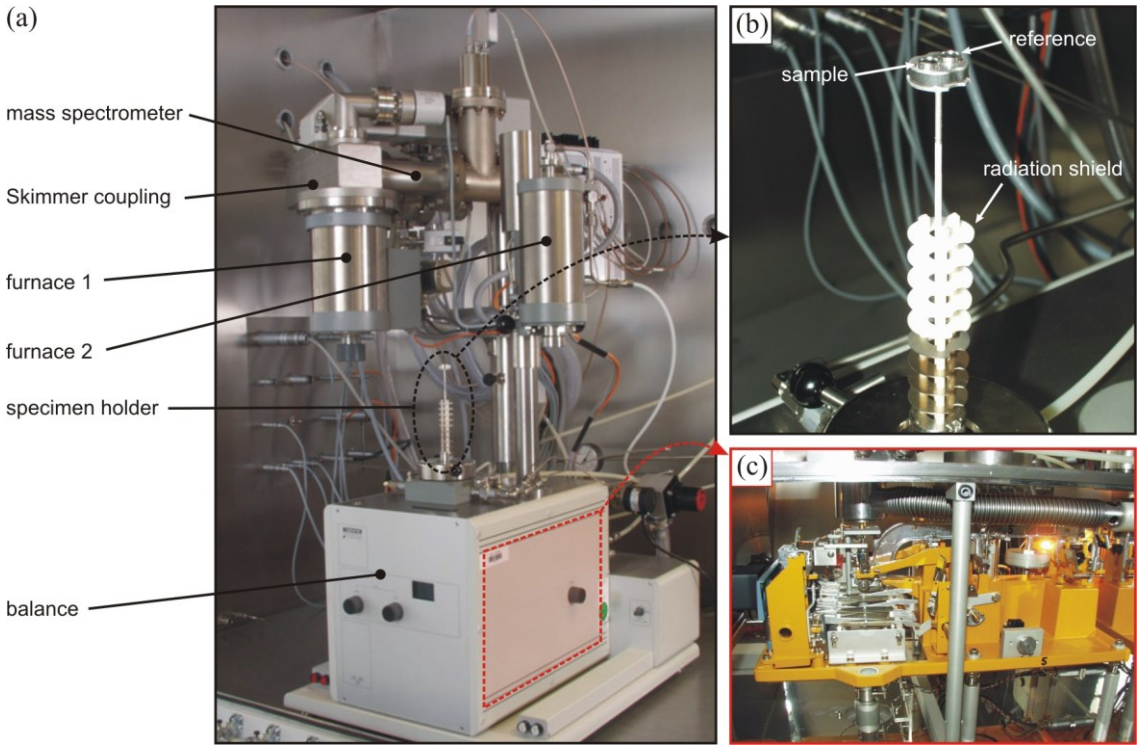

Figure 4.8: (a) Netzsch STA 409C combining DSC, TGA, and MS, (b) sample carrier with radiation shields, (c) mechanical balance for TGA measurements [32].

The TGA technique monitors the mass of a sample as a function of temperature or time, while the sample is exposed to a defined atmosphere. Hence, TGA allows characterization of materials that exhibit a mass loss (e.g. decomposition) or an increase in mass as in the case of formation of oxide scales. DSC is a method used to determine for example phase transformation temperatures or enthalpies of transformation by measuring the difference in heat flow to (endothermic) or from (exothermic) a sample with respect to a reference sample [91]. Mass spectroscopy is a powerful tool in combination with TGA and DSC, since this technique allows determination of gaseous products involved in the reactions.

In this work, simultaneous thermal analysis was performed to investigate the decomposition of Al-Cr-N and Al-Cr-Si-N thin films. In addition, the onset temperature of oxidation was determined for these coatings by means of dynamical measurements up to 1440 °C. Moreover, isothermal STA experiments in synthetic air were carried out to order to investigate the oxidation behavior of selected Al-Cr-N and Al-Cr-Si-N thin films (see Publication II).

5 Summary and conclusions

Al-Cr-N is a well-established coating applied on cutting tools and in the hot forging as well as the metal forming industry. CrN based coatings reveal good mechanical properties as well as good thermal stability and oxidation resistance. However, the ever increasing demand on films for high-temperature applications stimulates the development of metal nitride films with outstanding performance. In order to accomplish an improvement of Al-Cr-N coatings, different approaches were conducted within this thesis. The chemical composition was modified by forming quaternary Al-Cr-Si-N and Al-Cr-B-N systems with different contents of Si and B, respectively. These quaternary nitrides were analyzed with respect to their behaviour by varying the substrate bias voltage during deposition. Finally, multilayer coatings consisting of Ti-Al-N and Al-Cr-B-N individual layers and varying architecture were synthesized with the aim of combining their beneficial properties to further enhance the performance and durability of tools in service. All these coatings were synthesized by means of cathodic arc evaporation in an industrial scale deposition plant, which makes the results immediately available for application.

Al-Cr-Si-N and Al-Cr-B-N films are both based on the Al-Cr-N coating system. Addition of elements like Si and B results either in formation of a single-phase or a nanocomposite structure consisting of Al-Cr-(Si,B)-N grains embedded in an amorphous SiN_x or BN_x tissue phase, respectively, depending on the content of the alloying element. The main hardening mechanisms in these quaternary coatings are solid solution, Hall-Petch and nanocomposite hardening. Small amounts of Si or B are incorporated into the fcc AlCrN phase and cause local stress fields and thus increased hardness. Higher contents of alloying elements foster the formation of a nanocomposite structure, where the amorphous phase hinders growth of the Al-Cr-(Si,B)-N grains and causes an additional hardness increase according to the Hall-Petch effect.

Al-Cr-Si-N coatings exhibit enhanced oxidation resistance in comparison to Al-Cr-N films, as they form a slowly growing dense oxide scale composed of $(Al_xCr_{1-x})_2O_3$ and SiO_x. Tribological benefits can be observed by using B as alloying element in Al-Cr-N films. Al-Cr-B-N films reveal improved wear resistance, resulting in an order of magnitude lower wear coefficients compared to Al-Cr-N coatings without B addition.

Also Al-Ti-N/Al-Cr-B-N multilayer films show a significantly improved wear behaviour in comparison to Al-Cr-B-N and commercially applied Al-Cr-N and Al-Ti-N single layer films. Cuttings tests confirmed the outstanding performance of these multilayers, and consequently, a patent on this coating system has been registered for by the project partner Oerlikon Trading AG [92].

6 Bibliography

[1] W. Domke, Werkstoffkunde und Werkstoffprüfung, 10 ed., Cornelsen Verlag, Berlin, 2001.

[2] R. Ebner, H. Leitner, F. Jeglitsch, D. Caliskanoglu, in: F. Jeglitsch, R. Ebner, H. Leitner (Eds.), Proc. 5th Int. Conf. on Tooling, University of Leoben, Leoben (A), 1999.

[3] E. Badisch, Tribological Investigations of Tool Steels and Low-Friction Coatings, PhD Thesis, University of Leoben, 2003.

[4] H.-P. Stüwe, Einführung in die Werkstoffkunde, Bibliographisches Institut AG, Mannheim, 1991.

[5] B. Bhushan, Modern Tribology Handbook - Materials, Coatings and Industrial Applications, CRC Press, Boca Raton, 2001.

[6] K. Holmberg, A. Matthews, Coatings Tribology: Properties, Techniques and Applications in Surface Engineering, Elsevier, Amsterdam, 1994.

[7] P.H. Mayrhofer, Materials Science Aspects of Nanocrystalline PVD Hard Coatings, PhD Thesis, Montanuniversität Leoben, 2001.

[8] J. Musil, Surf. Coat. Technol. 125 (2000) 322.

[9] S. Vepřek, S. Reiprich, Thin Solid Films 268 (1995) 64.

[10] H. Gleiter, Acta Mater. 48 (2000) 1.

[11] H. Gleiter, Nanostruct. Mater. 6 (1995) 3.

[12] C.C. Koch, Nanostructured Materials-Processing, Properties, and Applications, second ed., William Andrew Publishing, Norwich, NY, USA, 2007.

[13] W. Gissler, H.A. Jehn, Advanced Techniques for Surface Engineering, Kluwer Academic Publishers, Dordrecht, 1992.

[14] O. Knotek, M. Böhmer, T. Leyendecker, J. Vac. Sci. Technol. A 4 (6) (1986) 2695.

[15] W.-D. Münz, J. Vac. Sci. Technol. A 4 (6) (1986) 2717.

[16] A. Hörling, L. Hultman, M. Odén, J. Sjölén, L. Karlsson, J. Vac. Sci. Technol. A 20 (5) (2002) 1815.

[17] D. McIntyre, J.E. Greene, G. Håkansson, J.-E. Sundgren, W.-D. Münz, J. Appl. Phys. 67 (3) (1990) 1542.

[18] K. Kutschej, P.H. Mayrhofer, M. Kathrein, P. Polcik, R. Tessadri, C. Mitterer, Surf. Coat. Technol. 200 (2005) 2358.

[19] A. Hörling, L. Hultman, M. Odén, J. Sjölén, L. Karlsson, Surf. Coat. Technol. 191 (2005) 384.

[20] A.E. Reiter, V.H. Derflinger, B. Hanselmann, T. Bachmann, B. Sartory, Surf. Coat. Technol. 200 (2005) 2114.

[21] R. Franz, B. Sartory, R. Kaindl, R. Tessadri, A. Reiter, V.H. Derflinger, P. Polcik, C. Mitterer, in: G. Kneringer, P. Rödhammer, H. Wildner, (Eds.), Proc. 16th Int. Plansee Seminar, Vol. 2, Plansee Holding AG, Reutte (A), 2005, 932 pp.

[22] P.H. Mayrhofer, C. Mitterer, L. Hultman, H. Clemens, Prog. Mater Sci. 51 (2006) 1032.

[23] M. Kawate, A.K. Hashimoto, T. Suzuki, Surf. Coat. Technol. 165 (2003) 163.

[24] S. Hofmann, H.A. Jehn, Werkst. Korros. 41 (1990) 756.

[25] O. Banakh, P.E. Schmid, R. Sanjinés, F. Lévy, Surf. Coat. Technol. 163-164 (2003) 57.

[26] M. Wittmer, J. Noser, H. Melchior, J. Appl. Phys. 52 (11) (1981) 6659.

[27] A. Sugishima, H. Kajioka, Y. Makino, Surf. Coat. Technol. 97 (1997) 590.

[28] Y. Makino, K. Nogi, Surf. Coat. Technol. 98 (1998) 1008.

[29] M. Kawate, A. Kimura, T. Suzuki, J. Vac. Sci. Technol. A 20 (2) (2002) 569.

[30] A. Kimura, M. Kawate, H. Hasegawa, T. Suzuki, Surf. Coat. Technol. 169-170 (2003) 367.

[31] J. Musil, H. Hrubý, Thin Solid Films 365 (2000) 104.

[32] H. Willmann, Al-Cr-N Thin Film Design For High Temperature Applications, PhD Thesis, Montanuniversität Leoben, 2007.

[33] Y. Ide, T. Nakamura, K. Kishitake, in: B. Mishra, C. Yamauchi (Eds.) Proceedings of the Second International Conference on Processing Materials for Properties, 2000, pp. 291.

[34] J. Vetter, E. Lugscheider, S.S. Guerreiro, Surf. Coat. Technol. 98 (1998) 1233.

[35] W. Kalss, A. Reiter, V. Derflinger, C. Gey, J.L. Endrino, Int. J. Refract. Met. Hard Mater 24 (2006) 399.

[36] P.H. Mayrhofer, H. Willmann, A.E. Reiter, 49th SVC Annual Technical Conference Proceedings (2006) 575.

[37] H. Willmann, P.H. Mayrhofer, P.O.Å. Persson, A.E. Reiter, L. Hultman, C. Mitterer, Scr. Mater. 54 (2006) 1847.

[38] J. Neidhardt, Z. Czigány, B. Sartory, R. Tessadri, M. O'Sullivan, C. Mitterer, Acta Mater. 54 (2006) 4193.

[39] S. Vepřek, Thin Solid Films 317 (1998) 449.

[40] J. Patscheider, T. Zehnder, M. Diserens, Surf. Coat. Technol. 146-147 (2001) 201.

[41] E. Arzt, Acta Mater. 46 (1998) 5611.

[42] M. Diserens, J. Patscheider, F. Lévy, Surf. Coat. Technol. 120-121 (1999) 158.

[43] H. Holleck, V. Schier, Surf. Coat. Technol. 76-77 (1995) 328.

[44] A.E. Santana, A. Karimi, V.H. Derflinger, A. Schütze, Surf. Coat. Technol. 177-178 (2004) 334.

[45] J. Lin, J.J. Moore, B. Mishra, M. Pinkas, W.D. Sproul, Surf. Coat. Technol. 204 (2009) 936.

[46] P.C. Yashar, W.D. Sproul, Vacuum 55 (1999) 179.

[47] J.S. Koehler, Phys. Rev. B 2 (2) (1970) 547.

[48] R.F. Bunshah, Handbook of Hard Coatings: Deposition Technologies, Properties and Applications, Noyes Publications, New Jersey, 2001.

[49] R.L. Boxman, P.J. Martin, D.M. Sanders, Handbook of Vacuum Arc Science and Technology: Fundamentals and Applications, Noyes Publications, New Jersey, 1995.

[50] U. Helmersson, M. Lattemann, J. Bohlmark, A.P. Ehiasarian, J.T. Gudmundsson, Thin Solid Films 513 (2006) 1.

[51] A. Anders, Cathodic Arcs - From Fractal Spots to Energetic Condensation, 1 ed., Springer, New York, 2008.

[52] M. Ohring, Materials Science of Thin Films - Deposition and Structure 2nd ed., Academic Press, San Diego, 2002.

[53] F.-W. Bach, T. Duda, Moderne Beschichtungsverfahren, Wiley-VCH, Weinheim, 2000.

[54] I. Petrov, P. Losbichler, D. Bergstrom, J.E. Greene, W.-D. Münz, T. Hurkmans, T. Trinh, Thin Solid Films 302 (1997) 179.

[55] I. Petrov, P.B. Barna, L. Hultman, J.E. Greene, J. Vac. Sci. Technol. A 21 (5) (2003) 117.

[56] P.B. Barna, M. Adamik, Thin Solid Films 317 (1998) 27.

[57] Y. Pauleau, P.B. Barna, Protective Coatings and Thin Films, Kluwer Academic Publisher, Dordrecht, 1997.

[58] J.E. Greene, Handbook of Crystal Growth, Elsevier Science Publisher, 1993, pp. 640.

[59] J.E. Greene, Handbook of Deposition Technologies for Films and Coatings, Noyes Publications, Park Ridge, 1994, pp. 681.

[60] R.F. Bunshah, Deposition Technologies for Films and Coatings - Developments and Applications, Noyes Publications, Park Ridge, 1982.

[61] B.A. Movchan, A. Demchishin, Phys. Metals Metallogr. 28 (1969) 653.

[62] J.A. Thornton, J. Vac. Sci. Technol. 11 (666) (1974).

[63] R. Messier, A.P. Giri, R.A. Roy, J. Vac. Sci. Technol. A 2 (1984) 500.

[64] A. Anders, Thin Solid Films 518 (2010) 4087.

[65] R. Franz, J. Neidhardt, B. Sartory, R. Tessadri, C. Mitterer, Thin Solid Films 516 (2008) 6151.

[66] H. Ljungcrantz, L. Hultman, J.-E. Sundgren, J. Appl. Phys. 78 (1995) 832.

[67] La Surface database, http://www.lasurface.com/database/elementxps.php.

[68] NIST database, http://srdata.nist.gov/xps/.

[69] E. Smith, G. Dent, Modern Raman Spectroscopy - A Practical Approach, Wiley & Sons Ltd, Chichester, 2005.

[70] W.H. Weber, R. Merlin, Raman Scattering in Materials Science, Springer-Verlag, Berlin, 2000.

[71] R.C. Brundle, C.A. Evans Jr., S. Wilson, Encyclopedia of Materials Characterization, Butterworth - Heinemann, Boston, 1992.

[72] J.C. Parker, R.W. Siegel, Appl. Phys. Lett. 57 (1990) 943.

[73] H. Bubert, H. Jenett, Surface and Thin Film Analysis, Wiley-VCH Verlag, Weinheim, 2002.

[74] http://materials.unileoben.ac.at/fileadmin/shares/unileoben/dmw/images/Regina/Phasenanalyse.pdf, (07/2013).

[75] T.H.D. Keijser, J.I. Langford, E.J. Mittemeijer, A.B.P. Vogels, J. Appl. Cryst. 15 (1982) 308.

[76] M. Birkholz, Elements of X-ray scattering, Wiley-VCH, Weinheim, 2006.

[77] B.D. Cullity, S.R. Stock, Elements of X-ray diffraction, Prentice Hall, New Jersey, 2001.

[78] L. Spieß, G. Teichert, R. Schwarzer, H. Behnken, C. Genzel, Moderne Röntgenbeugung, 2 ed., Vieweg + Teubner, Wiesbaden, 2009.

[79] B. Fultz, J. Howe, Transmission Electron Microscopy and Diffractometry of Materials, 2nd ed., Springer, Berlin, 2002.

[80] A. Flink, Growth and Characterization of Ti-Si-N Thin Films, PhD Thesis, Linköping University, 2008.

[81] D.B. Williams, C. Barry Carter, Transmission Electron Microscopy - A Textbook for Materials Science, Springer Science+Business Media, New York, 2009.

[82] A.C. Fischer-Cripps, Surf. Coat. Technol. 200 (2006) 4153.

[83] A.C. Fischer-Cripps, P. Karvánková, S. Vepřek, Surf. Coat. Technol. 200 (2006) 5645.

[84] http://materials.unileoben.ac.at/fileadmin/shares/unileoben/dmw/images/Regina/Mechanische_Schichteigenschaften.pdf, 07/2013.

[85] W.C. Oliver, G.M. Pharr, J. Mater. Res. 7 (1992) 1564.

[86] W.D. Nix, Metallurg. Trans. A 20 (1988) 2217.

[87] J.D. Wilcock, D.S. Campbell, Thin Solid Films 3 (1969) 3.

[88] R. Daniel, D. Holec, M. Bartosik, J. Keckes, C. Mitterer, Acta Mater. 59 (2011) 6631.

[89] L. Freund, S. Suresh, Thin Film Materials - Stress, Defect Formation and Surface Evolution, Cambridge University Press, 2003.

[90] J. Paulitsch, Structural Development and Interfacial Engineering of Hard Coatings by HIPIMS, PhD Thesis, Montanuniversität Leoben, 2010.

[91] G. Hühne, W. Hemminger, H.J. Flammersheim, Differential Scanning Calorimetry, Springer Verlag, Berlin, 1996.

[92] C. Tritremmel, M. Lechthaler, Cutting Tools with Al-Cr-B-N/Ti-Al-N Multilayer Coatings, Patent No. WO2011095292-A1, US 2013052477 A1, CA2788142-A1, KR2012113790-A, CN102725434-A, EP2531633-A1, MX2012009044-A1, SG 182749 A1 (2011).

7 Publications

7.1 List of included publications

I. Influence of Al and Si content on structure and mechanical properties of arc evaporated Al-Cr-Si-N thin films,
C. Tritremmel, R. Daniel, M. Lechthaler, P. Polcik, C. Mitterer
Thin Solid Films, 534 (2013) 403-409.

II. Oxidation behavior of arc evaporated Al-Cr-Si-N thin films,
C. Tritremmel, P.H. Mayrhofer, R. Daniel, M. Lechthaler, P. Polcik, C. Mitterer
J. Vac. Sci. Technol. A, 30 (6) (2012) 061501/6.

III. Microstructure and mechanical properties of nanocrystalline Al-Cr-B-N thin films,
C. Tritremmel, R. Daniel, M. Lechthaler, R. Rudigier, P. Polcik, C. Mitterer
Surf. Coat. Technol., 213 (2012) 1-7.

IV. Mechanical and tribological properties of Al-Ti-N/Al-Cr-B-N multilayer films synthesized by cathodic arc evaporation,
C. Tritremmel, R. Daniel, H. Rudigier, P. Polcik, C. Mitterer
submitted for publication.

7.2 My contribution to included publications

	Conception and planning[1]	Experiments	Analysis and interpretation	Manuscript preparation[1]
Publication I	100	85	70	100
Publication II	100	100	85	100
Publication III	100	75	80	100
Publication IV	100	70	75	100

[1] Supervision not included

8 Publication I

Publication I

Influence of Al and Si content on structure and mechanical properties of arc evaporated Al-Cr-Si-N thin films

C. Tritremmel, R. Daniel, M. Lechthaler, P. Polcik, C. Mitterer

Thin Solid Films 534 (2013) 403-409

Influence of Al and Si content on structure and mechanical properties of arc evaporated Al-Cr-Si-N thin films

C. Tritremmel [a], R. Daniel [a,b], M. Lechthaler [c], P. Polcik [d], C. Mitterer [a,b]

[a] Christian Doppler Laboratory for Advanced Hard Coatings at the Department of Physical Metallurgy and Materials Testing, Montanuniversität Leoben, Franz-Josef-Strasse 18, A-8700 Leoben, Austria

[b] Department of Physical Metallurgy and Materials Testing, Montanuniversität Leoben, Franz-Josef-Strasse 18, A-8700 Leoben, Austria

[c] OC Oerlikon Balzers AG, Iramali 18, LI-9496 Balzers, Principality of Liechtenstein

[d] PLANSEE Composite Materials GmbH, Siebenbürgerstrasse 23, D-86983 Lechbruck am See, Germany

Abstract

The effect of Al and Si on development of structure and mechanical properties was studied for arc evaporated Al-Cr-(Si)-N films synthesized from Al-Cr and Al-Cr-Si composite targets. All films show stoichiometric compositions, with a Si content corresponding to the target and a minor loss of Al. The hardness of Al-Cr-N films reaches a maximum for Al/Cr ratios close to the solubility limit of AlN in CrN. The addition of Si results in a further increase of hardness due to solid solution hardening and formation of a nanocomposite structure, which is accompanied by a reduced crystallinity and grain size. Al-Cr-Si-N films with high Si contents show a reduced hardness due to grain boundary sliding promoted by the higher amorphous phase fraction.

Keywords: Al-Cr-N; Microstructure; Nanocomposite; Mechanical properties

1 Introduction

The increasing demand on films for high-temperature applications like severe cutting processes has stimulated the development of advanced metal nitride (MeN) films with outstanding performance. CrN-based films show excellent mechanical properties as well as good oxidation resistance and thermal stability [1]. Their mechanical and tribological properties can, however, along with their thermal stability

and oxidation resistance, be significantly improved by addition of Al [2-4]. Ternary Al-Cr-N exists with both cubic or hexagonal structure, depending on the elemental composition. The metastable $Al_xCr_{1-x}N$ solid solution, having the face-centered cubic (fcc) structure of NaCl (B1) type, was found to be stable up to $x = 0.6 - 0.8$ [3, 5, 6]. Above this solubility limit, the hexagonal ZnS-type (wurtzite) crystal structure is formed, becoming dominant at higher Al content. The critical Al content depends on the deposition conditions under which the films are prepared. Hexagonal Al-Cr-N films show, unlike their fcc structured counterparts, excellent thermal stability but they suffer losses in mechanical properties and oxidation resistance at elevated temperatures above 900°C [4]. Silicon is another alloying element known to improve hardness and oxidation resistance of MeN films [7, 8]. Si inclines to segregate to grain boundaries forming an amorphous SiN_x phase embedding individual MeN grains and thus hindering their growth. This nanocomposite structure exhibits unique mechanical and thermal properties and thus is very promising for high-temperature applications [9-11]. Recent studies on arc evaporated Al-Cr-Si-N have already investigated the influence of Si on microstructure development, mechanical and tribological properties [11-13]. However, these coatings were prepared either by a combinatorial approach using two laterally rotating cathodes (Cr and Al-Si) [11, 13] or by composite Al-Cr-Si targets with low Si content (i.e. 3 - 4 at.%) [12, 14]. In contrast, Park et al. used a hybrid approach (arc ion plating and magnetron sputtering) for the deposition of Al-Cr-Si-N films [8]. Despite Al-Cr-Si-N films have been widely explored, a detailed study on deposition by cathodic arc evaporation from Al-Cr-Si composite targets covering a wide range of Si contents is still missing. Application of these Al-Cr-Si composite targets is expected to allow the deposition of coatings with a more uniform chemical composition, which is requested in industrial applications.

In a former study, structural and mechanical properties of $Al_{0.70}Cr_{0.30-x}Si_xN$ films with Si contents up to 5 at.% in the target have been reported [15]. Based on X-ray photoelectron spectroscopy measurements, no explicit affirmation of the formation of a separate SiN_x phase was found for these low Si contents. Al-Cr-Si-N films with the highest Si content of 5 at.% revealed a dual-phase structure consisting of fcc and wurtzite Al-Cr-(Si)-N phases which is accompanied by deteriorated mechanical properties. In the present study, Si-free Al-Cr-N and Al-Cr-Si-N films with varying Al/Cr atomic ratios (1 - 2.8) and Si content (5 - 20 at.%) in the target were

investigated to illuminate the effect of both, Al and Si, on structure formation and on mechanical properties. The main focus was on Al-Cr-Si-N films deposited from targets with Al/Cr ratios of 1 at different substrate bias voltages. Under optimized deposition conditions, the films exhibit exclusively the metastable fcc structure. The mechanical properties of these films were correlated with their structure, chemical bonding state, phase composition, grain size and residual stress.

2 Experimental details

The Al-Cr-N and Al-Cr-Si-N thin films were synthesized by cathodic arc evaporation (CAE) in an industrial scale deposition system INNOVA (OC Oerlikon Balzers). For film deposition, four out of six arc sources were equipped with powder-metallurgically prepared Al-Cr-(Si) targets (PLANSEE Composite Materials). The Al/Cr atomic ratio in the Si-free targets was varied from 1.0 to 2.3, whereas in Al-Cr-Si targets the Al/Cr ratio was kept constant at 1 with varying Si content of 5, 10 and 20 at.%. Additionally, a set of Al-Cr-Si-N films was deposited from targets with high Al and Si contents, i.e. an Al/Cr ratio of 2.8 and 5 at.% Si. The films were deposited on ultrasonically cleaned mirror-polished Si and low-alloyed steel (DIN 1.0330, AISI 1008) substrates mounted on the two-fold rotating substrate holder. Double-side polished Si(100) strips ($20 \times 7 \times 0.5$ mm^3) were used for X-ray structural analysis of the films as well as the measurements of their stress state by substrate curvature method. Additionally, cemented carbide cutting inserts (WC - 6% Co) were used for morphological investigations by scanning electron microscopy (SEM) and for hardness measurements. Prior to deposition, the chamber was evacuated to a base pressure of 5×10^{-4} Pa or below, then heated to 500 °C and subsequently filled with pure nitrogen to a pressure of 3.5 Pa. The substrate temperature was maintained at 500 °C during the whole deposition process. The arc current on each target was set to 140 A, resulting in a power density of approximately 17 Wcm^{-2}. The Al-Cr-(Si)-N films were grown on substrates biased to -40, -70, -100 or -150 V, respectively. All films were synthesized with a typical film thickness of 3 ± 0.3 µm at a deposition time of 60 minutes.

The elemental composition of the films was determined by means of energy dispersive X-ray spectroscopy (EDX) in a SEM Zeiss Evo 50 and by elastic recoil detection analysis (ERDA) using a 35 MeV Cl^{7+} ion beam and a Bragg ionization

detector. Structural analysis of the films was conducted by means of X-ray diffraction (XRD), using a D8 Advance diffractometer by Bruker AXS equipped with a parallel beam optics and Sol-X detector. The XRD patterns were recorded in the Bragg-Brentano configuration using Cu Kα radiation. From the broadening of the XRD patterns, the size of coherently diffracting domains ("grain size") was determined by a single-line method using the Pseudo-Voigt function [16]. Additionally, a detailed texture analysis was performed by calculating the texture coefficient according to the Harris formula [17, 18]. X-ray photoelectron spectroscopy (XPS) measurements were performed with an Omicron Multiprobe system with a monochromized Al Kα beam of 1486.6 eV with a resolution <0.5 eV to study the chemical bonding structure of the Al-Cr-Si-N films. Prior to the measurements, the samples were heated to 350 °C to remove volatile surface contaminates. The core level spectra Si2p, N1s, Al2s, Al2p and Cr2p were recorded in the corresponding energy range using a step size of 0.02 eV and a dwell time of 0.1 s. For reference, XPS measurements of high purity β-Si_3N_4 powder (Grade: TB, Yantai Tomley Hi-Tech Industrial & Trading Company). Film hardness was measured by means of nanoindentation using an ultra-micro indentation system (UMIS, Fischer-Cripps Laboratories) equipped with a Berkovich diamond tip. Film surface was polished before indentation using a colloidal silica suspension with a grain size of 0.04 µm (OP-S suspension). The actual shape of the tip was determined by calibration measurements on a fused silica specimen. The hardness was calculated from at least 30 load-displacement curves in the load range from 5 to 20 mN to avoid the effect of the underlying substrate and to get statistically reliable values [19]. These conditions result in a maximum indentation depth of 200 nm. The biaxial stress state in the films was calculated via the substrate curvature method using the modified Stoney equation [20].

3 Results

The elemental composition of the Al-Cr-N and Al-Cr-Si-N films deposited at a substrate bias of -40 V, as determined by EDX, are summarized in Table 1. For the precise determination of the Si content, ERDA measurements were additionally performed on Al-Cr-Si-N films with an Al/Cr target ratio of 1, confirming the EDX results. The oxygen contamination in the Al-Cr-Si-N films (measured by ERDA) is $\leq$0.4 at.%, irrespective of the Si content. For the notation of the individual films, the

target composition is used throughout this paper. All films investigated in this study were found to be stoichiometric with respect to the $\frac{N}{Al+Cr+Si}$ ratio within the accuracy of EDX. The Si content in the films is slightly lower than in the target (see Table 1).

Table 1: Elemental composition of the Al-Cr-(Si)-N films deposited at a substrate bias of -40 V, as determined by EDX.

Target		Film					
Elemental composition [at.%]	Al/Cr	Elemental composition				Al/Cr	Film composition
		N [at.%]	Al [at.%]	Cr [at.%]	Si [at.%]		
$Al_{0.50}Cr_{0.50}$	1.0	51	23	26	-	0.90	$Al_{0.46}Cr_{0.52}N_{1.02}$
$Al_{0.60}Cr_{0.40}$	1.5	50	28	22	-	1.30	$Al_{0.56}Cr_{0.44}N_{1.00}$
$Al_{0.70}Cr_{0.30}$	2.3	51	33	16	-	2.05	$Al_{0.66}Cr_{0.32}N_{1.02}$
$Al_{0.475}Cr_{0.475}Si_{0.05}$	1.0	49	22	27	2	0.80	$Al_{0.44}Cr_{0.54}Si_{0.04}N_{0.98}$
$Al_{0.45}Cr_{0.45}Si_{0.10}$	1.0	52	20	24	4	0.85	$Al_{0.40}Cr_{0.48}Si_{0.08}N_{1.04}$
$Al_{0.40}Cr_{0.40}Si_{0.20}$	1.0	51	19	22	8	0.90	$Al_{0.38}Cr_{0.44}Si_{0.16}N_{1.02}$
$Al_{0.70}Cr_{0.25}Si_{0.05}$	2.8	50	34	14	2	2.45	$Al_{0.68}Cr_{0.28}Si_{0.04}N_{1.00}$

This Si loss is due to the lower average ionization state of Si (+1.4) compared to Cr (+2.1) and Al (+1.7) [21]. The numbers in the brackets imply the mean ion charge-state of the corresponding element in the plasma. Furthermore, Al and Cr have a higher fraction of two- and threefold ionized particles, respectively [21]. This means that Al and Cr ions impinge on the biased sample surface with higher energy, which results in ongoing Al and Cr subplantation. On the other hand, the Si atoms are thus positioned rather close to the surface and will be preferentially re-sputtered by the impinging particles of higher ion charge-state [22]. Furthermore, the Al-Cr-N and Al-Cr-Si-N films are both characterized by Al contents which are typically lower than the target composition. This is primarily caused by the gas scattering of Al during the CAE process resulting in its preferred loss [15, 21, 23]. The EDX measurements also revealed that the substrate bias variation has only a minor effect on the Al/Cr ratio and the Si content of the deposited films.

SEM micrographs of fracture cross-sections and film surfaces are shown in Fig. 1 for the Al-Cr-Si-N films (Al/Cr = 1) with Si contents of 5, 10 and 20 at.% synthesized at a substrate bias of -40 V. All films are well adherent to cemented carbide as well as Si and steel substrates and exhibit a dense structure without any evidence of columnar growth. Films with low Si content (5 at.%) exhibit granular-like morphology (Fig. 1d), which changes to more or less featureless structure with increasing Si content (Figs. 1e and f). Arc evaporated films are characterized by droplets formed during the deposition process. Their size and density depend on the target composition and the deposition conditions. Both the density and size of the droplets in the Al-Cr-Si-N films is increased with higher Si content (see Figs. 1b and c).

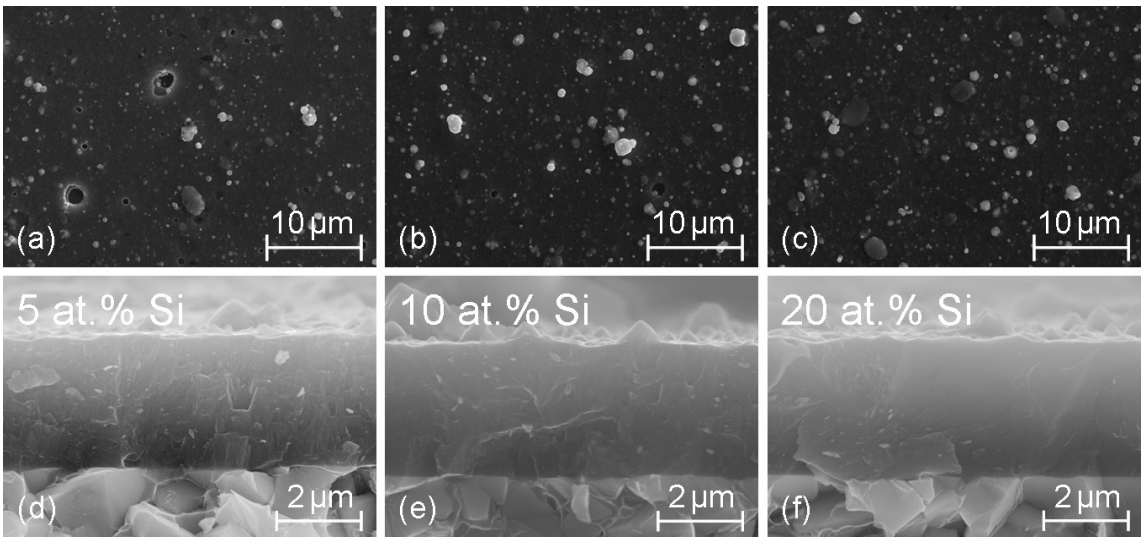

Figure 1: SEM plan-view and cross-sectional micrographs of $Al_{0.475}Cr_{0.475}Si_{0.05}N$ (a,d), $Al_{0.45}Cr_{0.45}Si_{0.10}N$ (b,e) and $Al_{0.40}Cr_{0.40}Si_{0.20}N$ (c,f) films, deposited on cemented carbide substrates at -40 V substrate bias.

XRD patterns of the Al-Cr-N and Al-Cr-Si-N films are shown in Fig. 2. All films, with the exception of that deposited from the target having the Al/Cr ratio of 2.8, exhibit exclusively the fcc phase irrespective of the Si content and the applied substrate bias, with diffraction peaks situated between fcc-AlN and fcc-CrN [24]. This reflects the formation of a metastable solid solution, where Cr is replaced by Al in the CrN lattice. The Si addition does apparently not affect the formation of this solid solution; however, it gives rise to changes of the film texture. While the Si-free

Al-Cr-N and the Al-Cr-Si-N films with a Si content lower than 5 at.% grow predominantly with (111) preferred orientation, the Al-Cr-Si-N films with higher Si content exhibit a structure consisting of (111)- and (100)-oriented grains. Additionally, only a minor contribution of (110)-oriented grains was found in all films; grains having the (311) orientation appear only in Si-free Al-Cr-N films and in Al-Cr-Si-N films with Si contents in the target lower than 20 at.%. Moreover, the Si addition into the Al-Cr-N films was found to result in a decrease of the intensity of the diffraction peaks and also in their broadening and shift towards higher 2θ angles. While the peak shift corresponds to changes of the crystal lattice due to residual stress (under the assumption that the composition does not change), the increase of the peak width with raising Si content reflects the reduction of the grain size. The diffraction pattern of the $Al_{0.70}Cr_{0.25}Si_{0.05}N$ film (Al/Cr ratio of 2.8 in the target) reveals a dual-phase polycrystalline structure with reduced crystallinity composed of wurtzite and fcc phases (Fig. 2). The wurtzite structure of this film deposited at -40 V substrate bias can be identified by the peak positioned close to hcp AlN (002) at 36.9° [24]. The most intense peak at $2\theta = 37.8°$ is a superposition of hcp-(101) and fcc-(111) reflections. Unlike all other single-phase films, $Al_{0.70}Cr_{0.25}Si_{0.05}N$ exhibits only a minor contribution of the fcc (100)-oriented grains.

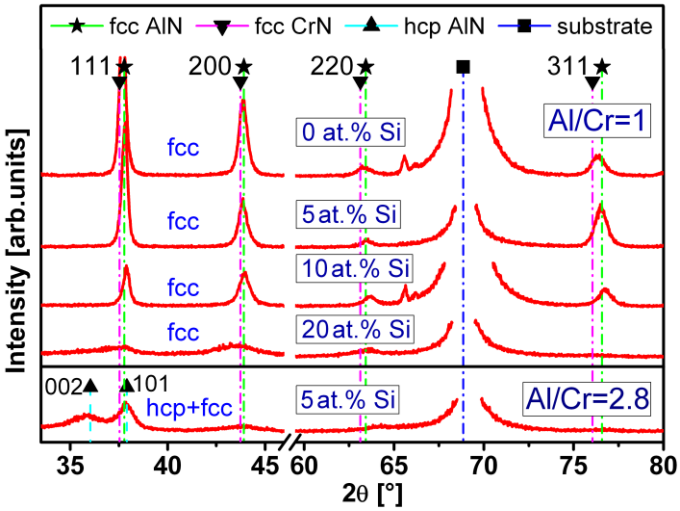

Figure 2: XRD patterns of Al-Cr-N and Al-Cr-Si-N films deposited on Si substrates at -40 V substrate bias. The XRD patterns of $Al_{0.60}Cr_{0.40}N$ and $Al_{0.70}Cr_{0.30}N$ films reveal similar peak positions.

A detailed analysis of the peak broadening allows the determination of the film grain size. Its variation as a function of the film composition is depicted in Fig. 3. For the calculation of the grain size, both (111) and (200) peaks were used in order to get reasonable results, since only grains parallel to the substrate surface can be considered. In the case of the dual-phase $Al_{0.70}Cr_{0.25}Si_{0.05}N$ film, only the fcc (111) peak was used for the analysis. The grain size changes only slightly with increasing Al/Cr ratio in the Al-Cr-N films (Fig. 3). The Al-Cr-N film with an Al/Cr target ratio of 1 is composed of grains having approximately 34 nm and the grain size slightly increases to 38 nm for an Al/Cr ratio increasing to 2.3. On the other hand, Si addition to Al-Cr-N films influences the grain size to a much higher extent (Fig. 3). As the Si content in the target increases from 5 to 20 at.% (corresponding to a change from 2 to 8 at.% in the films), the grain size decreases from 23 to approximately 6 nm. In the dual-phase $Al_{0.70}Cr_{0.25}Si_{0.05}N$ film (Al/Cr in the target of 2.8), the Si-induced grain refinement effect is even stronger. If the hexagonal Al-rich structure develops, already 2 at.% Si in the film result in the formation of grains with a size of only 7 nm (Fig. 3).

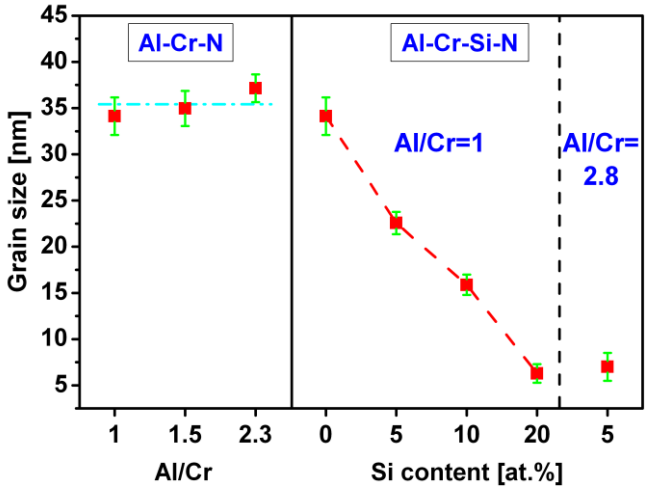

Figure 3: Development of the grain size of (a) Al-Cr-N films with different Al/Cr ratio and (b) Al-Cr-Si-N films with 5, 10 and 20 at.% Si in the target. All Al-Cr-(Si)-N films were deposited at a substrate bias of -40 V.

XPS measurements of the Al-Cr-Si-N films synthesized at -40 V substrate bias were performed to obtain additional information about the chemical bonding state. All relevant core level spectra, in particular N1s, Cr2p, Al2p and Si2p, were analyzed in terms of binding energies of the contributing bonding configurations. The main

constituents were identified as Cr-N and Al-N bonds [25]. The Si2p core level spectra of $Al_{0.475}Cr_{0.475}Si_{0.05}N$ and $Al_{0.40}Cr_{0.40}Si_{0.20}N$ films deposited at -40 V substrate bias are shown in Fig. 4, together with that of pure β-Si_3N_4 powder. Since XPS is a surface-sensitive analytical method and the samples were not sputter cleaned prior to analysis, all spectra exhibit oxidation-related contaminations (see the fitted Si-O subpeak in the energy range of 102.5 - 103.5 eV in Figs. 4a-c) [26]. The main component in the Si2p core level spectra of the Al-Cr-Si-N films is assigned to Si-N bonds (101-102 eV) [26] and corresponds well to the spectrum of the Si_3N_4 powder (Fig. 4c). Moreover, the shape of the Si2p regions of the spectra of the $Al_{0.40}Cr_{0.40}Si_{0.20}N$ film (Fig. 4b) and the Si_3N_4 powder (Fig. 4c) are rather similar and show the same subpeak contributions. The deviation in the position of the spectra is attributed to the non-constant electrical charge of the Si_3N_4 powder during measurement. The Si2p spectrum of the $Al_{0.475}Cr_{0.475}Si_{0.05}N$ film in Fig. 4a reveals additional minor contributions at lower binding energies (97.5 and 99.5 eV), which cannot be attributed to Si-N bonds but very likely correspond to Me-Si bonds (Me = Al, Cr). XPS analysis also revealed that an increasing Si content in the Al-Cr-Si-N films is associated with an increase of the volume fraction of Si-N bonds.

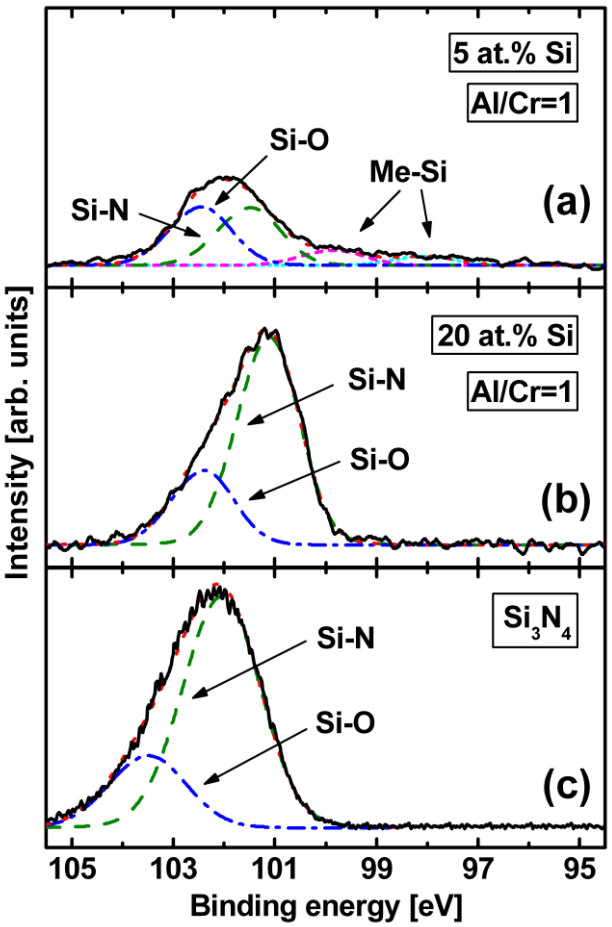

Figure 4: Si2p XPS core level spectra of (a) $Al_{0.475}Cr_{0.475}Si_{0.05}N$ and (b) $Al_{0.40}Cr_{0.40}Si_{0.20}N$ films and (c) β-Si_3N_4 powder. The Al-Cr-Si-N films were deposited at a substrate bias of -40 V on Si (100) substrate. The evidence of Al-Si and Cr-Si bonds in the high Si-containing film in the Si2p spectrum is suppressed by the Si-N peak of much higher intensity.

Enhanced ion irradiation of biased substrates is known to significantly affect film growth [27]. The effect of substrate bias ranging from -40 to -100 V on structural development of Al-Cr-Si-N films grown with 10 and 20 at.% Si in the target is shown in Fig. 5. In both cases, no preferred orientation is developed. Instead, a structure with (111)-, (100)-, (110)- and (311)-oriented grains is formed (see Fig. 5a). Moreover, the increasing energy of incident ions results in a decrease of the peak intensity, which reflects the reduction of crystallinity of these films. In the case of $Al_{0.45}Cr_{0.45}Si_{0.10}N$ films, the grain size continuously decreases from 16 nm at -40 V to 8 nm at -100 V. The enhanced formation of (100)-oriented grains indicates that under

these deposition conditions the adatom net flux is pronounced from (111)- and (311)-oriented planes towards the (100)-oriented surfaces [27]. Since the crystal lattice is effectively distorted by impinging ions with high energies [28], compressive stress develops in the films, which is reflected by a shift of the diffraction peaks towards lower 2θ angle.

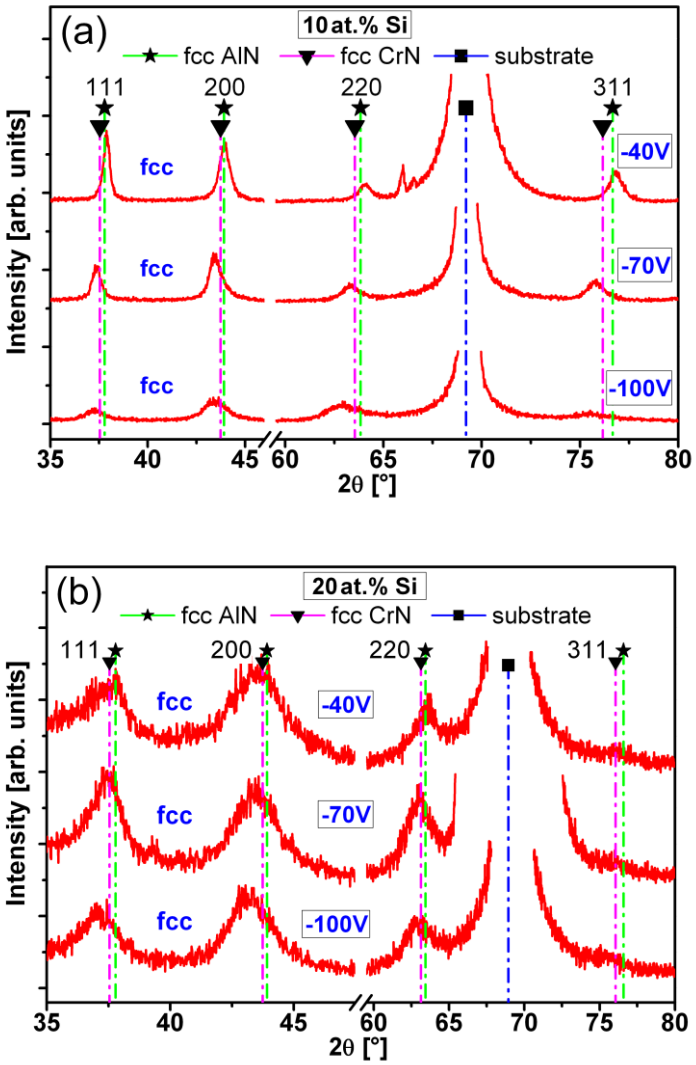

Figure 5: XRD patterns of (a) $Al_{0.45}Cr_{0.45}Si_{0.10}N$ and (b) $Al_{0.40}Cr_{0.40}Si_{0.20}N$ films deposited on Si substrates at substrate bias voltages varying between -40 and -100 V. The peak at 2θ ~ 69° is attributed to the Si substrate. Note, the scale of the intensity in Fig. 5b is by a factor of 5 lower than in Fig. 5a.

The development of texture of the Al-Cr-(Si)-N films as a function of the Si content is depicted in Fig. 6. The calculated texture coefficient reveals that while the

Si-free Al-Cr-N film exhibits a predominantly (111)-oriented structure. Growth of Al-Cr-Si-N films is significantly affected by the presence of Si, which is either incorporated in the AlCrN lattice or forms a SiN_x phase at the grain boundary [29], as evidenced by XPS measurements. As already mentioned, this results in the development of a film structure composed of grains randomly oriented in (111), (100), (110) and (311) directions. This effect is pronounced predominantly for the high Si content of 20 at.% in the target. In fact, with increasing Si content in the Al-Cr-N films, the fraction of grains oriented in (311) and (110) directions continuously increases at the expense of the (111) one, so that the film grown using the highest Si target content of 20 at.% exhibits a completely randomly oriented structure (evidenced by the comparable texture coefficient for all orientations). The grains having the fcc structure in the dual-phase $Al_{0.70}Cr_{0.25}Si_{0.05}N$ film show a pronounced (111) orientation, while the grains of the wurtzite phase are (001)-oriented (see Fig. 6).

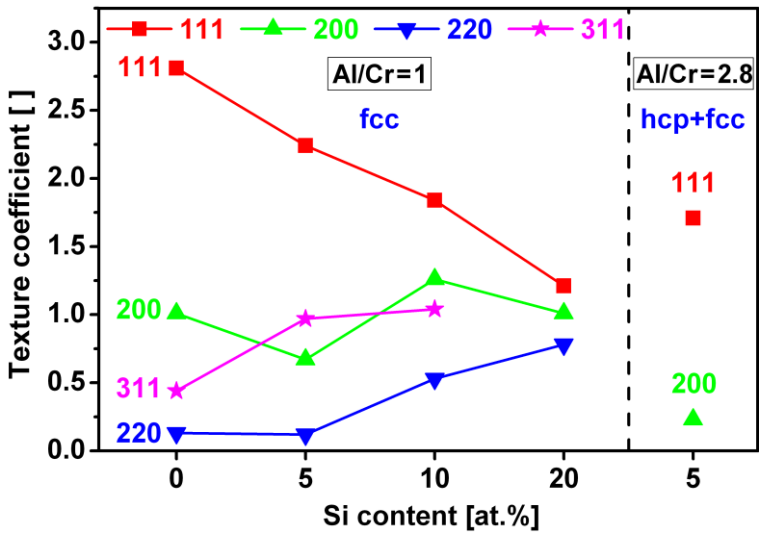

Figure 6: Coefficient of texture of an $Al_{0.50}Cr_{0.50}N$ film and Al-Cr-Si-N films with 5 to 20 at.% Si in the target and Al/Cr target ratio of 1 and 2.8. All films investigated were prepared at a substrate bias voltage of -40 V. For the dual-phase $Al_{0.70}Cr_{0.25}Si_{0.05}N$ film (rightmost) only grains having fcc structure are concerned.

The residual stress of the Al-Cr-N and the Al-Cr-Si-N films as a function of the Al/Cr target ratio, Si target content and substrate bias voltage is plotted in Fig. 7. All

films investigated are in the compressive stress state with stresses ranging from -0.3 to -1.9 GPa. This is predominantly a result of the high-energy, low-flux ion irradiation of the growing film, which causes formation of defects [28, 30, 31]. The Si-free Al-Cr-N film with Al/Cr = 1 in the target exhibits compressive stress of -1 GPa, which increases to -1.2 GPa for increasing the Al/Cr ratio to 2.3. The effect of Si addition to Al-Cr-N films on stress evolution, while keeping Al/Cr in the target constant at 1 and the substrate bias voltage at -40 V, is shown in Fig. 7. As the Si target content increases from 0 to 20 at.%, the compressive stress decreases from -1 to -0.3 GPa. The compressive stress in fcc Al-Cr-Si-N films with 5 and 10 at.% Si in the target rises with substrate bias increasing from -40 to -100 V from -1 to -1.5 GPa and from -0.9 to -1.7 GPa, respectively, which reflects the pronounced effect of ion bombardment. The lowest stress of -0.3 GPa is observed in the $Al_{0.40}Cr_{0.40}Si_{0.20}N$ film deposited at -40 V, showing the positive effect of Si addition on the reduction of compressive stress. However, also in this case, the increase of the substrate bias to -100 V results in an increase of compressive stress to -1.6 GPa. This effect is only moderate in the dual-phase $Al_{0.70}Cr_{0.25}Si_{0.05}N$ film, where the compressive stress varies only between -0.8 and -1 GPa, due to the presence of separated fcc and wurtzite phase fractions [15]. The stress increase at -150 V to -1.3 GPa is accompanied by the development of a higher fraction of ion-irradiation stabilized fcc phase [32].

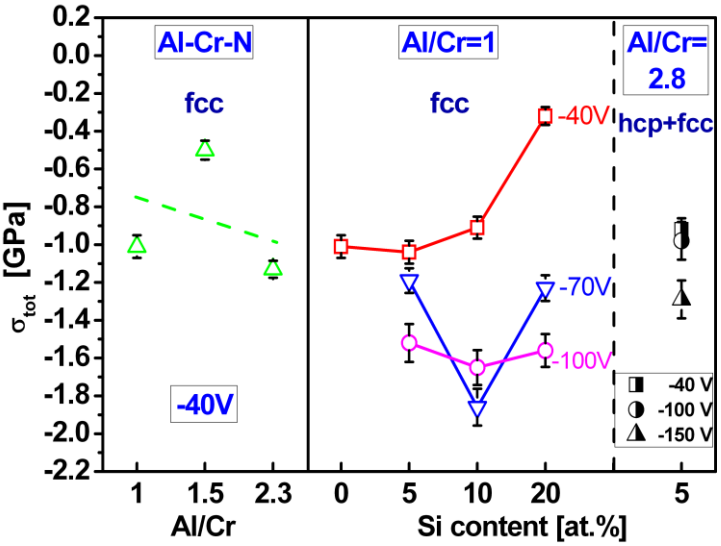

Figure 7: Residual stress of Si-free Al-Cr-N films with different Al/Cr target ratio deposited at -40 V substrate bias and Al-Cr-Si-N films with 5, 10 and 20 at.% Si in the target deposited at substrate bias voltage between -40 and -150 V.

The development of the hardness of the Si-free Al-Cr-N films deposited with various Al/Cr target ratios at -40 V substrate bias and the Al-Cr-Si-N films synthesized with increasing Si content at different bias voltages is shown in Fig. 8. The hardness of the Si-free Al-Cr-N films depends significantly on the Al/Cr target ratio. The maximum hardness of ~30 GPa is achieved for the highest Al target content of 70 at.%. Si addition to Al-Cr-N films (Al/Cr target ratio of 1 and substrate bias of -40 V) yields a hardness maximum of 36 GPa for a Si content of 10 at.%. A further Si increase above 10 at.% in the target is followed by a hardness decrease to ~30 GPa. The hardness of the films is beside the Si addition also enhanced by the ion irradiation. It increases with increasing substrate bias from 30 GPa at -40 V to 39 GPa at -100 V. By addition of 5 at.% Si to the high Al-containing Al-Cr-N film with composition $Al_{0.70}Cr_{0.25}Si_{0.05}N$, a hardness decrease to 28 GPa at -40 V substrate bias was observed. This hardness decrease is caused by the formation of the dual-phase structure composed of fcc and wurtzite phases. However, also in this case, an increasing substrate bias results in rising hardness, where the film deposited at -150 V exhibits a hardness of ~33 GPa.

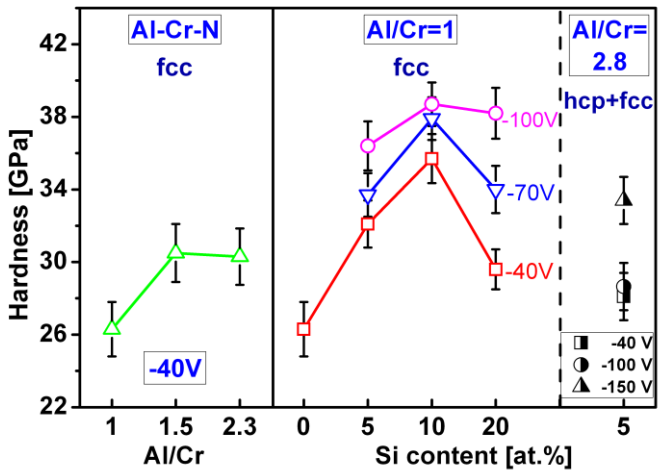

Figure 8: Hardness of Si-free Al-Cr-N films with different Al/Cr target ratios deposited at -40 V substrate bias and Al-Cr-Si-N films with 5, 10 and 20 at.% Si in the target deposited at substrate bias voltage between -40 and -150 V.

4 Discussion

4.1 The influence of Al and Si content on structure and morphology

Recent studies have shown that the Al/Cr ratio is the main factor determining the phase composition of $Al_xCr_{1-x}N$ films [4, 15]. Kawate et al. found the transition from the fcc NaCl-like to the wurtzite structure in the range of x = 0.6 to 0.7 [3]. Soldán et al. have shown that addition of Si at the expense of Cr in an $Al_{0.70}Cr_{0.30}$ target causes an increase of the Al/Cr ratio in the deposited films, consequently resulting in a destabilization of the fcc solid solution [15]. In the present work, only the $Al_{0.70}Cr_{0.25}Si_{0.05}N$ film synthesized at low substrate bias (-40 V) revealed a dual-phase structure, composed of fcc and wurtzite phases (see Fig. 2). This dual-phase structure is established by exceeding the solubility limit of Al in the fcc CrN lattice. Below the solubility limit, a metastable supersaturated fcc AlCrN solid solution exists. For this fcc phase, the lattice parameter decreases with increasing Al content due to the substitution of Cr with the smaller Al atoms [4]. If Si is added to the AlCrN solid solution, it can be incorporated in the fcc lattice either by substitution of Al and/or Cr atoms or by occupying interstitial sites. An assumed substitutional solid solution with Si atoms, which are smaller than the Cr and Al atoms, is expected to be

accompanied by a reduction of its lattice parameter, which is reflected by a peak shift towards higher 2θ angles, as shown in Fig. 2. Since only limited solubility of Si in the fcc AlCrN lattice is assumed, Si atoms must segregate to the grain boundaries when exceeding a critical content [33]. There, they form with N an amorphous SiN_x phase [9, 34]. This is corroborated by the XPS measurements of the Al-Cr-Si-N films revealing the presence of Si-N bonds (Fig. 4). The stoichiometric composition of the films with ~50 at.% N (Table 1) results in the absence of Si-Si bonds in the XPS spectra. The possible evidence of Al-Si and Cr-Si bonds in the low Si-containing Al-Cr-Si-N films also indicates the incorporation of Si in the AlCrN lattice (Fig. 4a). Thus, a nanocomposite structure can be assumed to be formed for sufficient Si contents, consisting of nanocrystalline Al-Cr-(Si)-N grains embedded in an amorphous SiN_x matrix [33, 34]. Formation of such a nanocomposite is driven by a decrease of the total system free energy [34], despite the increased fraction of interface area between Al-Cr-(Si)-N nanocrystals and the amorphous phase [35]. In fact, the formation of complex ternary or quaternary nitride compounds requires a higher mixing enthalpy, which favours formation of the nanocomposite structure [33, 36]. The presence of the SiN_x phase affects significantly the development of film structure and morphology, as it is embedding the Al-Cr-(Si)-N grains and thus hinders their growth. This results in a fine-grained and dense structure characteristic of low crystallinity without pronounced columnar growth (see Figs. 2 and 3). Complete coverage of the Al-Cr-(Si)-N grains by the amorphous SiN_x phase promotes the development of an almost randomly oriented structure and further reduction of grain size. Unlike the single-phase fcc $Al_{0.475}Cr_{0.475}Si_{0.05}N$ film, the dual-phase $Al_{0.70}Cr_{0.25}Si_{0.05}N$ film with the same Si fraction exhibits smaller fcc-AlCrN grains. This restriction in growth of fcc Al-Cr-(Si)-N grains is attributed to the additional formation of the hcp Al-Cr-(Si)-N phase [15].

Changes in the film structure and phase composition affect also the mechanical properties of the Al-Cr-N films. In the case of the Si-free Al-Cr-N films, an increase in hardness with increasing Al content is observed due to solid solution hardening, resulting in a supersaturated solid solution with Al contents close to the solubility limit (see Fig. 8 and Table 1) [4]. The increase of compressive stress caused by the substitution of Cr by Al atoms results in distortion of the Al-Cr-N lattice (Fig. 7), inducing strain in the film. This consequently hinders dislocation movement and thus

increases hardness. On the other hand, the improvement of mechanical properties by addition of Si is attributed to a combination of solid solution hardening and grain size refinement. Incorporation of Si into the fcc Al-Cr-N lattice causes local stress fields and thus increased hardness (Fig. 8). In fact, the residual compressive stress seems to follow a similar trend to hardness for the addition of small amounts of Si (see Figs. 7 and 8), corroborating the assumption that low Si contents are incorporated into the fcc AlCrN phase [37]. The formation of an amorphous SiN_x phase results in grain size refinement and causes an additional hardness increase according to the Hall-Petch relationship [35, 38]. There, the amorphous phase formed at the grain boundaries acts as an effective barrier for dislocation movement [39]. Although the hardness increases up to a certain Si content, the compressive stress decreases (Figs. 7 and 8). This indicates that the hardness enhancement of the nanocomposite Al-Cr-Si-N films cannot be attributed to the compressive stress state alone, but to the formed small randomly oriented Al-Cr-(Si)-N grains and the amorphous SiN_x phase at the grain boundaries, which effectively restrict generation and propagation of dislocations in the film under loading. At higher Si content, film hardness decreases rapidly, as a high volume fraction of SiN_x amorphous phase is formed. This reduces the grain size of the Al-Cr-(Si)-N phase under a critical limit, where grain boundary sliding is enabled (see the $Al_{0.40}Cr_{0.40}Si_{0.20}N$ film in Figs. 3, 7 and 8) [35]. In contrast, the dual-phase $Al_{0.70}Cr_{0.25}Si_{0.05}N$ films exhibit lower hardness with respect to the fcc single-phase films having the same Si content, which is due to the presence of both fcc and the softer hcp phase [3, 15]. The lower compressive stress with respect to the single-phase $Al_{0.475}Cr_{0.475}Si_{0.05}N$ film is attributed to internal relaxation mechanisms, such as phase separation. Moreover, the grain size of this film is below 7 nm, where for a Si content in the coating of 2 at.% (see Table 1) a complete coverage of the grains by an amorphous SiN_x phase is not possible anymore [9]. Thus, hardening by the formation of a nanocomposite structure is negligible and the solid solution hardening effect by incorporation of Si into the fcc AlCrN phase is overcompensated by the formation of the softer wurtzite phase. Hence, the dominating effect on hardness evolution in $Al_{0.70}Cr_{0.25}Si_{0.05}N$ films is the fcc/hcp phase ratio.

4.2 The effect of bias variation on structure and mechanical properties

Phase composition, structure and mechanical properties of Al-Cr-(Si)-N films can be effectively controlled by the deposition parameters. Particularly, the variation of the energy of the incident particles by changing the negative substrate bias significantly affects the growth mechanisms and thus the film properties. The CAE process provides a highly ionized plasma, with metal ions having multiple ionization states [40]. These multiple ion charge states result in higher ion impact energy at the substrate, without applying a high substrate bias voltage [41]. If a substrate bias is applied, depending on their energy, the attracted positive ions give rise to an effectively increased adatom mobility at the film surface, to implantation of evaporated species and to re-sputtering of incorporated atoms [23, 42]. This subsequently affects growth mechanisms through enhanced nucleation, which results in decreased grain size and inhibition of the formation of columnar structures [28]. Moreover, the high energy of incident ions gives rise to increased film density and thus thin films deposited at higher substrate bias voltage are characterised by dense and void-free structure (Fig. 1).

$Al_{0.45}Cr_{0.45}Si_{0.10}N$ and $Al_{0.40}Cr_{0.40}Si_{0.20}N$ films grown at biased substrates reveal exclusively single-phase fcc structure without significant changes in their elemental composition in a wide range of applied substrate bias (Figs. 5a and b). The already mentioned minor influence of ion energy on the elemental composition can be ascribed to a high nitridation level given by deposition in pure N_2 atmosphere at the relatively high total pressure of 3.5 Pa. This indicates that almost all evaporated particles spontaneously react with dissociated nitrogen forming Me-N (Me = Al, Cr) molecules on the film surface, which are in contrast to weakly bonded metallic atoms unlikely to be re-sputtered even under relatively intense high-energetic ion bombardment. The presence of molecules on the growing surface results subsequently in changes of the film texture. The observed loss of the (111) on behalf of (100) texture with increasing bias voltage (Figs. 5a and b) is due to the increasingly effective collisional dissociation of N_2^+ molecules at the growing surface and formation of Me-N molecules [27]. This results in an increased probability of Me atoms being trapped on the thermodynamically more favourable (100) surface, which consequently develops during competitive growth [27]. Moreover, the increased

dissociation of N_2^+ molecules promotes the formation of the SiN_x phase, which additionally affects the texture development of Al-Cr-(Si)-N grains and contributes to a decrease of the average grain size. Since the grain refinement is promoted also by the enhanced ion bombardment increasing the nucleation rate, an interplay of both effects needs to be considered to explain the observed development of small grains without preferred orientation (see Figs. 5a and b).

High-energetic incident ions also result in the displacement of lattice atoms, which typically induces formation of interstitials and vacancies. Thus, under high-energy ion bombardment conditions high defect densities are generated in the films giving rise to high compressive stresses [28]. This high compressive stress state subsequently affects the mechanical properties of the films, as can be seen in a strong relation between hardness (Fig. 8) and residual stress (Fig. 7). All films studied show increasing compressive stress with increasing substrate bias, which is accompanied by increasing hardness. This common dependence can be attributed to the formation of defect-induced stress fields, which act as barriers for dislocation movement, and thus results in enhanced hardness [43]. Moreover, the decreasing grain size fostered by the higher ion energy also promotes the increase of hardness. The decrease of compressive stresses for high Si contents in fcc Al-Cr-(Si)-N nanocomposite films is assumed to originate from the amorphous SiN_x grain boundary phase encapsulating nanocrystalline Me-N grains (Fig. 7).

The development of compressive stress of Al-Cr-Si-N films, however, strongly depends on the phase composition. In the case of dual-phase Al-Cr-Si-N films, lower compressive stress develops with respect to the single-phase films due to the presence of the hexagonal phase. In that case, the separation in fcc and hcp phases promotes stress relaxation. The hexagonal volume fraction is, however, reduced under bombardment of more energetically incident ions stabilizing the metastable fcc phase. Hence, increasing fcc phase fraction and higher defect density promotes higher compressive stress and improved hardness, respectively (Figs. 7 and 8).

5 Conclusions

Microstructure and mechanical properties of Al-Cr-(Si)-N films deposited by cathodic arc evaporation using Al-Cr-Si composite targets are determined by their Al

and Si content, respectively. Metastable supersaturated cubic Al-Cr-N films exhibit increasing hardness and residual compressive stress with Al content increasing up to the solubility limit of AlN in CrN. While low Si contents in the Al-Cr-Si-N films seem to be exclusively incorporated in the fcc Al-Cr-N lattice, a nanocomposite structure consisting of Al-Cr-(Si)-N grains embedded by an amorphous SiN_x phase is formed at higher Si contents. The enhanced hardness of these films, given by a combination of solid solution, Hall-Petch and nanocomposite hardening, is in addition accompanied by reduced residual compressive stress. High Si-containing Al-Cr-Si-N films are characterized by a reduced hardness due to the pronounced fraction of amorphous SiN_x phase.

In summary, the scientific chain between synthesis conditions, resulting structure and properties has been established for Al-Cr-Si-N films grown by cathodic arc evaporation from Al-Cr-Si composite targets.

Acknowledgements

The authors gratefully acknowledge the financial support of the Christian Doppler Society. Additionally, the authors would like to thank the Forschungszentrum Dresden-Rossendorf for providing elastic recoil detection analysis as well as Alexander Fian (Institute of Nanostructured Materials and Photonics, Weiz, Austria) for XPS measurements and support regarding the XPS analysis.

References

[1] P.H. Mayrhofer, G. Tischler, C. Mitterer, Surf. Coat. Technol. 142-144 (2001) 78.

[2] R. Franz, B. Sartory, R. Kaindl, R. Tessadri, A. Reiter, V.H. Derflinger, P. Polcik, C. Mitterer, in: G. Kneringer, P. Rödhammer, H. Wildner (Ed.), Proc. 16th Int. Plansee Seminar, Reutte, Austria, 2005, p. 932.

[3] M. Kawate, A. Kimura, T. Suzuki, J. Vac. Sci. Technol. A 20/2 (2002) 569.

[4] A.E. Reiter, V.H. Derflinger, B. Hanselmann, T. Bachmann, B. Sartory, Surf. Coat. Technol. 200 (2005) 2114.

[5] Y. Makino, K. Nogi, Surf. Coat. Technol. 98 (1998) 1008.

[6] A. Sugishima, H. Kajioka, Y. Makino, Surf. Coat. Technol. 97 (1997) 590.

[7] S. Vepřek, S. Reiprich, Thin Solid Films 268 (1995) 64.

[8] I.-W. Park, D.S. Kang, J.J. Moore, S.C. Kwon, J.J. Rha, K.H. Kim, Surf. Coat. Technol. 201 (2007) 5223.

[9] J. Patscheider, T. Zehnder, M. Diserens, Surf. Coat. Technol. 146-147 (2001) 201.

[10] S.Veprek, M.J.G. Veprek-Heijman, Surf. Coat. Technol. 202 (2008) 5063.

[11] D. Rafaja, M. Dopita, M. Růžička, V. Klemm, D. Heger, G. Schreiber, M. Šíma, Surf. Coat. Technol. 201 (2006) 2835.

[12] T. Polcar, A. Cavaleiro, Surf. Coat. Technol. 206 (2011) 1244.

[13] X.Z. Ding, X.T. Zeng, Y.C. Liu, Thin Solid Films 519 (2011) 1894.

[14] T. Polcar, A. Cavaleiro, Mater. Chem. Phys. 129 (2011) 195.

[15] J. Soldán, J. Neidhardt, B. Sartory, R. Kaindl, R. Čerstvý, P.H. Mayrhofer, R. Tessadri, P. Polcik, M. Lechthaler, C. Mitterer, Surf. Coat. Technol. 202 (2008) 3555.

[16] T.H.D. Keijser, J.I. Lanford, E.J. Mittemeijer, A.B.P. Vogels, J. Appl. Cryst. 15 (1982) 308.

[17] I. Iordanova, P.J. Kelly, R. Mirchev, V. Antonov, Vacuum 81 (2007) 830.

[18] M.H. Mueller, W.P. Chernock, P.A. Beck, Trans. Met. Soc. of AIME 212 (1958) 38.

[19] W.C. Oliver, G.M. Pharr, J. Mater. Res. 7 (1992) 1564.

[20] P.H. Mayrhofer, C. Mitterer, Surf. Coat. Technol. 133-134 (2000) 131.

[21] A. Anders, IEEE Transactions on Plasma Science 29/2 (2001) 393.

[22] A. Flink, T. Larsson, J. Sjölén, L. Karlsson, L. Hultman, Surf. Coat. Technol. 200 (2005) 1535.

[23] R.L. Boxman, P.J. Martin, D.M. Sanders, Handbook of Vacuum Arc Science and Technology: Fundamentals and Application, Noyes Publ., New Jersey, 1995.

[24] Powder Diffraction File (Card 00-025-1495 for fcc-AlN, Card 00-011-0065 for fcc-CrN, Card 00-025-1133 for w-AlN), International Center for Powder Diffraction Data, ICDD, PDF-2/Release 2007, 2007.

[25] Binding energies for relevant bonds obtained from the La Surface XPS database, http://www.lasurface.com/database/elementxps.php, 06/2012

[26] D. Briggs, M.P. Seah, Practical surface analysis, John WILEY & SONS, 1993.

[27] R. Daniel, K.J. Martinschitz, J. Keckes, C. Mitterer, J. Phys. D: Appl. Phys. 42 (2009) 075401.

[28] I. Petrov, P.B. Barna, L. Hultman, J.E. Greene, J. Vac. Sci. Technol. A 21/5 (2003) 117.

[29] F. Vaz, L. Rebouta, P. Goudeau, T. Girardeau, J. Pacaud, J.P. Riviére, A. Traverse, Surf. Coat. Technol. 146-147 (2001) 274.

[30] H. Oettel, R. Wiedemann, Surf. Coat. Technol. 76-77 (1995) 265.

[31] H. Oettel, R. Wiedemann, S. Preißler, Surf. Coat. Technol. 74-75 (1995) 273.

[32] M. Pfeiler, K. Kutschej, M. Penoy, C. Michotte, C. Mitterer, M. Kathrein, Surf. Coat. Technol. 202 (2007) 1050.

[33] J.L. Endrino, S. Palacín, M.H. Aguirre, A. Gutiérrez, F. Schäfers, Acta Mater. 55 (2007) 2129.

[34] S. Vepřek, Thin Solid Films 317 (1998) 449.

[35] E. Arzt, Acta Mater. 46 (1998) 5611.

[36] S. Vepřek, A.S. Argon, Surf. Coat. Technol. 146-147 (2001) 175.

[37] M. Pfeiler, J. Zechner, M. Penoy, C. Michotte, C. Mitterer, M. Kathrein, Surf. Coat. Technol. 203 (2009) 3104.

[38] J. Musil, Surf. Coat. Technol. 125 (2000) 322.

[39] A. Flink, PhD, PhD Thesis, Linköping Studies in Science and Technology, Dissertation No. 1190, Linköping University, Sweden, 2008, Linköping University, Sweden, 2008.

[40] A. Anders, Cathodic Arcs-From Fractal Spots to Energetic Condensation, Springer, New York, 2008.

[41] U. Helmersson, M. Lattemann, J. Bohlmark, A.P. Ehiasarian, J.T. Gudmundsson, Thin Solid Films 513 (2006) 1.

[42] R. Daniel, K.J. Martinschitz, J. Keckes, C. Mitterer, Acta Mater. 58 (2010) 2621.

[43] J.-E. Sundgren, Thin Solid Films 128 (1985) 21.

9 Publication II

Publication II

Oxidation behavior of arc evaporated Al-Cr-Si-N thin films

C. Tritremmel, P.H. Mayrhofer, R. Daniel, M. Lechthaler, P. Polcik and C. Mitterer

Journal of Vacuum Science & Technology A, 30 (6) (2012) 061501/6

Oxidation behavior of arc evaporated Al-Cr-Si-N thin films

C. Tritremmel, R. Daniel and C. Mitterer

Christian Doppler Laboratory for Advanced Hard Coatings, Department of Physical Metallurgy and Materials Testing, Montanuniversität Leoben, Franz-Josef-Strasse 18, A-8700 Leoben, Austria

P.H. Mayrhofer

Christian Doppler Laboratory for Application Oriented Coating Development, Department of Physical Metallurgy and Materials Testing, Montanuniversität Leoben, Franz-Josef-Strasse 18, A-8700 Leoben, Austria

M. Lechthaler

OC Oerlikon Balzers AG, Iramali 18, LI-9496 Balzers, Principality of Liechtenstein

P. Polcik

PLANSEE Composite Materials GmbH, Siebenbürgerstrasse 23, D-86983 Lechbruck am See, Germany

ABSTRACT

The impact of Al and Si on the oxidation behavior of Al-Cr-(Si)-N thin films synthesized by arc evaporation of powder metallurgically prepared Al_xCr_{1-x} targets with x = Al/(Al+Cr) of 0.5, 0.6 and 0.7 and $(Al_{0.5}Cr_{0.5})_{1-z}Si_z$ targets with Si contents of z = 0.05, 0.1 and 0.2 in N_2 atmosphere was studied in detail by means of differential scanning calorimetry, thermo-gravimetric analysis (TGA), X-ray diffraction and Raman spectroscopy. Dynamical measurements in synthetic air (up to 1440 °C) revealed the highest onset temperature of pronounced oxidation for nitride coatings prepared from the $Al_{0.4}Cr_{0.4}Si_{0.2}$ target. Isothermal TGA at 1100, 1200, 1250 and 1300 °C highlight the pronounced improvement of the oxidation resistance of $Al_xCr_{1-x}N$ coatings by the addition of Si. The results show that Si promotes the formation of a dense coating morphology as well as a dense oxide scale when exposed to air.

Keywords: Oxidation; Al-Cr-N; Al-Cr-Si-N; Thin films, Thermo-gravimetric analysis

I. INTRODUCTION

Hard protective coatings for tools used in various machining and forming applications are characterized by a high hardness, wear and oxidation resistance. Especially in machining applications, the coatings are exposed to extreme working loads, such as high temperatures (even above 1000 °C at the cutting edge) combined with severe mechanical and corrosive environment.

CrN-based coatings show excellent mechanical properties together with high oxidation resistance and thermal stability. Alloying CrN with Al has proven to further enhance these properties when remaining in the face centered cubic (fcc) crystal structure [1-3]. The fcc $Al_xCr_{1-x}N$ solid solution, having the NaCl (B1) crystal type, can be synthesized for Al contents up to x = 0.67-0.8 [2,4]. For Al contents above this metastable solubility limit, the hexagonal close packed (hcp) ZnS (wurtzite type) structure is preferred. The maximum solubility limit for AlN in the fcc structure strongly depends on the used deposition conditions and techniques due to their e.g., inherent available film growth kinetics. While single phase fcc Al-Cr-N coatings are known for their excellent mechanical properties, wear and oxidation resistance, single phase hcp coatings with high Al contents exhibit a better thermal stability [5]. For specific applications, where the thermal load is not dominating, a small fraction of hexagonal phases within a fcc phase dominated Al-Cr-N coating can be beneficial, as this results in the formation of a dense coating [5]. Due to the available nucleation sites, such coatings exhibit an earlier phase separation towards the stable constituents w-AlN and fcc-CrN [6].

CrN coatings typically start to oxidize at ~750 °C by the formation of a thin protective chromium oxide layer [7]. The improved oxidation resistance of Al-Cr-N coatings (onset temperature of pronounced oxidation above 900 °C [1,8] is based on the formation of an aluminum-rich outer oxide scale inhibiting the inward diffusion of oxygen [3]. Hofmann and Jehn [9] have found by Auger electron spectroscopy depth profile analysis of oxidized Al-Cr-N coatings that with increasing temperature the Al content of the outer oxide scale decreases and the Cr content increases. Consequently, as many applications require a thermal stability above 900 °C a further improvement of Al-Cr-N films is needed.

Based on numerous studies, silicon is a very promising candidate whenever an improved hardness and thermal stability is required [10-12]. Due to extremely limited solubility of Si in various transition metal nitrides, the addition of Si causes a pronounced grain refinement and densification of the overall coating structure based on the formation of a dense, amorphous SiN_x grain boundary phase [13]. Furthermore, the high cohesive strength of the SiN_x phase results in a hardness increase [13,14]. As Si promotes the formation of dense oxides, the oxidation resistance of nitride coatings can be improved due to the addition of Si, similar to aluminum [15-18]. Based on these previous studies, we investigate in this study the effect of Si addition (up to 16 at.% of the metal sublattice) on the oxidation resistance of Al-Cr-N films having Al/Cr ratios of 1 and 2.8. For comparison, Al-Cr-N films having different Al contents are studied as well.

II. EXPERIMENTAL DETAILS

Various $Al_xCr_{1-x}N$ and $(Al_xCr_{1-x})_{1-z}Si_zN$ thin films were synthesized in an industrial scale deposition system INNOVA (OC Oerlikon Balzers) by cathodic arc evaporation (CAE) of powder-metallurgically prepared $Al_{0.5}Cr_{0.5}$, $Al_{0.6}Cr_{0.4}$, $Al_{0.7}Cr_{0.3}$, and $Al_{0.475}Cr_{0.475}Si_{0.05}$, $Al_{0.45}Cr_{0.45}Si_{0.1}$, $Al_{0.4}Cr_{0.4}Si_{0.2}$, and $Al_{0.7}Cr_{0.25}Si_{0.05}$ targets (diameter 150 mm and thickness 12 mm, target composition is given in at.% fraction) in N_2 atmosphere. All depositions were carried out with using four of the six arc evaporation sources, which were equipped with identical targets to promote homolithically grown coatings. In order to avoid substrate interference during the oxidation tests, mirror-polished sapphire substrates ($10\times4\times0.5$ mm^3), ultrasonically cleaned in acetone and ethanol, were used for the deposition. The base pressure of the chamber was always $\leq 1x10^{-3}$ Pa, before heating to 500 °C and etching the substrates in a pure Ar plasma with ions extracted from an additional arc discharge. After the heating and etching process, the deposition chamber was filled with N_2 (purity of $\geq$ 99.8%) to the desired working gas pressure of 3.5 Pa. The current on each target used for arc evaporation was set to 140 A. All deposition runs were carried out for a duration of 60 min using two-fold substrate rotation (~37 seconds per carousel revolution) and a substrate bias potential of -40 V, resulting in a coating thickness of 3 ± 0.3 µm.

The oxidation tests were performed in a simultaneous thermal analyzer (Netzsch-STA 409C, combining differential scanning calorimetry, DSC, and thermo-gravimetric analyses, TGA), equipped with a quadrupole mass spectrometer (QMS) through a skimmer coupling system. Prior to each oxidation run, the measuring chamber was evacuated to 1 Pa and then re-filled with oxygen or synthetic air (80 mol.% N_2, 20 mol.% O_2) to atmospheric pressure. Dynamical analyses to 1440 °C were carried out with a heating rate of 5 K/min to determine the onset temperature for pronounced oxidation. At selected temperatures, where the dynamical DSC and TGA curves exhibit distinct features, additional isothermal STA studies were conducted. During all investigations the mass spectrometer was set to monitor the atomic mass units for N_2 (28) and O_2 (32).

Energy-dispersive electron probe microanalysis (EDX, Oxford Instruments INCA Energy 200) was used to determine the coating composition in the as deposited state and to analyze the oxidized samples. Structural investigations of as deposited and oxidized coatings were performed by X-ray diffraction (XRD) using a D8 Advance diffractometer (Bruker AXS) equipped with parallel beam optics and Sol-X detector. The XRD patterns were recorded in the grazing incidence configuration using CuKα radiation and a 2° grazing incidence angle. The grain size in the as-deposited films was determined from the broadening of the XRD peaks by a single-line method using the Pseudo-Voigt function [19]. The hardness of the as-deposited films was measured by means of nanoindentation using an ultra-micro indentation system (UMIS, Fischer-Cripps Laboratories) and was evaluated from at least 30 load-displacement curves in the load range from 5 to 20 mN after the Oliver and Pharr method [20]. The maximum indentation depth was always below 10% of the coating thickness to avoid the effect of the underlying substrate. The substrate curvature method was used to determine the biaxial stress state in the as-deposited films, which was calculated via the modified Stoney equation [21]. A scanning electron microscope (SEM, FEI Quanta 200 Mk2) was used to study the morphology and thickness of the oxide scale, operating in a low vacuum mode to account for their low electrical conductivity. By using a Jobin Yvon Labram confocal-Raman spectrometer equipped with a frequency-doubled Nd-YAG laser (532.2 nm, 100 mW) at room temperature in ambient air, the oxidized coatings were investigated to identify oxidation products.

III. RESULTS AND DISCUSSION

A summary of the elemental composition, microstructure, hardness and biaxial stress state of the as deposited $Al_xCr_{1-x}N$ and $(Al_xCr_{1-x})_{1-z}Si_zN$ coatings is given in Table I. The N content, detected by ERDA (elastic recoil detection analysis), is between 49 and 52 at.%. For easier reading, their notation was chosen to refer to stoichiometric nitrides. The highest Al/Cr ratio is obtained for the coating prepared from the $Al_{0.7}Cr_{0.25}Si_{0.05}$ target, which exhibits a microstructure composed of fcc and hcp phases. All other coatings investigated crystallize in the single-phase fcc structure. With Si content increasing from 4 to 16 at.% of the metal sublattice in the fcc coatings, their grain size decreases from 34 to 6 nm, their compressive stress decreases from -1.00 to -0.35 GPa, and their hardness first increases from 26 to 36 GPa for $Al_{0.42}Cr_{0.50}Si_{0.08}N$ and then decreases to 30 GPa for $Al_{0.39}Cr_{0.45}Si_{0.16}N$. Selected coatings with properties summarized in Table I were chosen for further studies on their oxidation resistance as they provide different Al and Si contents for single-phase fcc and dual-phase fcc+hcp microstructures.

Table I: Summary of crystal structure, grain size, hardness and biaxial macro-stress of the coatings investigated.

Film composition	Crystal structure	Grain size [nm]	Hardness [GPa]	σ [GPa]
$Al_{0.47}Cr_{0.53}N$	fcc	34	26	-1.00
$Al_{0.56}Cr_{0.44}N$	fcc	35	30	-0.55
$Al_{0.67}Cr_{0.33}N$	fcc	37	30	-1.15
$Al_{0.43}Cr_{0.53}Si_{0.04}N$	fcc	22	32	-1.05
$Al_{0.42}Cr_{0.50}Si_{0.08}N$	fcc	16	36	-0.90
$Al_{0.39}Cr_{0.45}Si_{0.16}N$	fcc	6	30	-0.35
$Al_{0.68}Cr_{0.28}Si_{0.04}N$	fcc+hcp	7	28	-0.95

A. Dynamical thermo-gravimetric analysis in oxygen

Figures 1(a), (b) and (c) present the specific weight gain, and the simultaneously monitored MS signals for N_2 and O_2, respectively, during dynamical heating of fcc $Al_{0.43}Cr_{0.53}Si_{0.04}N$ up to 1440 °C. These studies were conducted in O_2 atmosphere, rather than synthetic air, to allow for a detection of the N_2 signal caused by N-release from the coatings due to the oxidation process and dissociation of N bonded to Cr, Al or Si. For annealing temperatures (T_a) below 950 °C, only a small N_2 signal can be detected, as well as no significant change in weight. Further increase in temperature (>1000 °C) causes an increased N_2 signal. Earlier studies clearly showed, that this is connected with the breaking of Cr-N bonds within Al-Cr-N coatings, leading to the formation of h-Cr_2N and further to body centered cubic Cr [22], when the temperature increases further. At temperatures above 1250 °C, the N_2 signal rapidly increases with T_a. Here, also the O_2 signal decreases, although the measurements were conducted in flowing O_2 atmosphere, thus indicating a pronounced O_2 uptake by the coating. These processes, i.e. N_2 release and O_2 uptake, will cause the sample weight to decrease and increase, respectively. Hence, TGA measurements can only account for the dominating mechanism. If an $Al_xCr_{1-x}N$ coating is fully oxidized to $(Al_xCr_{1-x})_2O_3$, the weight gain should be 37%. As during our TGA measurements the weight of the sample is almost unchanged up to temperatures of 1300 °C, although N_2-release and O_2 uptake can be detected, the released N_2 is not solely due to the transformation of the nitride into the oxide, but also due to dissociation of Cr-N bonds. The latter effect is especially dominant at temperatures above 1350 °C, where the mass even decreases, see Fig. 1. This proofs that the oxidation process is retarded by the formation of a dense oxide. To account for application-near conditions, further oxidation studies were conducted in synthetic air.

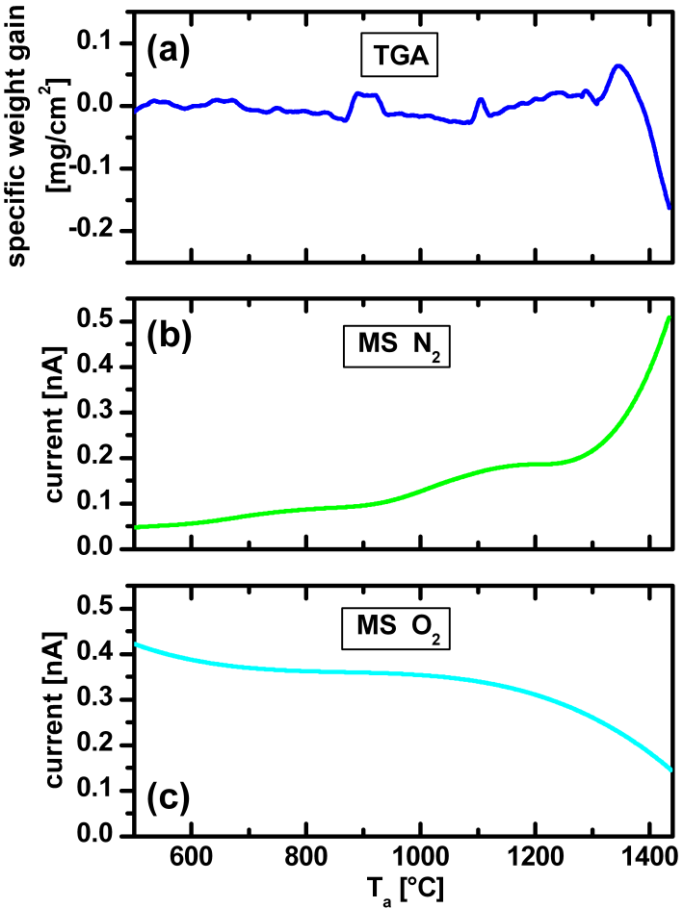

Figure 1: Dynamical measurements of $Al_{0.43}Cr_{0.53}Si_{0.04}N$ up to 1440 °C in oxygen atmosphere. (a) TGA, (b) mass spectrometer signal of N_2 and (c) mass spectrometer signal of O_2.

B. Dynamical thermo-gravimetric analysis in synthetic air

Dynamical TGA in synthetic air up to 1440 °C of $Al_{0.47}Cr_{0.53}N$, $Al_{0.56}Cr_{0.44}N$, $Al_{0.67}Cr_{0.33}N$, $Al_{0.43}Cr_{0.53}Si_{0.04}N$, $Al_{0.42}Cr_{0.50}Si_{0.08}N$, $Al_{0.39}Cr_{0.45}Si_{0.16}N$ and $Al_{0.68}Cr_{0.28}Si_{0.04}N$ coatings clearly suggests the onset of pronounced oxidation to take place in the temperature range between 1100 and 1325 °C (Fig. 2). These onset temperatures are much higher when comparing to other metal nitride systems like CrN, TiN, TiAlN [7,23,24]. For the Si-free $Al_xCr_{1-x}N$ coatings, the detectable onset temperature is not directly connected with the Al content. In principle, two effects can account for this behavior. Increasing the Al content will result in an increased oxidation resistance, whereas an increasing Cr content will result in an increasing

Cr-N dissociation driven weight loss (i.e. by N_2 release). Unambiguously, the oxidation resistance can be improved by the addition of Si to the single-phase fcc coatings [16]. This positive effect of Si on the oxidation resistance can not be observed for $Al_{0.68}Cr_{0.28}Si_{0.04}N$, as this coating exhibits already in the as deposited state a mixed fcc and hcp microstructure. Hence, this coating shows an earlier phase separation towards its stable constituents due to the pre-existing nucleation sites as mentioned above. Comparable results have been published by Willmann et al. [6]. Endrino et al. observed improved oxidation resistance also for $Al_{0.678}Cr_{0.278}Si_{0.046}N$ [25] coatings, as these have been single phase cubic structured (by using a higher bias potential of -100 V [16]) in the as deposited state and hence provided less diffusion paths. Especially, the formation of hcp AlN with the connected increase in specific volume of ~26% [26] will result in a massive increase of defects or even cracks and thereby promote oxidation. Based on the results obtained by dynamical TGA, further isothermal DSC and TGA are conducted for 1, 4 and 8 h, at 1100, 1200, 1250, and 1300 °C.

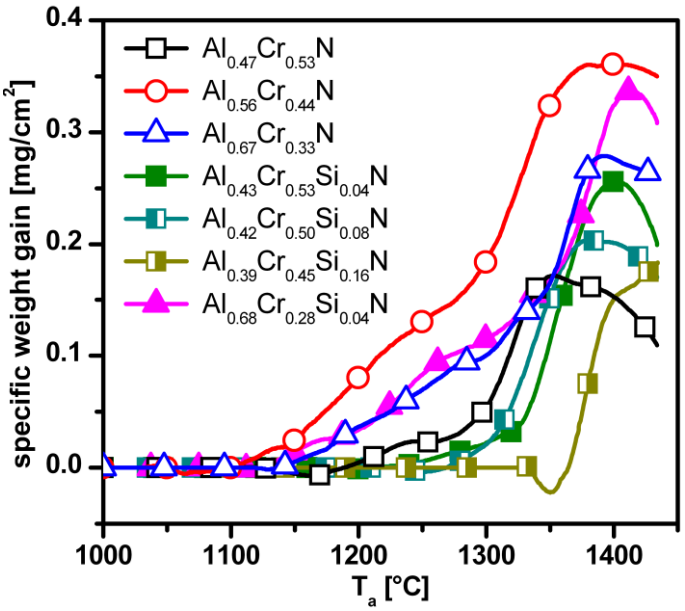

Figure 2: Dynamical TGA measurements of $Al_{0.47}Cr_{0.53}N$, $Al_{0.56}Cr_{0.44}N$, $Al_{0.67}Cr_{0.33}N$, $Al_{0.43}Cr_{0.53}Si_{0.04}N$, $Al_{0.42}Cr_{0.50}Si_{0.08}N$, $Al_{0.39}Cr_{0.45}Si_{0.16}N$ and $Al_{0.68}Cr_{0.28}Si_{0.04}N$ coatings up to 1440 °C in synthetic air.

C. Isothermal thermo-gravimetric analysis in synthetic air

The baseline-corrected DSC scan at 1300 °C of the $Al_{0.39}Cr_{0.45}Si_{0.16}N$ coating [see Fig. 3(a)], which exhibits the highest onset temperature for oxidation during dynamical investigations (see Fig. 2), is composed of exothermic and endothermic contributions. Together with the simultaneously detected mass evolution, the isothermal changes versus time can be divided into three regions I, II and III. During the first ~90 min, region I, the exothermic contribution and the weight gain indicate an oxidation processes dominated period. This is followed by region II (from 90 to 140 min) where no weight change can be detected. Here, the DSC signal suggests an increasing contribution of endothermic reactions, basically the dissociation of N bonded to Cr [6]. During the following period (140 to 240 min) this dissociation and hence the N_2 release is dominating, resulting in a weight loss. These results clearly demonstrate that simple weight measurements after thermal exposure, especially of Cr-N bonds containing materials, can lead to an incorrect conclusion of no changes in the coating. Therefore, it is of vital importance to vary both temperature and time when investigating the oxidation behavior. The measured weight of the $Al_{0.39}Cr_{0.45}Si_{0.16}N$ sample after oxidation at 1100, 1200, 1250, and 1300 °C for 1, 2 and 4 h also suggests competing reactions involving weight-loss and weight gain [see Fig. 3(b)].

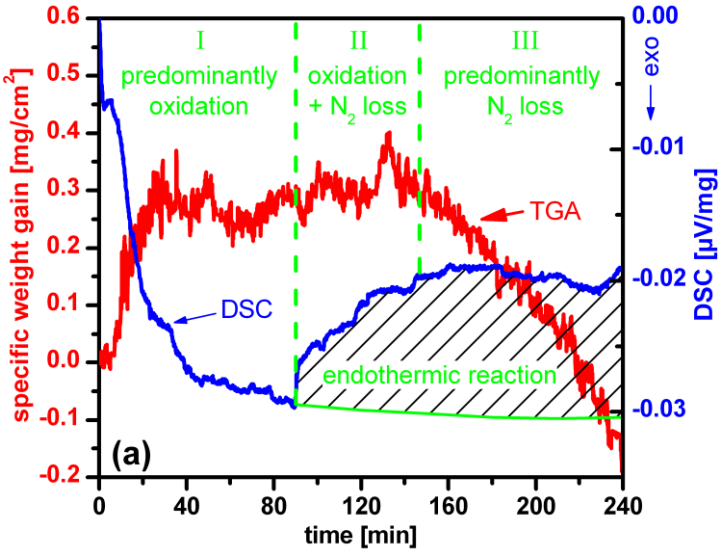

Figure 3(a): Isothermal DSC and TGA signals of $Al_{0.39}Cr_{0.45}Si_{0.16}N$ in synthetic air at 1300 °C for the duration of 4 h.

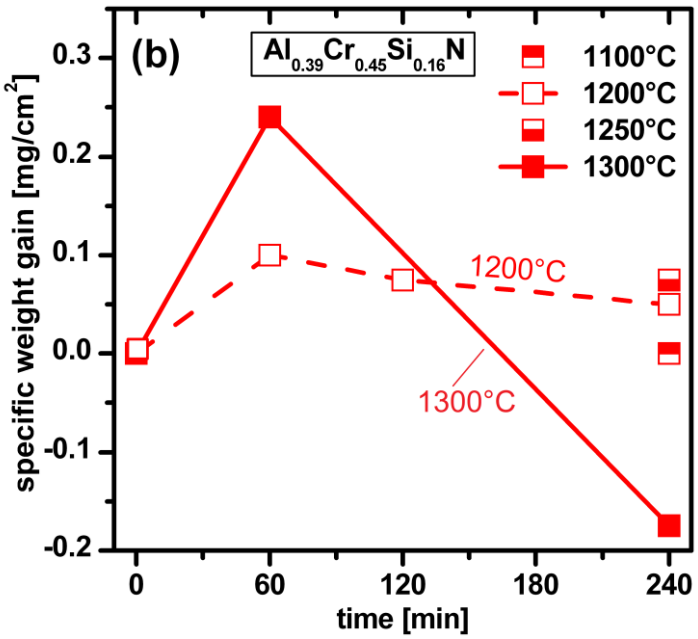

Figure 3(b): Specific weight gain of $Al_{0.39}Cr_{0.45}Si_{0.16}N$ after annealing at different temperatures and exposure times.

The TGA signals detected for $Al_{0.47}Cr_{0.53}N$ [Fig. 4(a)], $Al_{0.67}Cr_{0.33}N$ [Fig. 4(b)] and $Al_{0.42}Cr_{0.50}Si_{0.08}N$ [Fig. 4(c)] during isothermal exposure in synthetic air at 1100, 1200, 1250, and 1300 °C explicitly show the complex thermal behavior of this type of coating. As indicated already during the dynamical studies, especially the high Cr containing film [Fig. 4(a)] exhibits a pronounced interaction between weight gain due to oxidation and weight loss due to dissociation of Cr-N bonds. The TGA results suggest that this effect can be significantly retarded by higher Al contents and the addition of Si, compare Figs. 4(a), (b) and (c).

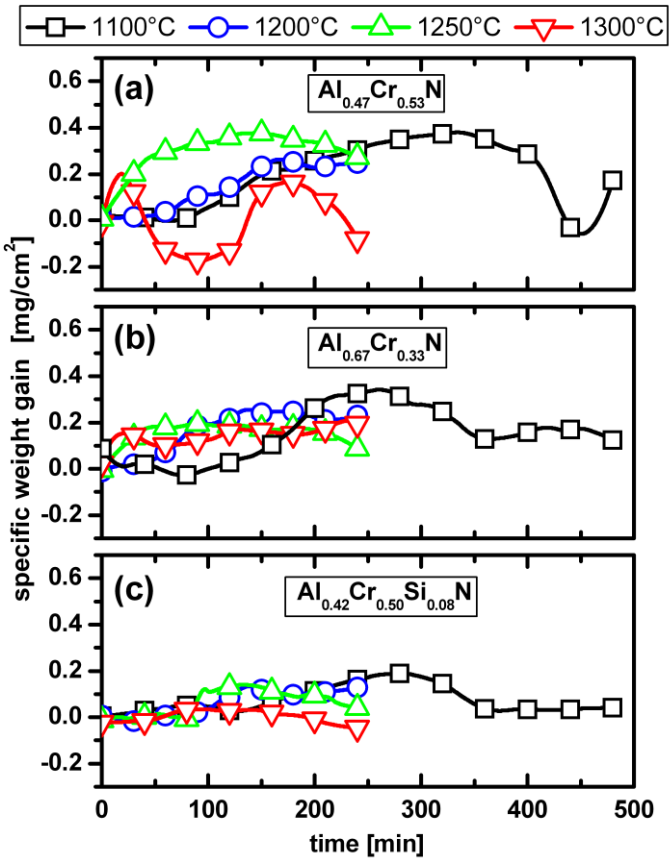

Figure 4: TGA signals during isothermal annealing in synthetic air at temperatures between 1100 and 1300 °C for (a) $Al_{0.47}Cr_{0.53}N$, (b) $Al_{0.67}Cr_{0.33}N$ and (c) $Al_{0.42}Cr_{0.50}Si_{0.08}N$.

XRD analyses of the coatings after isothermal oxidation at 1250 °C and 4 h, Fig. 5, clearly demonstrate the positive influence of Si on promoting the formation of a crystalline corundum type mixed $(Al_xCr_{1-x})_2O_3$ oxide [27]. Whereas the Si-free coatings show an oxide scale composed of Cr-rich and Al-rich $(Al_xCr_{1-x})_2O_3$ [9,28] [see

the broad peak in Fig. 5(a)], resulting in a small grain size due to competitive growth (or layered oxide structure [29]) and hence an increased grain boundary fraction, only a single $(Al_xCr_{1-x})_2O_3$ oxide phase can be detected for the Si-alloyed coatings [see Fig. 5(b)].

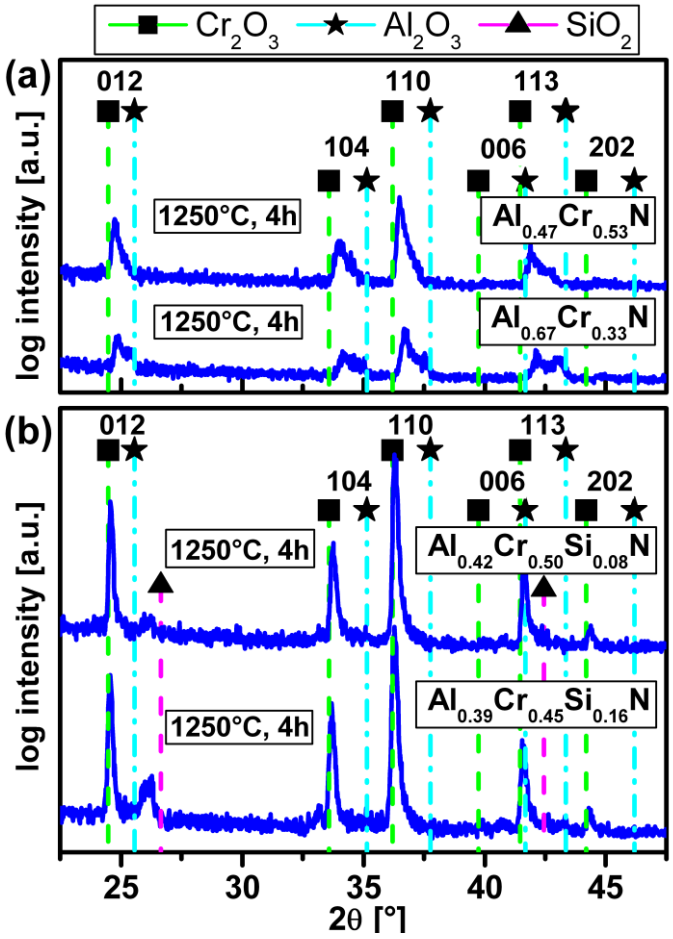

Figure 5: XRD patterns of coatings annealed at 1250 °C for 4 h in synthetic air. (a) $Al_{0.47}Cr_{0.53}N$ and $Al_{0.67}Cr_{0.33}N$ and (b) $Al_{0.42}Cr_{0.50}Si_{0.08}N$ and $Al_{0.39}Cr_{0.45}Si_{0.16}N$.

This is also valid for lower and higher oxidation temperatures, see the XRD pattern of $Al_{0.39}Cr_{0.45}Si_{0.16}N$ after oxidation at 1100, 1200 and 1300 °C (Fig. 6). Growth of the latter, more complex oxide needs a significantly higher onset temperature than for the Si-free oxide scale, see Fig. 2. Furthermore, the XRD pattern recorded after 4 h exposure at 1100 °C in Fig. 6(a) suggests the formation of a crystalline SiO_2 phase in addition to $(Al_xCr_{1-x})_2O_3$ [27].

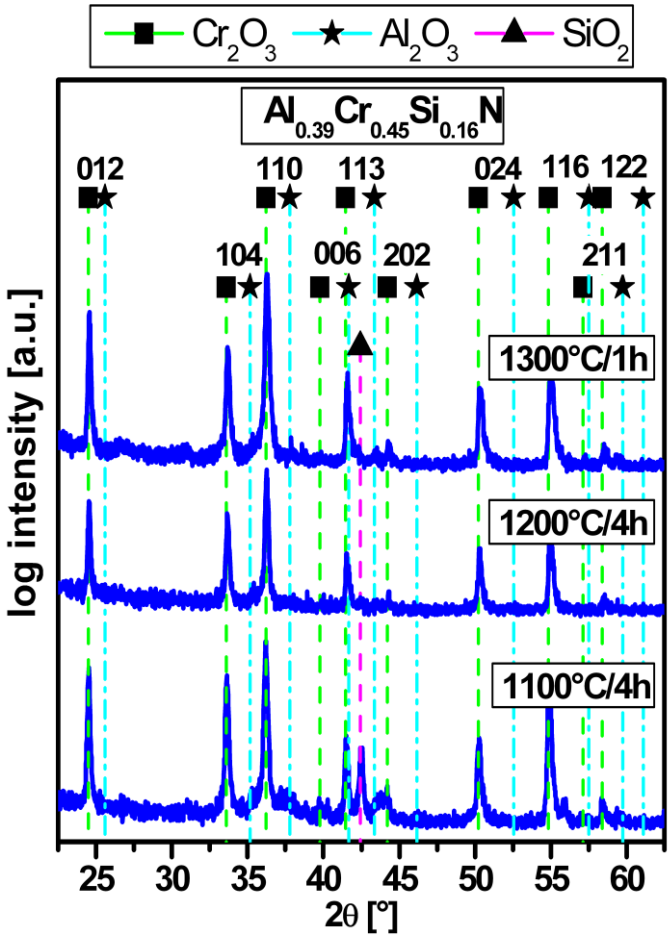

Figure 6: XRD patterns of $Al_{0.39}Cr_{0.45}Si_{0.16}N$ after annealing in synthetic air at 1100 °C (4 h), 1200 °C (4 h) and 1300 °C (1 h).

Raman measurements of the afore discussed $Al_{0.47}Cr_{0.53}N$, $Al_{0.67}Cr_{0.33}N$, $Al_{0.42}Cr_{0.50}Si_{0.08}N$ and $Al_{0.39}Cr_{0.45}Si_{0.16}N$ coatings after oxidation for 4 h at 1200 °C show a pronounced difference between Si-free and Si-containing coatings (Fig. 7). Whereas the outermost oxide scale for the Si-free $Al_{0.47}Cr_{0.53}N$ and $Al_{0.67}Cr_{0.33}N$ coatings is dominated by corundum type Al_2O_3, the Raman shift of the Si-containing $Al_{0.42}Cr_{0.50}Si_{0.08}N$ and $Al_{0.39}Cr_{0.45}Si_{0.16}N$ coatings suggest the formation of a mixed Cr_2O_3-Al_2O_3 oxide scale, in agreement to the XRD studies. Furthermore, especially for the high Si containing film, SiO_2 formation can be confirmed.

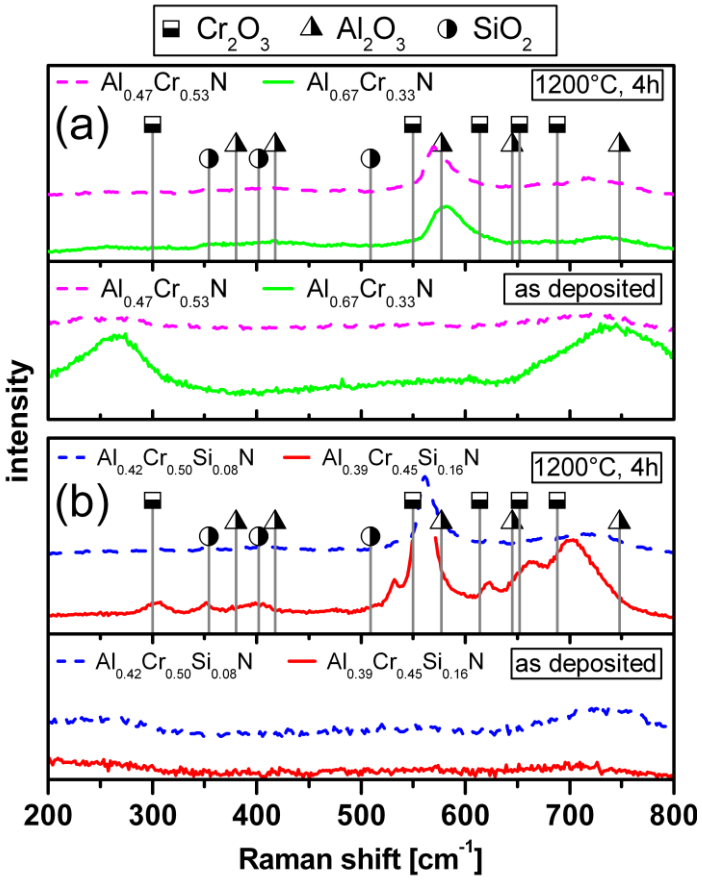

Figure 7: Raman spectra of coatings in the as deposited state and after annealing at 1200 °C for 4 h in synthetic air. (a) $Al_{0.47}Cr_{0.53}N$ and $Al_{0.67}Cr_{0.33}N$ and (b) $Al_{0.42}Cr_{0.50}Si_{0.08}N$ and $Al_{0.39}Cr_{0.45}Si_{0.16}N$.

IV. CONCLUSIONS

The study has shown that the oxidation behavior of cathodic arc evaporated Al-Cr-N and Al-Cr-Si-N films is strongly influenced by their Al and Si content, respectively. The highest onset temperature for oxidation accompanied with the lowest weight gain was found for the $Al_{0.39}Cr_{0.45}Si_{0.16}N$ coating. While the formation of a crystalline corundum type mixed and/or layered $(Al_xCr_{1-x})_2O_3$ oxide scale at the surface determines the oxidation resistance in Al-Cr-N coatings, the Al-Cr-Si-N coatings are characterized by a single $(Al_xCr_{1-x})_2O_3$ oxide phase at the surface, inhibiting further oxidation. $Al_{0.39}Cr_{0.45}Si_{0.16}N$ coatings additionally form a crystalline SiO_2 phase in addition to $(Al_xCr_{1-x})_2O_3$ during exposure in synthetic air. As a consequence, the oxidation rate in $Al_{0.39}Cr_{0.45}Si_{0.16}N$ films is determined by the slowly

growing dense oxide scale composed of $(Al_xCr_{1-x})_2O_3$ and SiO_x. The onset temperature of oxidation is increased from 1100 °C for $Al_{0.56}Cr_{0.44}N$ to 1325 °C for $Al_{0.39}Cr_{0.45}Si_{0.16}N$ coatings. Consequently, the $Al_{0.39}Cr_{0.45}Si_{0.16}N$ coating is a promising candidate for high temperature applications in oxidizing atmosphere.

ACKNOWLEDGEMENTS

The authors highly acknowledge the financial support of the Christian Doppler Society as well as the Österreichische Forschungsförderungsgesellschaft and the Bundesministerium für Wirtschaft, Familie und Jugend within the Research Studio Austria energy-drive.

REFERENCES

[1] Y. Ide, T. Nakamura, and K. Kishitake, Proceedings of the Second International Conference on Processing Materials for Properties, edited by B. Mishra and C. Yamauchi, 2000, pp. 291.

[2] M. Kawate, A. Kimura, and T. Suzuki, J. Vac. Sci. Technol. A **20** (2), 569 (2002).

[3] A.E. Reiter, C. Mitterer, and B. Sartory, J. Vac. Sci. Technol. A **25** (4), 711 (2007).

[4] Y. Makino and K. Nogi, Surf. Coat. Technol. **98**, 1008 (1998).

[5] A.E. Reiter, V.H. Derflinger, B. Hanselmann, T. Bachmann, and B. Sartory, Surf. Coat. Technol. **200**, 2114 (2005).

[6] H. Willmann, P.H. Mayrhofer, P.O.Å. Persson, A.E. Reiter, L. Hultman, and C. Mitterer, Scripta Materialia **54**, 1847 (2006).

[7] P.H. Mayrhofer, H. Willmann, and C. Mitterer, Surf. Coat. Technol. **146-147**, 222 (2001).

[8] M. Kawate, A.K. Hashimoto, and T. Suzuki, Surf. Coat. Technol. **165**, 163 (2003).

[9] S. Hofmann and H.A. Jehn, Werkst. Korros. **41**, 756 (1990).

[10] S. Veprek and M. J.G. Veprek-Heijman, Surf. Coat. Technol. **202**, 5063 (2008).

[11] D. Rafaja, M. Dopita, M. Růžička, V. Klemm, D. Heger, G. Schreiber, and M. Šíma, Surf. Coat. Technol. **201**, 2835 (2006).

[12] T. Polcar and A. Cavaleiro, Surf. Coat. Technol. **206**, 1244 (2011).

[13] J. Patscheider, T. Zehnder, and M. Diserens, Surf. Coat. Technol. **146-147**, 201 (2001).

[14] S. Vepřek, P. Nesládek, A. Niederhofer, F. Glatz, M. Jílek, and M. Šíma, Surf. Coat. Technol. **108-109**, 138 (1998).

[15] M. Diserens, J. Patscheider, and F. Lévy, Surf. Coat. Technol. **120-121**, 158 (1999).

[16] J.L. Endrino, G.S. Fox-Rabinovich, A. Reiter, S.V. Veldhuis, R.Escobar Galindo, J.M. Albella, and J.F. Marco, Surf. Coat. Technol. **201**, 4505 (2007).

[17] J. Endrino and V. Derflinger, Patent No. EP 1 771 602 B1 (2006).

[18] T. Polcar and A. Cavaleiro, Mater. Chem. Phys. **129**, 195 (2011).

[19] T.H.D. Keijser, J.I. Lanford, E.J. Mittemeijer, and A.B.P. Vogels, J. Appl. Cryst. **15**, 308 (1982).

[20] W.C. Oliver and G.M. Pharr, J. Mater. Res. **7**, 1564 (1992).

[21]P.H. Mayrhofer and C. Mitterer, Surf. Coat. Technol. **133-134**, 131 (2000).

[22]P.H. Mayrhofer, F. Rovere, M. Moser, C. Strondl, and R. Tietema, Scr. Mater. **57**, 249 (2007).

[23]W.D. Münz, J. Vac. Sci. Technol. A **4** (6), 2717 (1986).

[24]L.A. Donohue, I. J. Smith, W.-D. Münz, I. Petrov, and J.E. Greene, Surf. Coat. Technol. **94-95**, 226 (1997).

[25]J.L. Endrino, S. Palacín, M.H. Aguirre, A. Gutiérrez, and F. Schäfers, Acta Mater. **55**, 2129 (2007).

[26]P.H. Mayrhofer, H. Willmann, and A.E. Reiter, Surf. Coat. Technol. **202**, 4935 (2008).

[27]Powder Diffraction File (Card 00-038-1479 for Cr_2O_3, Card 01-070-5679 for Al_2O_3, Card 00-005-0490 for SiO_2), International Center for Powder Diffraction Data, ICDD, PDF-2/Release 2007 (2007).

[28]O. Banakh, P.E. Schmid, R. Sanjinés, and F. Lévy, Surf. Coat. Technol. **163-164**, 57 (2003).

[29]F. Rovere, P.H. Mayrhofer, A. Reinholdt, J. Mayer, and J.M. Schneider, Surf. Coat. Technol. **202**, 5870 (2008).

10 Publication III

Publication III

Microstructure and mechanical properties of nanocrystalline Al-Cr-B-N thin films

C. Tritremmel, R. Daniel, M. Lechthaler, H. Rudigier, P. Polcik, C. Mitterer

Surface & Coatings Technology, 213 (2012) 1-7

Microstructure and mechanical properties of nanocrystalline Al-Cr-B-N thin films

C. Tritremmel[1] , R. Daniel[2], M. Lechthaler[3], H. Rudigier[3], P. Polcik[4], C. Mitterer[1,2]

[1] Christian Doppler Laboratory for Advanced Hard Coatings at the Department of Physical Metallurgy and Materials Testing, Montanuniversität Leoben, Franz-Josef-Strasse 18, A-8700 Leoben, Austria
[2] Department of Physical Metallurgy and Materials Testing, Montanuniversität Leoben, Franz-Josef-Strasse 18, A-8700 Leoben, Austria
[3] OC Oerlikon Balzers AG, Iramali 18, LI-9496 Balzers, Liechtenstein
[4] PLANSEE Composite Materials GmbH, D-86963 Lechbruck, Germany

Abstract

Al-Cr-N is a well-established hard film system with excellent mechanical and tribological properties. The effect of B addition on structure and mechanical properties of Al-Cr-N films grown by cathodic arc evaporation was systematically investigated. The B content in the targets was varied between 10 and 30 at.% at a constant Al/Cr atomic ratio of 1.8. X-ray diffraction revealed that all coatings exhibit a face-centered cubic structure, with texture and grain size affected by B content and substrate bias voltage. X-ray photoelectron spectroscopy indicates formation of a nanocomposite structure consisting of a crystalline face-centered cubic Al-Cr-(B)-N solid solution and an amorphous BN_x phase. Nanoindentation experiments revealed a significant hardness enhancement of Al-Cr-(B)-N with respect to B-free films, accompanied with a reduction of residual compressive stress.

Keywords: Al-Cr-N; Thin films; Microstructure; Nanocomposite; Mechanical properties

1 Introduction

The ever increasing demand arising from high speed machining applications for protective films having high hardness, good wear resistance and increased thermal stability has led to the development of Al-Cr-N thin films [1-3]. Ternary Al-Cr-N coatings exist either in the metastable face-centered cubic B1 (fcc) structure of CrN or, by exceeding the metastable solubility limit, the thermodynamically stable wurtzite

B4 structure of AlN with dual-phase structures slightly above the solubility limit [1]. Due to the high solubility limit of Al in the fcc CrN lattice, the ternary metastable fcc $Al_xCr_{1-x}N$ exists over a wide composition range up to $x = 0.6 - 0.8$ [1, 4, 5]. In general, the fcc modification is favored in industrial applications due to its improved mechanical and tribological properties compared to wurtzite $Al_xCr_{1-x}N$ [1, 3]. Although Al-Cr-N films are successfully used, there is still a need for increased tool performance and life time. In fact, there are a variety of options to improve mechanical and tribological properties of Al-Cr-N films. A common method improving film properties like hardness is to increase the energetic ion bombardment during film deposition, however, with the drawback of additional effects including higher compressive stress, which is typically accompanied with reduced film adhesion [6, 7]. However, synthesis of film materials having multilayer or nanocomposite structure seems more promising. In the case of nanometer-sized multilayers, alternating layers with different composition and a layer thickness below 10 nm results in improved film properties such as high hardness or increased toughness [8]. Nanocomposite films are of increasing interest due to the possibility to synthesize materials with unique structure resulting in outstanding properties like superhardness, toughness and/or increased wear resistance [8, 9]. It has been shown that a nanocomposite structure may form in transition metal nitride films by addition of alloying elements like Si or B. Increasing Si content in Ti-Si-N films thus results in formation of a compound consisting of TiN nanocrystals embedded in an amorphous Si_3N_4 phase [10, 11]. Recent publications on cathodic arc evaporated Al-Cr-Si-N films revealed the positive effect of Si addition on mechanical properties and oxidation resistance [12, 13]. Also B has shown to improve the mechanical properties in Al-Cr-B-N coatings [14, 15]. Similarly, Baker et al. observed improved performance for nanocomposite Ti-Al-B-N films, consisting of nanocrystalline TiAlN grains separated by an compliant intergranular amorphous (a) BN phase [16].

In the present study, metastable fcc Al-Cr-B-N films with constant Al/Cr atomic target ratio (~1.8) and varying B content (10 - 30 at.% in the target) deposited at different substrate bias voltages were investigated in order to examine the influence of B content in cathodic arc evaporated Al-Cr-B-N films on their microstructure and mechanical properties such as hardness and residual stress state. X-ray photoelectron spectroscopy (XPS) and nanostructural characterization by means of

transmission electron microscopy (TEM) were in addition used to investigate the possible formation of a nanocomposite structure in the Al-Cr-B-N films.

2 Experimental details

The Al-Cr-B-N films were prepared by cathodic arc evaporation (CAE) in a commercial Oerlikon Balzers deposition system (Innova) with a base pressure of 5×10^{-4} Pa, where four out of six sources were equipped with powder-metallurgically prepared Al-Cr-B targets (PLANSEE Composite Materials GmbH). The Al/Cr atomic ratio in the targets was kept constant at ~1.8 with varying B content of 10, 20 and 30 at.%. In addition, B-free Al-Cr-N films with an Al/Cr atomic ratio of 1.5 and 2.3 were synthesized under identical deposition conditions to provide a reference for Al-Cr-B-N films. The substrates, mirror-polished Si(100) strips and cemented carbide cutting inserts (WC - 6% Co) mounted on the two-fold rotating holder, were heated to 500 °C and etched for approximately 30 min in a pure Ar plasma with ions extracted from an additional gas discharge. During deposition the chamber was filled with pure nitrogen to a pressure of 3.5 Pa and the current on each arc source was set to 150 A. Furthermore, the coil current of the magnet system on the back of the targets was individually adjusted (varied between 1.1 A and 1.6 A for B contents in the target increasing from 10 to 30 at.%) to obtain the most effective utilization of the target. The Al-Cr-B-N films were grown on substrates biased to a constant value of -40 or -100 V. The deposition time was adjusted in order to obtain a typical film thickness of 3 ± 0.2 µm.

The crystal structure of the films was examined by means of X-ray diffraction (XRD) using a D8 Advance diffractometer (Bruker AXS) in θ-θ geometry, equipped with a Göbel mirror on the primary side and an energy-dispersive Sol-X detector on the secondary side. The coated samples were scanned with a Cu Kα primary beam operated at a voltage of 40 kV and a current of 40 mA. The grain size (size of coherently diffracting domains) was estimated from the broadening of the diffraction peaks by a single line method using the Pseudo-Voigt function [17]. The microstructure and the morphology of the films were investigated by scanning electron microscopy (SEM) using a Zeiss EVO 50. Raman spectroscopy was additionally used to study the structural development of the Al-Cr-B-N films. The spectra were recorded with a Jobin Yvon Labram confocal-Raman spectrometer

equipped with a frequency-doubled Nd-YAG laser (532.2 nm, 100mW) at room temperature in ambient air. The elemental composition of the Al-Cr-B-N films was determined by elastic recoil detection analysis (ERDA) using a 35 MeV Cl^{7+} ion beam and a Bragg ionization detector. A detailed microstructural analysis of Al-Cr-B-N films was performed by TEM using a FEI TITAN. The chemical bonding structure of the Al-Cr-B-N films was studied by means of XPS with an Omicron Multiprobe system, equipped with a monochromised Al Kα beam of 1486.6 eV and a resolution of <0.5 eV. Prior to the measurement, the samples were sputter cleaned with 2 keV Ar-ions to remove volatile surface contaminants. The Unifit 2002 program was used to deconvolute the N1s core level spectra [18].

The biaxial stress state in the films was evaluated from the optical substrate curvature measurements in the temperature range of 25 – 600 °C by the modified Stoney equation [19]. The intrinsic and thermal stresses were extracted from the measured total stress following the procedure described in [20]. Hardness measurements were accomplished using a UMIS nanoindenter (Fischer-Cripps Laboratories) equipped with a Berkovich diamond tip. Calibration measurements on a fused silica specimen were used to determine the actual shape of the tip. The maximum applied load was in the range between 5 and 25 mN to avoid the influence of the substrate and not less than 30 load-displacement curves were used to get reliable hardness values [21].

3 Results

All deposited films are well adherent to the Si strips and cutting inserts, irrespective of the applied substrate bias voltage. The elemental composition of the Al-Cr-B-N films biased to -100 V, as measured by ERDA, is summarized in Table 1. All Al-Cr-B-N films reveal a nearly stoichiometric composition with respect to the $\frac{N}{Al+Cr+B}$ ratio. However, the Al/Cr metal ratios of the as-deposited films differ significantly from the target composition. A loss of ~5 at.% Al, especially for the films with 2.3 and 5.7 at.% B in the target, was observed, which is most likely associated to gas scatter effects during transport from the target to the substrate [22]. This results in a reduced Al/Cr ratio in the film with respect to the target (see Table 1). The scattering effect is even more pronounced for B, showing a loss by a factor of ~50 %

with respect to the target composition. This behavior is attributed to the low average ionization state of B (+1) compared to Cr (+2.1) and Al (+1.7) [23], giving rise to enhanced B loss [12].

Table 1: Elemental composition of Al-Cr-B-N films deposited at -100 V substrate bias, as determined by ERDA.

Target		**Film**					
Elemental composition [at.%]	Al/Cr	**Elemental composition**				Al/Cr	**Elemental composition [at.%]**
		N [at.%]	**Al [at.%]**	**Cr [at.%]**	**B [at.%]**		
$Al_{0.58}Cr_{0.32}B_{0.10}$	1.80	49.3	26.7	21.7	2.3	1.20	$Al_{0.53}Cr_{0.43}B_{0.04}N$
$Al_{0.52}Cr_{0.28}B_{0.20}$	1.85	48.8	22.9	22.6	5.7	1.00	$Al_{0.45}Cr_{0.44}B_{0.11}N$
$Al_{0.45}Cr_{0.25}B_{0.30}$	1.80	47.7	22.7	20.5	9.1	1.10	$Al_{0.43}Cr_{0.39}B_{0.18}N$

SEM micrographs of film surfaces and fracture cross-sections are shown in Fig. 1 for Al-Cr-B-N films synthesized at a substrate bias of -100 V. Fracture cross-sections (Figs. 1(d)-(f)) indicate that all films are dense and present a rather featureless morphology, without any evidence of columnar growth. The density and size of droplets, a typical feature of the deposition technique used [24], increases with increasing B content and results in increased surface roughness of the film (see Figs. 1(a)-(c)). Micrographs of Al-Cr-B-N films deposited at a substrate bias of -40 V (not shown here) show even higher droplet density, which indicates that the droplet density is not only depending on target composition but also on the deposition conditions.

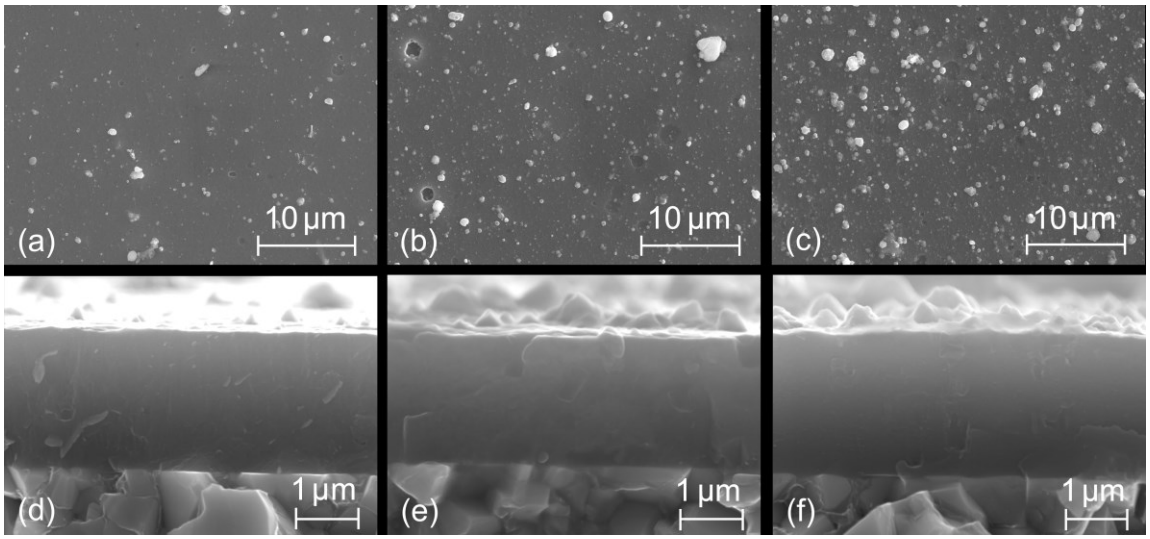

Figure 1: SEM plan-view and cross-sectional micrographs of Al-Cr-B-N films with 2.3 at.% B (a, d), 5.7 at.% B (b, e) and 9.1 at.% B (c, f), deposited on cemented carbide substrates at -100 V substrate bias.

The evolution of the microstructure of Al-Cr-B-N films with various compositions is illustrated by the XRD patterns in Fig. 2. All films consist of a crystalline $Al_xCr_{1-x}N$ phase corresponding to the fcc NaCl-type structure irrespective of B content and applied substrate bias voltage. In addition, also the formation of a BN_x phase is likely, although this phase is due to its often amorphous character not visible in the XRD pattern. The diffraction peaks of the fcc-$Al_xCr_{1-x}N$ phase have been reported to be situated between fcc-AlN and fcc-CrN [25], which reflects the formation of a metastable solid solution where Cr is substituted by Al in the CrN lattice. The shift to lower 2θ angles can be attributed to the high compressive stress caused by the high substrate bias voltage of -100 V. B addition does apparently not affect the formation of this solid solution, nevertheless its influence on texture evolution is evident. Al-Cr-B-N films with 2.3 at.% B grow predominantly with (111) preferred orientation and exhibit low-intensity diffraction peaks corresponding to (100)- and (110)-oriented grains. A higher amount of B in the film (5.7 at.%) causes a reduction of the (111) preferred orientation by promoting the growth of (100)- and (110)-oriented grains. Further increase of B content to 9.1 at.% results in random orientation of grains. The addition of B into the Al-Cr-N films is furthermore associated with a loss of intensity due to the reduced radiation absorption, the broadening of the diffraction peaks and a peak shift towards higher 2θ angles with respect to the fcc CrN positions. While the

increase of peak width with increasing B content is mainly associated with a reduction of grain size, the observed peak shift is assumed to correspond to a change of residual stress. Since the Al/Cr ratio was kept constant in all films, the peak shift to higher 2θ angles corresponds to a reduction of the compressive stress. This is besides the effect of B addition also promoted by the reduction of the energy of film forming species at the lower bias voltage of -40 V.

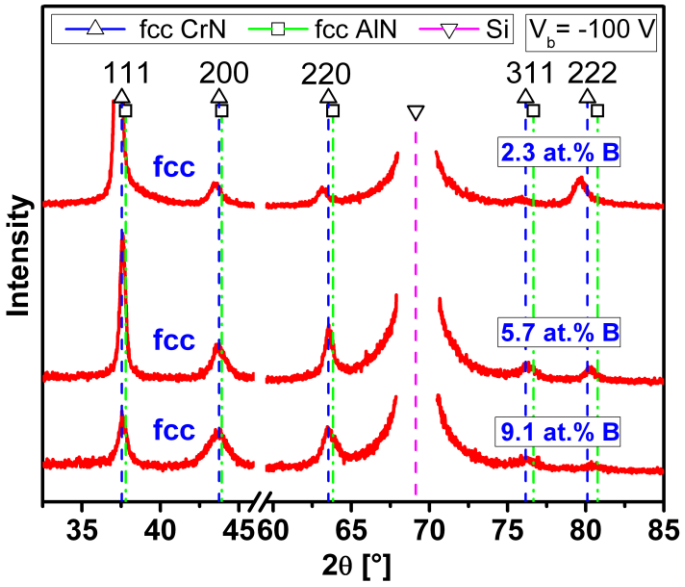

Figure 2: Effect of the B content on structure and orientation of Al-Cr-B-N films deposited at -100 V substrate bias, as revealed by XRD measurements.

The broadening of the XRD peaks mentioned above was analyzed to estimate the mean grain size of the fcc phase in Al-Cr-B-N films. The variation of the grain size as a function of the B content and substrate bias voltage is depicted in Fig. 3. For comparison, the grain size of B-free Al-Cr-N films with Al/Cr ratios in the target of 1.5 and 2.3, synthesized at -40 V substrate bias, is also shown. While the influence of the Al/Cr ratio on the grain size of Al-Cr-N films is only minor, resulting in a mean crystallite size between 34 and 37 nm, B addition significantly influences the grain size development. The addition of 2.3 at.% B into the film does not significantly affect the grain size. However, higher B contents resulted in a dramatic decrease, reaching values close to ~7 nm for 9.1 at.% B in the film. Fig. 3 also shows the effect of the bias voltage on the development of the grain size of Al-Cr-B-N films. Its influence is

evident for the Al-Cr-B-N film with 2.3 at.% B, revealing a decrease of the grain size from ~40 to ~20 nm by increasing the bias voltage from -40 to -100 V. For the higher B contents, only slight variations of the grain size with increasing ion energy were obtained.

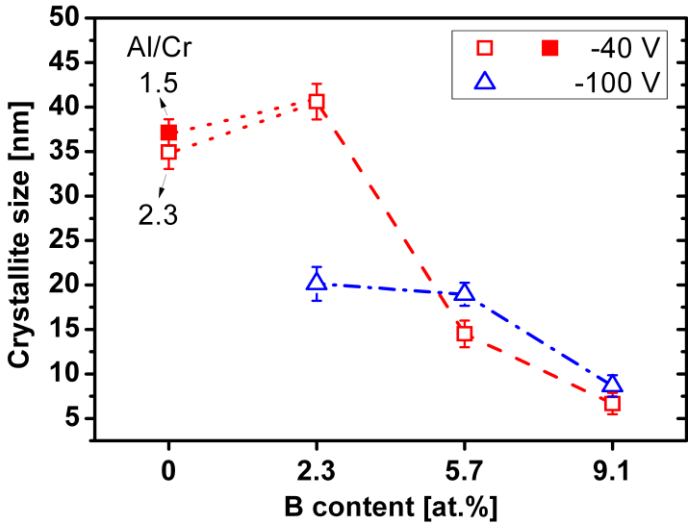

Figure 3: Influence of the B content and substrate bias voltage on the mean crystallite size in Al-Cr-B-N films with 2.3, 5.7 and 9.1 at.% B deposited at -40 V and -100 V substrate bias, respectively.

The Raman spectra of Al-Cr-B-N films synthesized at -40 and -100 V substrate bias are displayed in Fig. 4. All spectra reveal two broad bands at ~250 and ~750 cm^{-1}, which can be assigned to the fcc-$Al_xCr_{1-x}N$ phase [26]. All peaks are shifted towards lower wave number with increasing B content, irrespective of applied substrate bias voltage (Figs. 4(a) and (b)). Moreover, a higher B content causes a loss in the peak intensity accompanied with a significant peak broadening indicating a reduction of the grain size. Similar to the XRD investigations, the increasing ion energy results in a shift of bands towards lower wave numbers, which indicates increasing compressive stress due to the enhanced formation of defects in the films [26].

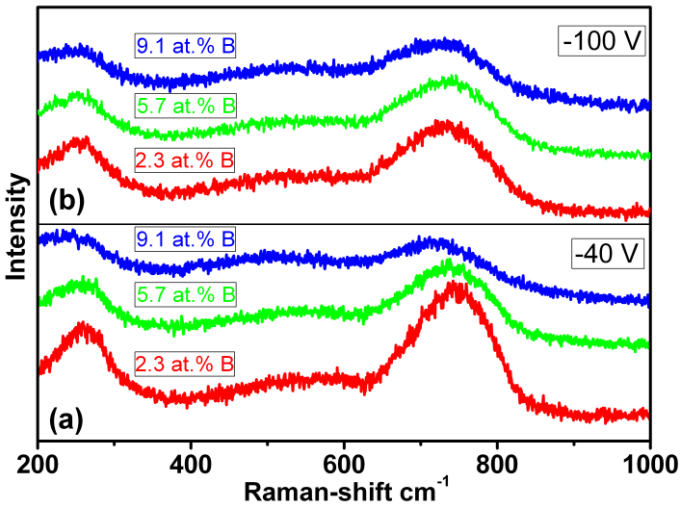

Figure 4: Raman spectra of Al-Cr-B-N films with 2.3, 5.7 and 9.1 at.% B in the target, deposited at substrate bias voltages of -40 V (a) and -100 V substrate bias (b).

XPS measurements of the Al-Cr-B-N films synthesized at -100 V substrate bias were conducted to obtain additional information about the chemical bonding state. All relevant core level spectra, in particular N1s, Cr2p, Al2p and B1s, were analyzed in terms of binding energies of the contributing bonding configurations. The main constituents were identified as Cr-N and Al-N [27]. The B1s and N1s core level spectra of Al-Cr-B-N films with various B content deposited at -100 V are shown in Fig. 5(a) and (b). Since all samples were sputter cleaned prior to analysis, the spectra are almost free of oxidation-related contaminations (see the negligible small B-O peak in the energy range of 191.5 – 192.5 eV) [28]. The main component in the B1s spectra (Fig. 5(a)) is the B-N peak with a maximum at 190 eV [29]. In addition, a smaller B-N peak is obvious at a binding energy of ~187 eV [28]. It is also evident from the spectra, that the increasing B content is associated with an increase of the intensity and fraction of the B-N peak. This can be interpreted by an increasing fraction of a-BN_x phase with increasing B content. The N1s spectra in Fig. 5(b) show peaks originating from N-Al (396.4 eV) [30], N-Cr (396.6 eV) [29] and N-B (397.9 eV) [29]. A detailed inspection of the peak shape indicates increasing intensity of the right shoulder of the N-(Al, Cr) peak, which corresponds to an increase of the peak area of N-B bindings. This corroborates the trend of the B-N peak with increasing B content in Fig. 5(a).

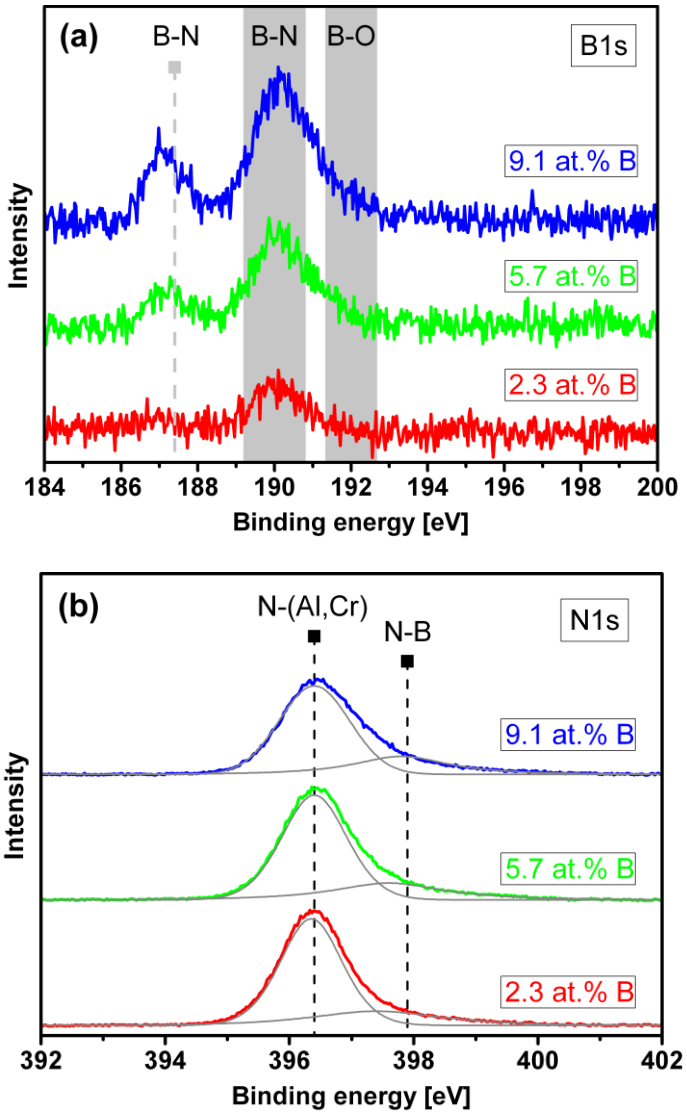

Figure 5: XPS core level spectra of Al-Cr-B-N films with 2.3, 5.7 and 9.1 at.% B, deposited at a substrate bias voltage of -100 V on a Si (100) substrate. (a) B1s and (b) N1s. The intensity in (a) is magnified by a factor of 10 compared to (b).

An additional detailed study of the nanostructure of the as-deposited Al-Cr-B-N films was performed by means of TEM. Figure 6 shows a bright-field cross-sectional high-resolution TEM micrograph with corresponding selected area electron diffraction (SAED) pattern of the Al-Cr-B-N film with 5.7 at.% B grown at -40 V bias. The SAED pattern shows reflections corresponding only to the fcc-$Al_xCr_{1-x}N$ phase, as already revealed by XRD. The blurred SAED rings of the Al-Cr-B-N films with 5.7 at.% B in the target are due to nano-sized Al-Cr-(B)-N crystallites and they also reflect small fractions of highly disordered or even amorphous regions located between the

crystallites. Inferred from XPS measurements (Fig. 5) these regions may be assumed as a-BN_x phase.

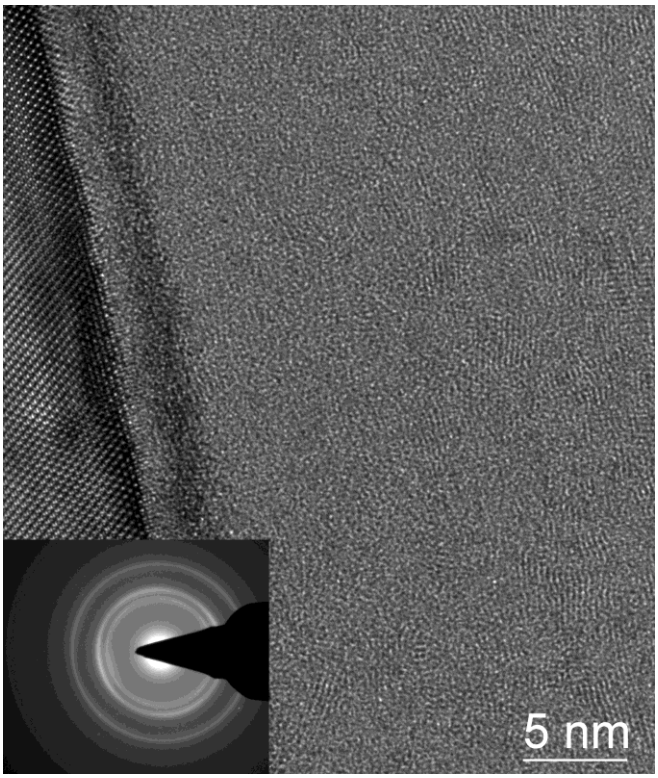

Figure 6: Cross-sectional high-resolution TEM micrograph of the Al-Cr-B-N film with 5.7 at.% B grown at -40 V substrate bias, along with its respective SAED pattern.

In order to investigate the stress state of the synthesized Al-Cr-B-N films, substrate curvature biaxial stress temperature measurements were performed in the range between room temperature (RT) and 600 °C. The residual stress (σ_{tot}) of Al-Cr-B-N films in their as-deposited state as a function of B content and substrate bias voltage is depicted in Fig. 7(a). It is obvious that the addition of B into Al-Cr-N films results in a significant reduction of compressive stress. While the B-free Al-Cr-N films with Al/Cr target ratios of 1.5 and 2.3 grown at a bias voltage of -40 V exhibit -0.5 and -1.2 GPa compressive stress, respectively, a B content of 2.3 at.% in the film results in a compressive stress decrease to -0.2 GPa. With further increase of the B content, the residual stress remains in the range of -0.2 to +0.2 GPa (see the full symbols in Fig. 7(a) for a bias voltage of -40 V). Due to enhanced defect

generation at higher ion energies, the compressive stress increases to ~1 - 1.5 GPa at -100 V (open symbols in Fig. 7(a) for a bias voltage of -100 V); however, the stress development with increasing B content is similar to -40 V. The residual stress decreases from -1.6 GPa to -0.7 GPa with the B concentration increasing from 2.3 to 9.1 at.%. More detailed information about the individual components of the residual stress is given in Fig. 7(b). In general, residual stress in thin films comprises intrinsic σ_i, thermal σ_{th} and extrinsic σ_e stress components, where the latter one can be neglected due to the absence of phase transformations or interfacial stress in the investigated films [7, 20]. The intrinsic stress σ_i generated during film growth is compressive and decreases with increasing B content from -3 GPa for B-free Al-Cr-N films to -0.6 GPa in the Al-Cr-B-N film with 9.1 at.% B (-40 V bias, see Fig. 7(b)). On the other hand, the thermal stress generated in the films during cooling from deposition temperature T_d (500 °C) to RT is tensile and decreases with increasing B content from 1.7 GPa to 0.4 GPa (Fig. 7(b)), due to the thermal expansion coefficient (TEC) mismatch between film ($\alpha_{Al\text{-}Cr\text{-}B\text{-}N}$ = ~5 - 6 $\times$ 10^{-6} K^{-1}, as calculated from the slope of the stress-temperature curve in Fig. 7(c) between RT and T_d) and substrate (α_{Si} = 2.6 $\times$ 10^{-6} K^{-1} [20]). An increase of the substrate bias voltage results in a significant increase of the intrinsic σ_i stress from -0.8 to -1.5 GPa with decreasing B content (Fig. 7(b)). In contrast, the thermal component is almost unaffected by the ion energy. Typical stress-temperature curves in the range of RT to 600 °C of Al-Cr-B-N films with a B content varying between 2.3 and 9.1 at.%, synthesized at -100 V substrate bias, are shown in Fig. 7(c). It is evident, that the slope of the linear thermo-elastic part up to 500 °C decreases with increasing B content. This indicates that the TEC of Al-Cr-B-N films decreases with increasing B content. The observed deviation from the linear behavior above the T_d reflects changes in the film structure due to defect recovery processes activated above T_d [20].

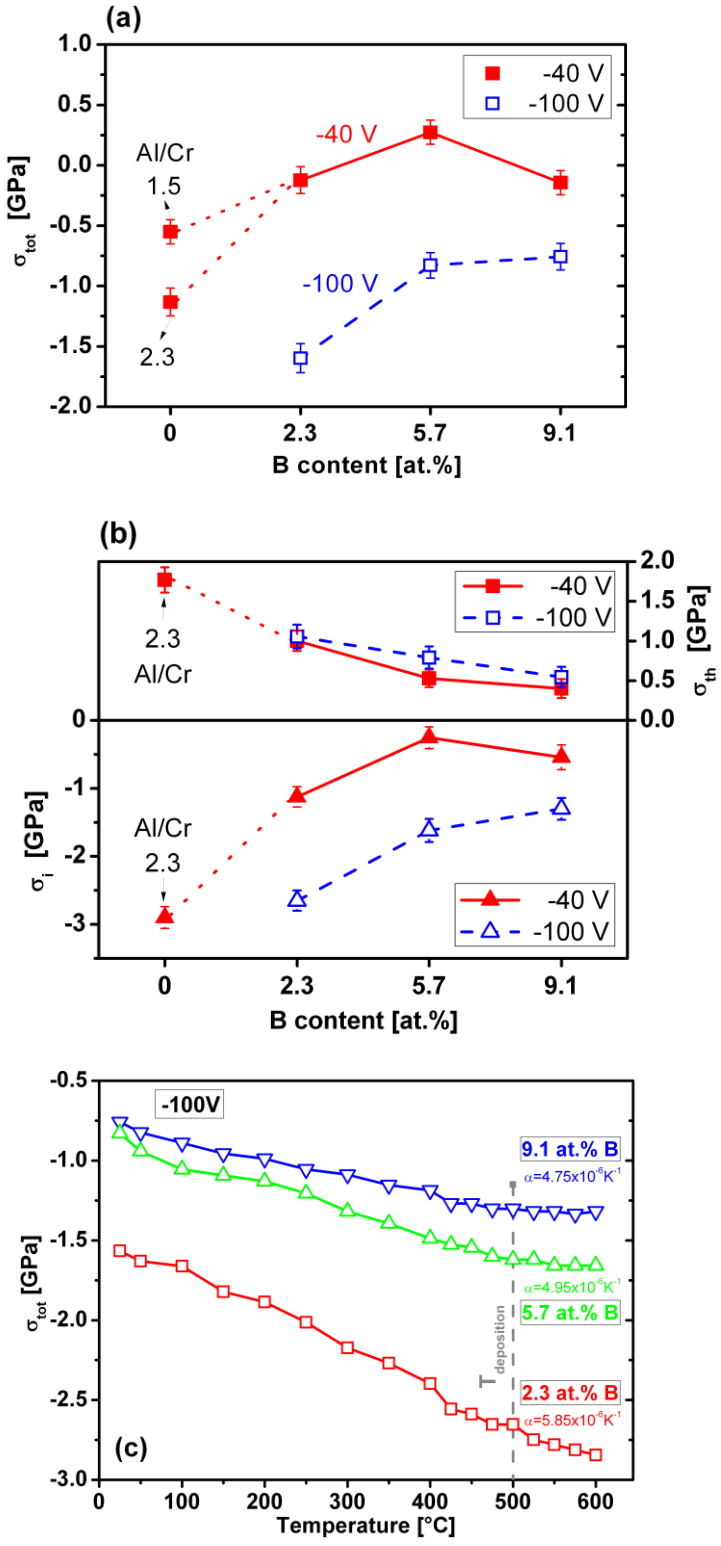

Figure 7: Development of (a) the total residual stress σ_{tot} and (b) the intrinsic σ_i and thermal stress σ_{th} of Al-Cr-B-N films with B contents of 2.3, 5.7 and 9.1 at.% deposited at -40 V and -100 V substrate bias grown on Si (100) substrates. In addition, stress components of B-free Al-Cr-N films are shown. (c) Stress-temperature plots of Al-Cr-B-N films with 2.3, 5.7 and 9.1 at.% B in the target deposited at a substrate bias voltage of -100 V.

Values of hardness and Young's modulus of Al-Cr-N and Al-Cr-B-N films, as determined by nanoindentation, are displayed in Fig. 8. The Al-Cr-B-N films deposited with a substrate bias of -40 V reveal a hardness in the range from 33 to 41 GPa, where the maximum was observed for Al-Cr-B-N films with 2.3 and 5.7 at.% B. A further increasing B content reduces the hardness to 32 GPa at 9.1 at.%. This is, however, still higher than the hardness of B-free Al-Cr-N films (Al/Cr target ratios of 1.5 and 2.3), which varies between 26 and 30 GPa. The development of the Young's modulus follows a similar trend as the hardness. The highest modulus of 625 GPa was observed for the Al-Cr-B-N films with 2.3 at.% B in the target, irrespective of the bias voltage, decreasing with increasing B content to 425 GPa at 9.1 at.%, which is comparable to the Young's modulus of B-free Al-Cr-N. Hardness of Al-Cr-B-N films with 2.3 at.% B increases from 41 to 43 GPa by increasing the substrate bias from -40 V to -100 V, whereas hardness of Al-Cr-B-N films with higher B content remains unaffected by increasing the ion energy.

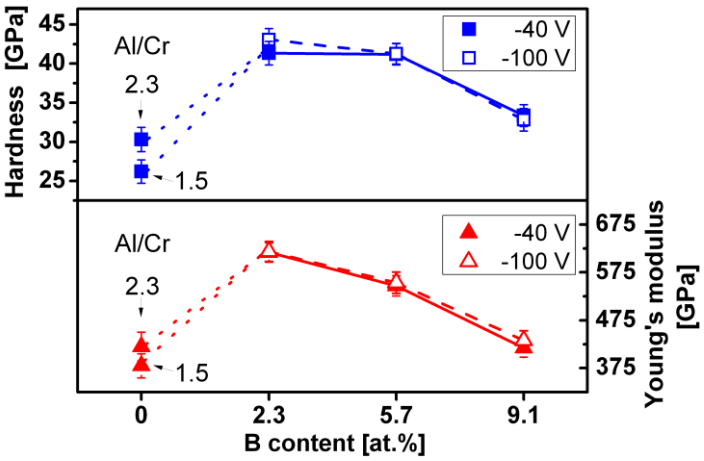

Figure 8: Hardness and Young's modulus of Al-Cr-B-N films with 0, 2.3, 5.7 and 9.1 at.% B deposited at -40 and -100 V substrate bias on cemented carbide substrates.

4 Discussion

4.1 Influence of B content on structure evolution

The Al/Cr ratio is an important factor determining phase composition, film structure, mechanical and thermal properties of $Al_xCr_{1-x}N$ films [2-4]. Kawate et al. found the transition in the crystal structure from the fcc NaCl-like to the wurtzite type to occur in the range of x = 0.6 to 0.7 (corresponding to Al/Cr ratios of 1.5 - 2.3, depending on deposition conditions) [1]. It is well-established that film hardness and thermal stability of Al-Cr-N films get most improved when the Al/Cr ratio is close to this transition composition [3, 31]. Thus, the Al-Cr-B-N films investigated within this study were deposited from targets with an Al/Cr ratio of ~1.8 (i.e., x ~ 0.5 in the coating) to ensure the development of the fcc crystal structure. Since the solubility limit of Al in the CrN lattice is not reached for this composition, the film structure is characterized by the metastable supersaturated fcc-$Al_xCr_{1-x}N$ solid solution [3]. B added to this solid solution can be incorporated in its lattice either by substitution of Al and/or Cr atoms or by occupying interstitial sites. In the first case, the lattice parameter of the Al-Cr-(B)-N phase should decrease due to the smaller size of B incorporated instead of the larger Al and Cr atoms. This is reflected by the shift of the XRD peaks towards higher 2θ angles with increasing B content, as shown in Fig. 2. Since the solubility of B in the fcc-$Al_xCr_{1-x}N$ phase should be rather limited similar to TiN, and thus, if exceeding a critical concentration, B should segregate to grain boundaries where it forms with N an a-BN_x phase [11, 32, 33]. XPS measurements revealed the presence of B-N bonds in the Al-Cr-B-N films (Fig. 5(a)), which suggests that the sufficiently high N concentration (~50 at.%, see Table 1) promotes bonding of B with N (i.e., the B-B bonding configuration is rather unlikely) [34]. The BN_x phase has an only short-range ordered amorphous-like structure, as observed in other nanocomposite films consisting of transition metal nitrides and BN [35]. Its presence at the grain boundaries significantly affects the development of the film structure, as it interrupts growth of individual Al-Cr-(B)-N crystallites and causes renucleation during deposition [6, 32]. Thus, a fine-grained nanocomposite structure consisting of nanocrystalline Al-Cr-(B)-N grains surrounded by an a-BN_x matrix develops [10, 16]. There, incorporation of a low amount of B atoms in the fcc-$Al_xCr_{1-x}N$ solid solution can not be excluded. The limited growth of Al-Cr-(B)-N grains is reflected by the

development of their grain size, which is the smaller the higher the a-BN_x volume fraction is (see Figs. 3 and 6) [36]. The formation of such a nanocomposite structure consisting of binary nitrides such as fcc MeN and a-BN_x is energetically driven by the reduction of the total free energy of the system and thus requires much lower formation energy then it is needed for complex ternary or quaternary compounds [10].

Al-Cr-B-N films synthesized under high ion energy conditions (i.e., a bias voltage of -100 V) exhibit a very dense structure consisting of even smaller grains with respect to films prepared at -40 V (Figs. 1 and 3). This is associated with the effectively increased adatom mobility at the film surface induced by high-energetic incident particles, which may also be implanted in the subsurface region of the growing film [22, 37]. These processes subsequently affect growth mechanisms associated with enhanced nucleation and defect generation, which typically result in decreased crystallite size and hindered formation of a columnar structure, as it is seen in Figs. 1 and 3 [6, 22]. Moreover, deposition in pure N_2 atmosphere at relatively high total pressure (3.5 Pa) and higher ion energy promotes collisional dissociation of N_2^+ molecules at the film surface [37] and thus formation of the a-BN_x phase. The presence of B in the Al-Cr-N lattice and a-BN_x at the grain boundaries subsequently affects the orientation and size of Al-Cr-(B)-N crystallites (Fig. 2) [12].

4.2 Effect of B addition on the stress state and hardness

Changes in the microstructure and phase composition of the Al-Cr-(B)-N films are strongly associated with variations of their stress state and hardness. This is on the one hand driven by changes in the Al-Cr-N lattice structure due to incorporation of B and on the other hand by the formation of the nanocomposite structure.

In general, a low amount of alloying elements incorporated into the lattice by substitution of atoms or by occupying interstitial sites causes local stress fields which typically results in overall residual stress, e.g. compressive stress if larger atoms substitute smaller ones or if interstitials are incorporated in the lattice. This is demonstrated by the increase of the compressive stress for increasing Al/Cr ratios (see Fig. 7(a)). However, when Al is incorporated in the CrN lattice by substituting Cr atoms, the lattice parameter and, hence, compressive stress are expected to be

reduced. On the other hand, defect generation by ion bombardment is much easier in the open structure of an $Al_xCr_{1-x}N$ lattice with a higher number of smaller Al atoms, which subsequently contributes to development of compressive stress. The extent to which compressive stress develops in Al-Cr-N films thus significantly depends on the interplay of these stress inducing mechanisms. Since the strained lattice acts as an effective barrier for dislocation movement, caused by the formed local stress fields of the incorporated atoms interacting with those of the dislocations, the hardness is effectively increased with increasing compressive stress in the film (see Fig. 8).

The observed significant improvement of mechanical properties of Al-Cr-N films by B addition is, on the other hand, ascribed to a combined effect of solid solution hardening, grain size refinement (Hall-Petch hardening) and formation of an a-BN_x tissue phase embedding the Al-Cr-(B)-N crystallites [14, 15]. This explains why the hardness of Al-Cr-B-N films increases significantly by addition of B although the compressive residual stress is reduced (see Fig. 7(a)).

If only a small amount of B is added to Al-Cr-N, it can be assumed that a significant fraction is dissolved in the AlCrN lattice and, thus, solid solution hardening plays an essential role in hardness enhancement. The increase of hardness by addition of B above its solubility limit in the AlCrN lattice is, on the other hand, accompanied by a reduction of the compressive stress, which is related to the small crystallite size and the presence of a-BN_x at the grain boundaries. B and most probably also an a-BN_x phase improve mechanical properties, as they enhance the cohesion of grain boundaries by affecting the local bonding at the interface [32]. Once B segregates to the grain boundaries, the enhanced cohesive energy of interfacial areas in Al-Cr-B-N films results in increased hardness with respect to B-free Al-Cr-N films, even at low B contents (Fig. 8). The interfacial area strengthened by forming an a-BN_x phase results in formation of a nanocomposite structure, where Al-Cr-B-N crystallites are covered by an a-BN_x phase. Although the compressive stress of Al-Cr-B-N films with B content $\geq$2.3 at.% is significantly reduced by 0.4 - 1 GPa (for Al/Cr ratios of 1.5 or 2.3, respectively, see Fig. 7(a)), the hardness increases from 30 to 42 GPa. This is related to a significant decrease of the grain size and subsequent Hall-Petch hardening. This effect is, however, dominating only when the grains are completely covered by the a-BN_x tissue. While the grains are only partially covered (for the films with 2.3 at.% B, see Table 1), growth of the

Al-Cr-(B)-N crystallites (though rather limited) is still likely and the Hall-Petch hardening is thus not the major contribution to the enhanced hardness, but its combination with the solid solution hardening described above [11].

The formation of the nanocomposite structure with fully covered crystallites, which size is below 20 nm at higher B content (≥5.7 at.%), ensures high hardness of the films despite the significant reduction of the residual compressive stress (see Fig. 7(a)). The increased volume fraction of the a-BN_x phase in the Al-Cr-B-N films with 5.7 at.% B results in a complete encapsulation of the Al-Cr-(B)-N crystallites (Fig. 6) and causes pronounced grain size refinement accompanied with reduced boundary mobility. As a consequence, the generation and propagation of dislocations in the film is effectively hindered. In the case of 5.7 at.% B in the films, hardness is not further affected by the increased B content and remains constantly high.

At higher B content (9.1 at.%), a reduction of hardness is observed (Fig. 8). This is ascribed to increased thickness of the a-BN_x tissue, exceeding a certain limit and causing softening of the Al-Cr-B-N film. Moreover, the high fraction of a-BN_x reduces the size of randomly oriented crystallites below a critical limit, resulting in a dislocation annihilation process at the grain boundaries and break-down of the Hall-Petch relation (see the structure and grain size evolution in Figs. 2 and 3) [38]. In addition, intergranular sliding becomes important under loading as the number of interfacial atoms is increased. This reflects the dependence of the hardening mechanisms on the volume fraction of the a-BN_x phase, which change from dominating solid solution at lower to nanocomposite hardening at higher B contents.

The mechanical properties of thin films are also typically affected by the high energetic incident ions, which induce formation of interstitials and vacancies. Generation of high defect density gives subsequently rise to high residual compressive stress in the films, which typically positively influence their hardness [6]. B-free Al-Cr-N films show increased compressive stress with increasing substrate bias voltage [39]. As mentioned above, this common dependence is attributed to the formation of defects, which cause local stress fields during film growth [40]. Al-Cr-B-N films with low B-content (2.3 at.%) exposed to higher ion bombardment (-100 V bias) during growth reveal a hardness increase of 2 GPa from 41 to 43 GPa compared to those deposited at moderate incident energy (-40 V bias, see Fig. 8). This hardness improvement is ascribed predominantly to the generation of a high number of

defects, but also to the Hall-Petch hardening associated with a reduction of the crystallite size under intense ion bombardment (Fig. 3). The Al-Cr-B-N films with higher B content (>2.3 at.%) show almost no change in hardness by increasing the substrate bias voltage from -40 to -100 V (Fig. 8). This is because the higher B content, and thus an increased a-BN_x phase fraction, promotes relaxation of the compressive stress induced by the incident particles. Since ion-induced defects effectively annihilate within the a-BN_x tissue, this stress relaxation process is the more effective the thicker the a-BN_x tissue is. As a too high defect concentration at the grain boundaries causes weakening of these interfacial areas in the case of a polycrystalline structure (cracks can more easily propagate along weak boundaries under an applied load) [40], the presence of a defect-releasing and interface-strengthening a-BN_x tissue phase effectively contributes to the enhancement of mechanical properties of the Al-Cr-B-N films.

5 Conclusions

Al-Cr-B-N hard films were successfully synthesized by means of reactive cathodic arc evaporation using powder-metallurgical targets and characterized with respect to their composition, microstructure and mechanical properties. The Al-Cr-B-N films investigated in this study form either a polycrystalline or a nanocomposite structure consisting of face-centered cubic Al-Cr-(B)-N grains embedded in an amorphous BN_x tissue phase depending on the B content. The volume fraction of the BN_x phase increases with increasing B content, which is accompanied by a reduction of grain size of the cubic Al-Cr-(B)-N phase. The enhanced hardness of Al-Cr-B-N films with respect to B-free Al-Cr-N films is given by a combination of solid solution, Hall-Petch and nanocomposite hardening, accompanied by a significant reduction of residual compressive stress.

In summary, it has been demonstrated, that the addition of B to Al-Cr-N films has an outstanding beneficial effect on their mechanical properties, which makes them promising candidates as wear-protective coatings for cutting applications.

Acknowledgements

The authors are grateful to Alexander Fian (Institute of Nanostructured Materials and Photonics, JOANNEUM RESEARCH, Weiz, Austria) for performing XPS measurements and Christina Scheu (Department of Chemistry and Biochemistry, LMU Munich, Germany) for TEM investigations. Additionally, the authors would like to thank the Forschungszentrum Dresden-Rossendorf for providing ERDA measurements. Financial support of the Christian Doppler Society is highly acknowledged.

References

[1] M. Kawate, A. Kimura, T. Suzuki, J. Vac. Sci. Technol. A 20 (2) (2002) 569.

[2] R. Franz, B. Sartory, R. Kaindl, R. Tessadri, A. Reiter, V.H. Derflinger, P. Polcik, C. Mitterer, in G. Kneringer, P. Rödhammer, H. Wildner, eds., Proc. 16th Int. Plansee Seminar, Plansee, Reutte (A), Vol. 2, 2005, p. 932 (2005).

[3] A.E. Reiter, V.H. Derflinger, B. Hanselmann, T. Bachmann, B. Sartory, Surf. Coat. Technol. 200 (2005) 2114.

[4] Y. Makino, K. Nogi, Surf. Coat. Technol. 98 (1998) 1008.

[5] A. Sugishima, H. Kajioka, Y. Makino, Surf. Coat. Technol. 97 (1997) 590.

[6] I. Petrov, P.B. Barna, L. Hultman, J.E. Greene, J. Vac. Sci. Technol. A 21 (5) (2003) 117.

[7] R. Daniel, K.J. Martinschitz, J. Keckes, C. Mitterer, Acta Mater. 58 (2010) 2621.

[8] J. Musil, Surf. Coat. Technol. 125 (2000) 322.

[9] S. Vepřek, M.G.J. Vepřek-Heijman, P. Karvankova, J. Prochazka, Thin Solid Films 476 (2005) 1.

[10] S. Vepřek, Thin Solid Films 317 (1998) 449.

[11] J. Patscheider, T. Zehnder, M. Diserens, Surf. Coat. Technol. 146-147 (2001) 201.

[12] C. Tritremmel, R. Daniel, M. Lechthaler, P. Polcik, C. Mitterer, Thin Solid Films, submitted for publication.

[13] J.L. Endrino, G.S. Fox-Rabinovich, A. Reiter, S.V. Veldhuis, R.E. Galindo, J.M. Albella, J.F. Marco, Surf. Coat. Technol. 201 (2007) 4505.

[14] T. Sato, T. Yamamoto, H. Hasegawa, T. Suzuki, Surf. Coat. Technol. 201 (2006) 1348.

[15] M. Nose, T. Kawabata, T. Watanuki, S. Ueda, K. Fujii, K. Matsuda, S. Ikeno, Surf. Coat. Technol. 205 (2011) 533.

[16] M.A. Baker, S. Klose, C. Rebholz, A. Leyland, A. Matthews, Surf. Coat. Technol. 151-152 (2002) 338.

[17] T.H.D. Keijser, J.I. Langford, E.J. Mittemeijer, A.B.P. Vogels, J. Appl. Cryst. 15 (1982) 308.

[18] Unifit Software, http://uni-leipzig.de/~unifit/, 09/2012.

[19] P.H. Mayrhofer, C. Mitterer, Surf. Coat. Technol. 133-134 (2000) 131.

[20] R. Daniel, D. Holec, M. Bartosik, J. Keckes, C. Mitterer, Acta Mater. 59 (2011) 6631.

[21] W.C. Oliver, G.M. Pharr, J. Mater. Res. 7 (1992) 1564.

[22] R.L. Boxman, P.J. Martin, D.M. Sanders, Handbook of Vacuum Arc Science and Technology: Fundamentals and Applications, Noyes Publications, New Jersey, 1995.

[23] A. Anders, Cathodic Arcs, 1 ed., Springer, New York, 2008.

[24] J. Neidhardt, M. O'Sullivan, A.E. Reiter, W. Rechberger, W. Grogger, C. Mitterer, Surf. Coat. Technol. 201 (2006) 2553.

[25] Powder Diffraction File (Card 00-025-1495 for fcc-AlN, Card 00-011-0065 for fcc-CrN), International Center for Powder Diffraction Data, ICDD, PDF-2/Release 2007, 2007.

[26] R. Kaindl, R. Franz, J. Soldán, A. Reiter, P. Polcik, C. Mitterer, B. Sartory, R. Tessadri, M. O'Sullivan, Thin Solid Films 515 (2006) 2197.

[27] Binding energies for relevant bonds obtained from the La Surface XPS database, http://www.lasurface.com/database/elementxps.php, 09/2012.

[28] E.C. Onyiriuka, Appl. Spectrosc. 47 (1993) 35.

[29] D. Briggs, M.P. Seah, Practical surface analysis, 2nd ed., John WILEY & SONS, 1993.

[30] A. Fernandez, C. Real, J.C. Sanchez-Lopez, M.D. Alcala, Nanostruct. Mater. 11 (2) (1999) 249.

[31] H. Willmann, P.H. Mayrhofer, P.O.Å. Persson, A.E. Reiter, L. Hultman, C. Mitterer, Scr. Mater. 54 (2006) 1847.

[32] P.H. Mayrhofer, C. Mitterer, L. Hultman, H. Clemens, Prog. Mater Sci. 51 (2006) 1032.

[33] J. Neidhardt, Z. Czigány, B. Sartory, R. Tessadri, M. O'Sullivan, C. Mitterer, Acta Mater. 54 (2006) 4193.

[34] C. Rebholz, J.M. Schneider, A.A. Voevodin, J. Steinebrunner, C. Charitidis, S. Logothetidis, A. Leyland, A. Matthews, Surf. Coat. Technol. 113 (1999) 126.

[35] K.P. Budna, P.H. Mayrhofer, J. Neidhardt, É. Hegedũs, I. Kovács, L. Tóth, B. Pécz, C. Mitterer, Surf. Coat. Technol. 202 (2008) 3088.

[36] C. Rebholz, M.A. Monclus, M.A. Baker, P.H. Mayrhofer, P.N. Gibson, A. Leyland, A. Matthews, Surf. Coat. Technol. 201 (2007) 6078.

[37] R. Daniel, K.J. Martinschitz, J. Keckes, C. Mitterer, J. Phys. D: Appl. Phys. 42 (7) (2009) 075401.

[38] E. Arzt, Acta Mater. 46 (1998) 5611.

[39] J. Soldán, J. Neidhardt, B. Sartory, R. Kaindl, R. Čerstvý, P.H. Mayrhofer, R. Tessadri, P. Polcik, M. Lechthaler, C. Mitterer, Surf. Coat. Technol. 202 (2008) 3555.

[40] J.-E. Sundgren, Thin Solid Films 128 (1985) 21.

11 Publication IV

Publication IV

Mechanical and tribological properties of Al-Ti-N/Al-Cr-B-N multilayer films synthesized by cathodic arc evaporation

C. Tritremmel, R. Daniel, H. Rudigier, P. Polcik, C. Mitterer

Submitted for publication

Mechanical and tribological properties of Al-Ti-N/Al-Cr-B-N multilayer films synthesized by cathodic arc evaporation

C. Tritremmel[1], R. Daniel[2], H. Rudigier[3], P. Polcik[4], C. Mitterer[1,2]

[1] Christian Doppler Laboratory for Advanced Hard Coatings at the Department of Physical Metallurgy and Materials Testing, Montanuniversität Leoben, Franz-Josef-Strasse 18, A-8700 Leoben, Austria
[2] Department of Physical Metallurgy and Materials Testing, Montanuniversität Leoben, Franz-Josef-Strasse 18, A-8700 Leoben, Austria
[3] OC Oerlikon Balzers AG, Iramali 18, LI-9496 Balzers, Liechtenstein
[4] PLANSEE Composite Materials GmbH, D-86963 Lechbruck, Germany

Abstract

Al-Ti-N/Al-Cr-B-N multilayer films were synthesized by means of cathodic arc evaporation. The influence of the individual layer thicknesses on mechanical and tribological properties was systematically investigated and compared with Al-Cr-B-N single layer films. Al-Cr-B targets with 10 and 20 at.% B, respectively, were used in combination with Al-Ti targets, having an Al/Ti ratio of 1. The multilayer films exhibit enhanced hardness and significantly reduced residual compressive stress together with improved wear resistance compared to Al-Cr-B-N single layer films.

Keywords: Al-Cr-N; Multilayer; Mechanical properties; Tribological properties

1 Introduction

Al-Ti-N and Al-Cr-N films are well-established coating systems extensively used for wear protection of cutting tools, dies and molds. This is attributed to their outstanding properties such as high hardness, wear resistance and good thermal stability [1-3]. Both ternary $Al_xTi_{1-x}N$ and $Al_xCr_{1-x}N$ crystallize in a single-phase face-centered cubic B1 (fcc) modification for AlN mole fractions *x* below ~0.7 (corresponding to Al/Cr and Al/Ti ratios of 1.5 - 2.3, depending on deposition conditions) or in a mixed or single-phase wurtzite B4 (w) modification for higher Al contents [2, 4]. The fcc modification exhibits, in contrast to wurtzite, superior mechanical and tribological properties and is thus favorable for many engineering applications. Despite successful application of these metastable ternary nitrides, the

demand on increased tool performance and life time fosters the continuous improvement of the coating systems. A possible approach to yield significant improvement of the film properties is the addition of alloying elements like Si or B. These elements are known to promote formation of a nanocomposite structure [5-7], which gives rise to growth of nanostructured materials with outstanding properties such as superhardness, toughness and/or increased wear resistance [8, 9]. Al-Cr-B-N films have recently been shown to exhibit superhardness and low compressive stress, originating from the nanocomposite structure where nano-sized fcc AlCrN grains are surrounded by a thin BN_x tissue phase [10]. Further improvement of such nanocomposite layers can be obtained by optimizing their design and architecture. When combined with other materials in a multilayer structure, their properties may distinctively be improved, and additionally adjusted by changing the thickness of the individual layers [11-13].

Consequently, the purpose of the present study was to investigate the microstructure, mechanical and tribological properties of cathodic arc evaporated Al-Ti-N/Al-Cr-B-N multilayer films with an individual Al-Cr-B-N layer thickness ranging from ~5 to ~180 nm.

2 Experimental details

The Al-Cr-B-N single layer and Al-Ti-N/Al-Cr-B-N multilayer films were synthesized by cathodic arc evaporation in an industrial scale deposition system (INNOVA, OC Oerlikon Balzers AG) using four arc sources equipped with powder-metallurgically prepared Al-Cr-B and $Al_{0.50}Ti_{0.50}$ targets (PLANSEE Composite Materials GmbH). The Al/Cr atomic ratio in the Al-Cr-B targets was kept constant at ~1.8, with B content varying between 10 and 20 at.%. The films were deposited on ultrasonically cleaned mirror-polished Si(100), cemented carbide cutting inserts (WC – 6 wt.% Co) and high-speed steel (DIN 1.3343, AISI M2) coupons (∅ 30 mm × 10 mm) mounted on the two-fold rotating substrate holder. The double-side polished Si strips (20 × 7 × 0.5 mm^3) were used for X-ray diffraction (XRD), transmission electron microscopy (TEM) and stress measurements. The coated cutting inserts were used for morphological investigations by scanning electron microscopy (SEM) and for hardness measurements. The high-speed steel coupons were used for tribological testing. The substrates were positioned on the substrate carrousel in the deposition

chamber (evacuated prior to deposition to a base pressure of 5×10^{-4} Pa or below), heated to 500 °C and etched in pure Ar plasma. During the whole deposition process, the substrate temperature was kept constant at 500 °C. The arc current was set to 150 and 200 A on each Al-Cr-B and $Al_{0.50}Ti_{0.50}$ target. The Al-Cr-B-N films were grown in pure nitrogen at 3.5 Pa on substrates biased to -100 V, while the substrate bias during deposition of the Al-Ti-N layers was held constant at -40 V. All multilayer films are combined with an Al-Ti-N base layer to obtain sufficient adhesion to the substrate. The substrate bias during deposition of the multilayer films denoted with “5 nm” and the transition layers (see Table 1), respectively, was held constant at -40 V. The total deposition time was adjusted in order to obtain a typical film thickness of 3 ± 0.3 µm.

XRD was used to investigate the crystallographic structure of the films. The diffractometer (D8 Advance, Bruker AXS) was equipped with parallel beam optics and an energy-dispersive detector (Sol-X). The XRD patterns were recorded using Cu Kα radiation operated at a voltage of 40 kV and a current of 40 mA. Elemental depth profile measurements of the Al-Ti-N/Al-Cr-B-N multilayer films were determined by means of elastic recoil detection analysis (ERDA) using a 35 MeV Cl^{7+} ion beam and a Bragg ionization detector. A detailed microstructural analysis of the multilayer films was conducted by TEM observations using a Philips CM 20 for Z-contrast investigations and a FEI Tecnai F20 for conventional and energy-filtered TEM (EFTEM, Gatan GIF Quantum energy filter) studies.

The residual macroscopic stresses in the films were measured using the substrate curvature method and calculated by the modified Stoney equation [14]. Hardness measurements were conducted by means of nanoindentation (UMIS, Fischer-Cripps Laboratories) using a Berkovich diamond tip and calculated from at least 30 load-displacement curves obtained during a test in the load range from 5 to 25 mN [15].

Tribological tests were conducted using a ball-on-disk tribometer (CSM Instruments) in ambient air at room temperature (RT, ~25 °C), 500 and 700 °C. Sintered alumina balls with a diameter of 6 mm were used as a counterpart. The sliding speed was set to 10 cm/s and the radius of the wear track to 7 mm. The normal load during the tests at RT was kept constant at 10 N and the sliding distance was 1000 m. At elevated temperatures (500, 700 °C), the normal load was reduced

to 5 N and the sliding distance to 300 m. The wear tracks were analyzed using an optical 3D white light profiling system (Wyko NT 1000) providing cross-sections of the wear tracks and the worn volume necessary for calculation of the wear coefficient (ratio between wear volume and normal load times sliding distance) [16]. By using a Jobin-Yvon Labram confocal-Raman spectrometer equipped with a frequency-doubled Nd-YAG laser (532.2 nm, 100mW), the changes in the surface structure of the wear tracks after tribological testing at different temperatures were analyzed.

3 Results

All deposited films are well adherent to the different substrate materials. Beside the Al-Cr-B-N single layer films (labeled as “3.0 µm” in the subsequent figures), a set of multilayer films was synthesized. The denotation and the architecture of the individual multilayer films are described in Table 1.

Table 1: Denotation and architecture of the multilayer films. “Iterations” refers to the number iterations of the Al-Ti-N sub layer, Al-Cr-B-N + Al-Ti-N transition layer and Al-Cr-B-N sub layer sequence. The transition layer is characterized by simultaneously running Al-Cr-B and Al-Ti targets resulting in a layer thickness of ~35 nm.

Multilayer denotation	**Top**	**180**	**90**	**5**
		Layer thickness [nm]		
Al-Cr-B-N top layer	~700	~180	~90	~5
Al-Cr-B-N sub layer	~180	~180	~90	~5
Al-Cr-B-N + Al-Ti-N transition layer	~35	~35	~35	none
Al-Ti-N sub layer	~60	~60	~30	~5
Iterations	8	8	14	simultaneous deposition
Al-Ti-N base layer	~200	~200	~200	~200

3.1 Microstructure

Single layer coatings deposited from $Al_{0.58}Cr_{0.32}B_{0.10}$ and $Al_{0.52}Cr_{0.28}B_{0.20}$ cathodes possess an Al content of 26.7 and 22.9 at.%, a Cr content of 21.7 and 22.6 at.% and the B concentration was found to be 2.3 and 5.7 at.%, respectively. The Al-Cr-B-N films reveal a nearly stoichiometric composition (i.e., $\frac{N}{Al+Cr+B} \approx 1$). The loss of Al (~5 at.%) in the Al-Cr-B-N films with respect to the target composition is most likely associated with gas scatter effects during the particle transport from the target to the substrate surface [17]. The scattering effect is even more pronounced for B showing a loss of nearly 50 % with respect to the target composition. More details about the conducted ERDA measurements can be found in [10]. As already reported earlier [10], the Al-Cr-B-N single layer films (“3.0 μm”) consist of a fcc crystalline Al-Cr-N phase irrespective of the B content. Small amounts of B can be incorporated in the Al-Cr-N lattice either by substitution of Al and/or Cr atoms or by occupying interstitial sites. The additional formation of an amorphous BN_x phase has been revealed by a combination of X-ray photoelectron spectroscopy and TEM [10]. The Al-Ti-N layers possess a stoichiometric composition and reveal a minor increase of the Ti/Al metal ratio with respect to the target composition [18]. Note that the notation of the films throughout the paper corresponds exclusively to the target composition.

Diffraction patterns of the Al-Cr-B-N single and Al-Ti-N/Al-Cr-B-N multilayer films are shown in Fig. 1. The diffraction peaks of the fcc phase are situated between fcc-AlN and fcc-CrN [19], which reflects the formation of a metastable solid solution where Cr is substituted by Al in the CrN lattice. The Al-Cr-B-N single layer films grow predominantly with (111) preferred orientation exhibiting additionally low-intensity peaks corresponding to (100)- and (110)-oriented grains (see Figs. 1(a) and (b)). Although the individual Al-Cr-(B)-N and Al-Ti-N phases in the Al-Ti-N/Al-Cr-B-N multilayer films could not be resolved, it is evident that the texture of the multilayer films changes continuously from (111) to (100) with decreasing Al-Cr-B-N layer thickness. The growth of the “5 nm” multilayer film is significantly affected by the high number of interfaces and develops with randomly oriented grains. The increased B content in the Al-Cr-B-N films does not affect the film texture; however, it gives rise to

a reduction of the film crystallinity, as indicated by the increasing peak broadening and reduced peak intensity (see Fig. 1(b)).

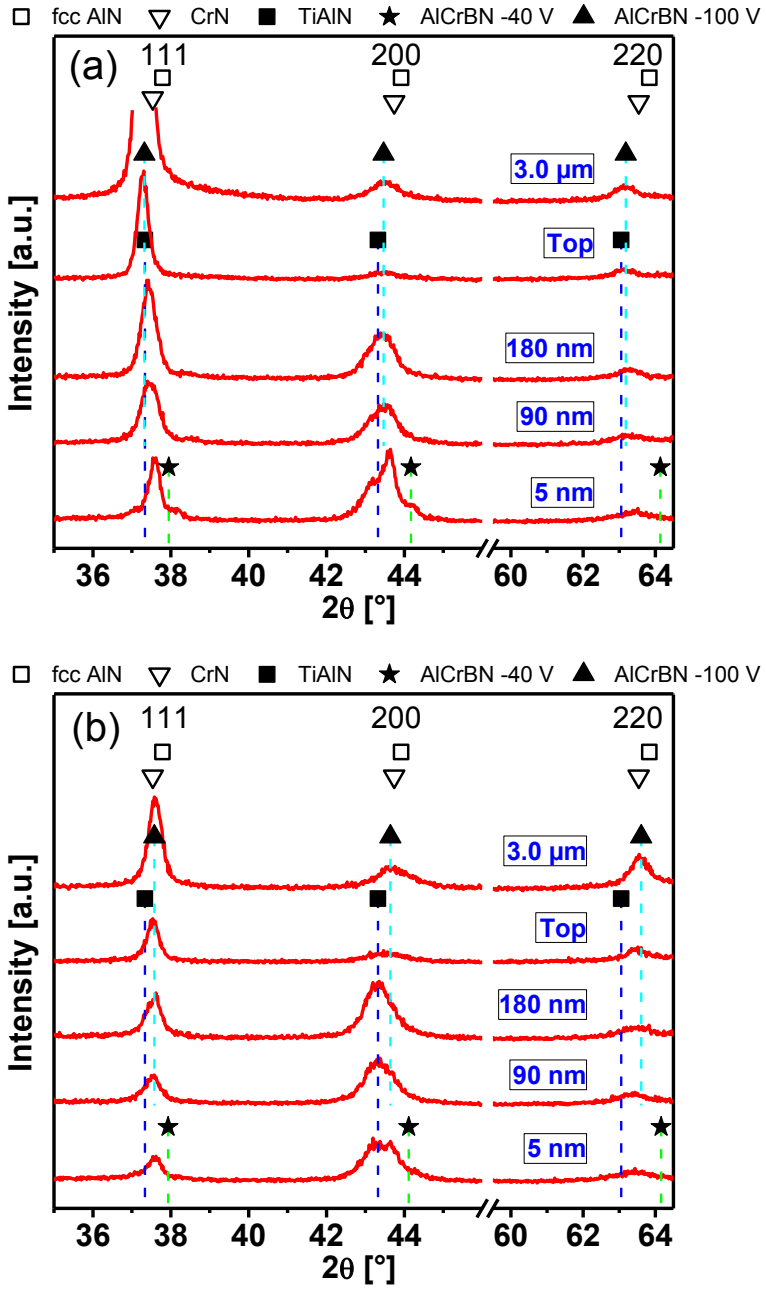

Figure 1: XRD patterns of (a) $Al_{0.50}Ti_{0.50}N/Al_{0.58}Cr_{0.32}B_{0.10}N$ and (b) $Al_{0.50}Ti_{0.50}N/Al_{0.52}Cr_{0.28}B_{0.20}N$ multilayer films for different Al-Cr-B-N layer thicknesses. The individual multilayers are denoted as “Top”, “180 nm”, “90 nm” and “5 nm”. This notation describes the Al-Cr-B-N layer thickness in the multilayer films (see Table 1).

A SEM micrograph of the fracture cross-section of the $Al_{0.50}Ti_{0.50}N/Al_{0.52}Cr_{0.28}B_{0.20}N$ multilayer film (“Top”) is shown in Fig. 2. The macroscopic characteristics are a rather featureless morphology and a comparatively smooth surface for an arc evaporated film.

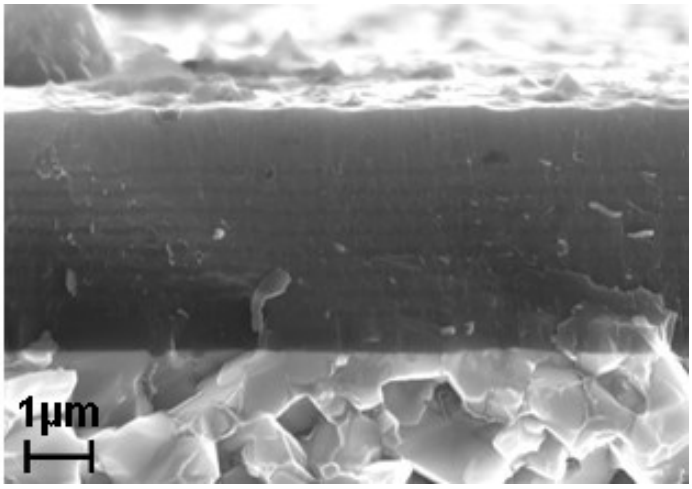

Figure 2: SEM cross-sectional micrograph of an $Al_{0.50}Ti_{0.50}N/Al_{0.52}Cr_{0.28}B_{0.20}N$ multilayer film with a 0.8 µm-thick $Al_{0.52}Cr_{0.28}B_{0.20}N$ top layer (“Top”), deposited on cemented carbide substrate.

The cross-sectional TEM micrograph of the $Al_{0.50}Ti_{0.50}N/Al_{0.52}Cr_{0.28}B_{0.20}N$ multilayer film (“90 nm”) shows in detail the sequence of the individual layers by means of mass contrast (Fig. 3(a)). The transition from Al-Cr-B-N to Al-Ti-N layer and vice versa is not abrupt; these layers are separated by a thin transition layer of ~35 nm thickness, which was achieved by simultaneous deposition from both sets of $Al_{0.52}Cr_{0.28}B_{0.20}$ and $Al_{0.50}Ti_{0.50}$ targets. The cross-sectional high-resolution EFTEM image in Fig. 3(b) shows the transition layer to consist of several thin (5 – 10 nm) Al-Cr-B-N and Al-Ti-N layers which is a result of the two-fold rotation of the substrate holder during deposition. ERDA elemental depth profile analysis of the $Al_{0.50}Ti_{0.50}N/Al_{0.52}Cr_{0.28}B_{0.20}N$ multilayer film (“90 nm”) revealed alternating Cr, Ti and B concentrations for the transition layer and constant N and Al content across the individual layers (Fig. 3(c)). It is also evident that the growth of individual columns (column width of ~20 nm) is not interrupted at the Al-Cr-B-N/Al-Ti-N interfaces (Fig. 3(b)).

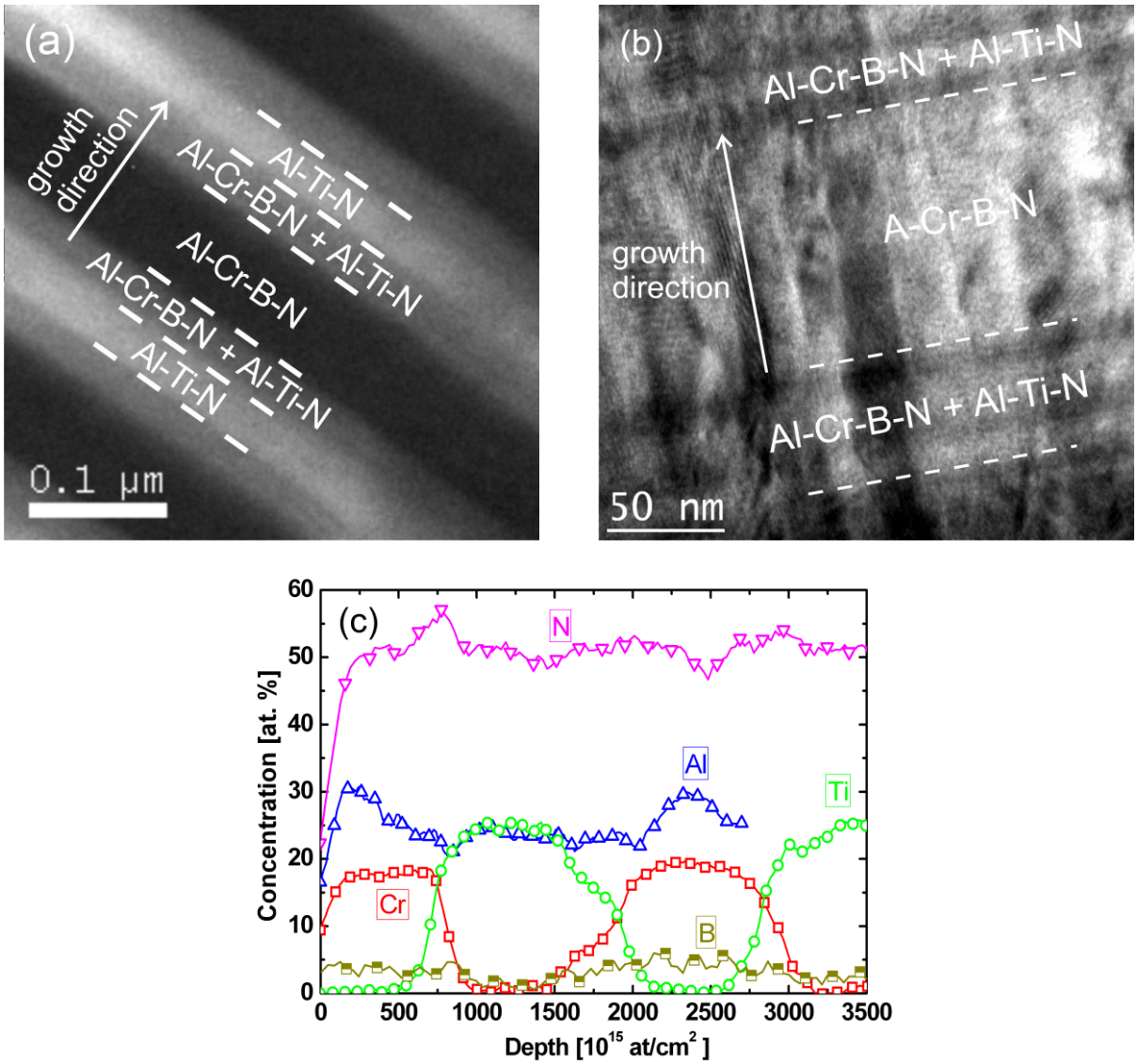

Figure 3: (a) Cross-sectional TEM micrograph (Z-contrast), (b) high resolution EFTEM micrograph and (c) ERDA depth profile analysis of the $Al_{0.50}Ti_{0.50}N/Al_{0.52}Cr_{0.28}B_{0.20}N$ multilayer film with the $Al_{0.52}Cr_{0.28}B_{0.20}N$ layer having a thickness of 90 nm ("90 nm") deposited on Si(100) substrate.

3.2 Mechanical and tribological properties

The indentation hardness and Young's modulus of the as-deposited Al-Cr-B-N single layer and Al-Cr-B-N/Al-Ti-N multilayer films as a function of the Al-Cr-B-N layer thickness are displayed in Fig. 4. The multilayer films exhibit hardness values ranging from 44 to 50 GPa, which is significantly higher than that of the Al-Cr-B-N single layer films (41-43 GPa). In general, the films with lower B content (10 at.%) revealed higher hardness than Al-Cr-B-N single layer films with higher B-content [10];

however, the maximum in hardness was obtained for the $Al_{0.50}Ti_{0.50}N/Al_{0.52}Cr_{0.28}B_{0.20}N$ multilayer film ("Top"). The Young's modulus decreases, similarly to hardness, from 615 to 550 GPa with increasing B content (see Fig. 4). Unlike hardness, decreasing Al-Cr-B-N sublayer thickness results in lower Young's modulus, except for $Al_{0.50}Ti_{0.50}N/Al_{0.58}Cr_{0.32}B_{0.10}N$ ("5 nm").

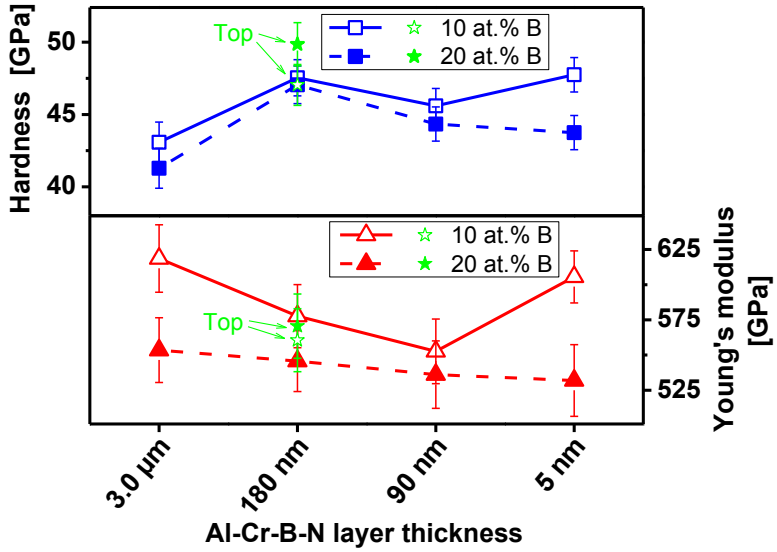

Figure 4: Hardness and Young's modulus of the Al-Cr-B-N single ("3.0 µm") and Al-Ti-N/Al-Cr-B-N multilayer films as a function of the Al-Cr-B-N layer thickness (for denotation see Table 1).

The average residual stress (σ_{tot}) of the Al-Cr-B-N single layer and Al-Ti-N/Al-Cr-B-N multilayer films as a function of B content and Al-Cr-B-N layer thickness is plotted in Fig. 5. All films investigated are in the compressive stress state with values ranging from -0.3 to -1.6 GPa. The compressive stress is predominantly a result of the high-energy ion irradiation of the growing film, which causes formation of structural defects [20]. The highest compressive stress is observed for the Al-Cr-B-N single layer film ("3.0 µm") and decreases with increasing B content. However, the residual stress is dramatically reduced in the Al-Ti-N/Al-Cr-B-N multilayer films, ranging from -0.3 to -0.8 GPa. The stress reduction gets more pronounced with increasing B content and decreasing thickness of Al-Cr-B-N sublayers (see Fig. 5).

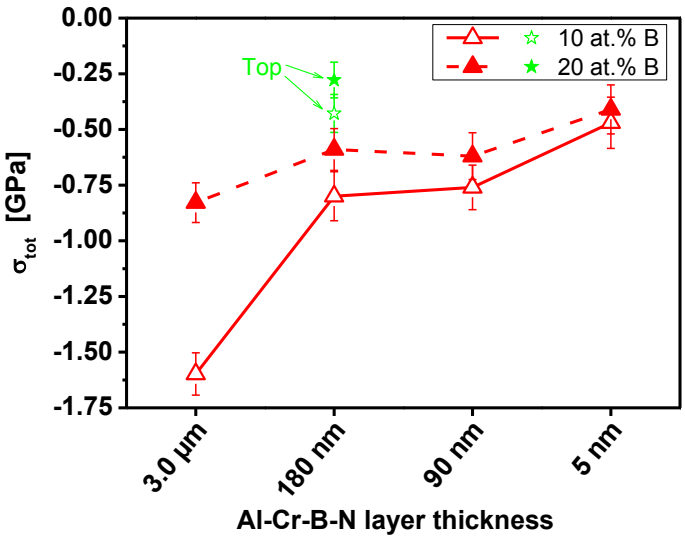

Figure 5: Development of the total residual stress (σ_{tot}) of the Al-Cr-B-N single ("3.0 µm") and Al-Ti-N/Al-Cr-B-N multilayer films as a function of the Al-Cr-B-N layer thickness (for denotation see Table 1).

The effect of the elemental composition and the multilayer architecture on friction and wear behavior of the B-containing Al-Cr-N films was examined by means of tribological testing. Fig. 6 shows the mean coefficient of friction (COF) for Al-Cr-B-N single layer and Al-Ti-N/Al-Cr-B-N multilayer films, sliding against alumina balls in ambient air at different temperatures. At RT, the mean COF for all films lies in the range from 0.6 to 0.7. The highest value corresponds to the Al-Cr-B-N single layer films ("3.0 µm"). As temperature is increased to 500 °C, the COF increases to a value of ~0.9. In this case, the single layer films ("3.0 µm") exhibit lower COF (~0.7) in comparison to the multilayer films. Ball-on-disk tests performed at 700 °C showed a mean friction coefficient of ~0.6 for both, single- and multilayer films.

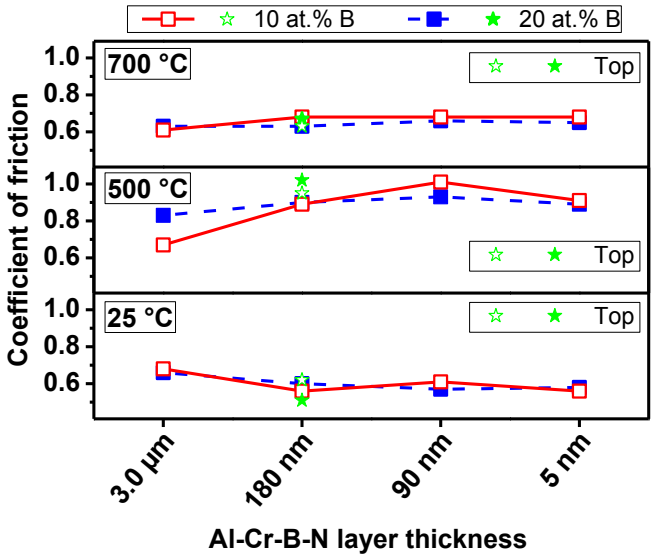

Figure 6: Mean friction coefficient of the Al-Cr-B-N single ("3.0 µm") and Al-Ti-N/Al-Cr-B-N multilayer films at room temperature (25 °C), 500 and 700 °C (for denotation see Table 1).

Two-dimensional surface profiles of the wear tracks after tribological testing at RT, 500 and 700 °C are shown in Fig. 7 for $Al_{0.58}Cr_{0.32}B_{0.10}N$ single layer and $Al_{0.50}Ti_{0.50}N/Al_{0.58}Cr_{0.32}B_{0.10}N$ multilayer films ("Top"). In addition, insets show optical light microscopy images of the wear scar at the alumina counterpart. In the case of $Al_{0.58}Cr_{0.32}B_{0.10}N$ single layer films, only minor wear is visible after testing at RT, while the wear scar on the counterpart is clearly evident (Fig. 7(a)). An increase in the testing temperature to 500 and 700 °C is accompanied with increased abrasive wear resulting in a wear track depth of 0.8 and 1.5 µm, respectively. This is less than the film thickness, giving evidence that the $Al_{0.58}Cr_{0.32}B_{0.10}N$ films did not fail. In the case of the $Al_{0.50}Ti_{0.50}N/Al_{0.58}Cr_{0.32}B_{0.10}N$ multilayer films ("Top"), no significant material removal is evident after testing at RT and 500 °C (Fig. 7(b)). A further increase in temperature to 700 °C results in a distinct increase in wear with a maximum wear depth of ~1 µm. Moreover, a considerable material accumulation at the borders of the wear track is observed. In comparison to the Al-Cr-B-N single layer films (Fig. 7(a)), the abrasive wear of the multilayer films is significantly reduced (Fig. 7(b)), especially at a temperature of 500 °C. The wear resistance of the films represented by the wear coefficients is summarized in Table 2.

Table 2: Wear coefficients of the $Al_{0.58}Cr_{0.32}B_{0.10}N$ single layer films ("3.0 µm") and $Al_{0.50}Ti_{0.50}N/Al_{0.58}Cr_{0.32}B_{0.10}N$ multilayer films ("Top") after testing at 25, 500 and 700 °C against alumina balls.

Film	Wear coefficient [m^3/Nm]		
	25 °C	500 °C	700 °C
Single layer	$5.6x10^{-17}$	$4.1x10^{-15}$	$3.4x10^{-15}$
Multilayer	$4.9x10^{-17}$	$4.7x10^{-16}$	$2.3x10^{-15}$

The wear coefficient increases with increasing temperature for both single layer and multilayer films. At 500 °C, the wear of the $Al_{0.50}Ti_{0.50}N/Al_{0.58}Cr_{0.32}B_{0.10}N$ multilayer is an order of magnitude lower as compared to the $Al_{0.58}Cr_{0.32}B_{0.10}N$ single layer film. Also tribological testing at 700 °C reveals higher wear of the single layer films. Nevertheless, also Al-Cr-B-N single layer films exhibit significantly lower wear than commercially used B-free Al-Cr-N films [3].

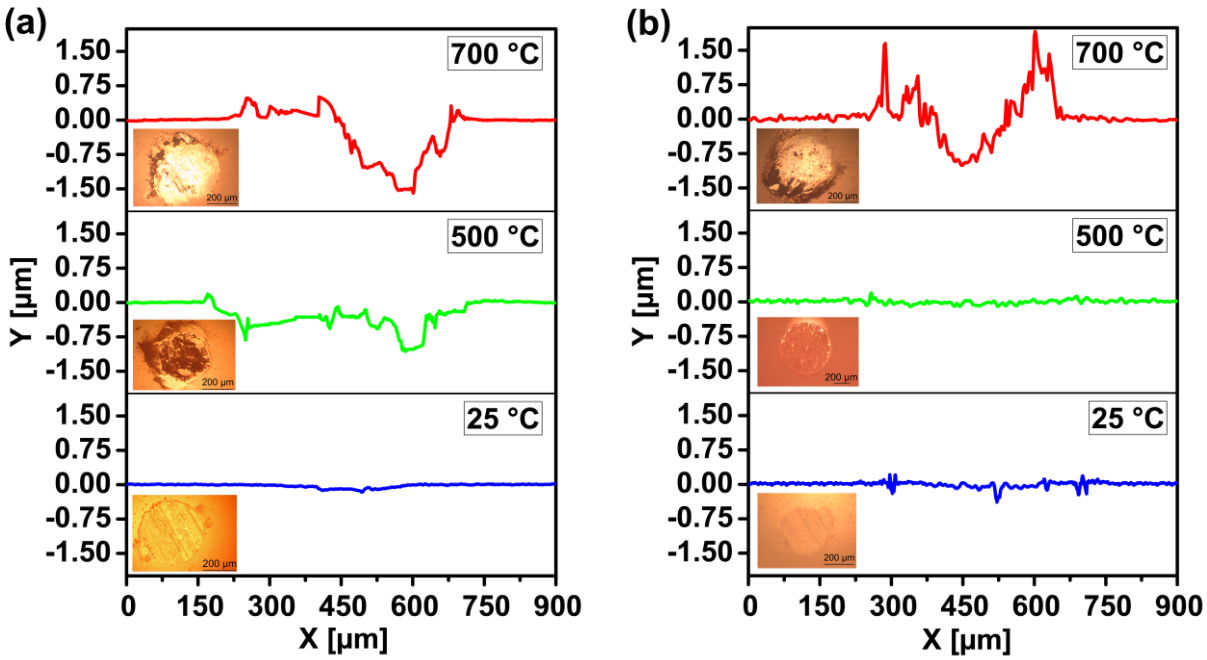

Figure 7: Two-dimensional profiles of the wear tracks after ball-on-disk tests against alumina at 25, 500 and 700 °C of (a) $Al_{0.58}Cr_{0.32}B_{0.10}N$ single ("3.0 µm") and (b) $Al_{0.50}Ti_{0.50}N/Al_{0.58}Cr_{0.32}B_{0.10}N$ multilayer films ("Top", for denotation see Table 1).

Subsequent to the ball-on-disk tests, the individual wear tracks and surrounding areas were analyzed by Raman spectroscopy to investigate possible changes of the film material after exposure to high temperatures in the contact with the counterpart (see Fig. 8). Compared to the pristine coating surface, the wear tracks on $Al_{0.58}Cr_{0.32}B_{0.10}N$ single layer films (Fig. 8(a)) reveals significant changes of the Raman spectra up to 500 °C. A further increase in test temperature to 700 °C results in a distinctive peak shift accompanied with the appearance of small peaks corresponding to iron oxides (i.e., Fe_2O_3 and Fe_3O_4). This implies that some regions in the wear track on the film are worn through, even though the wear track depth is smaller than the film thickness (see Fig. 7(a)). In the case of $Al_{0.50}Ti_{0.50}N/Al_{0.58}Cr_{0.32}B_{0.10}N$ multilayer films, the recorded Raman spectra of the individual wear tracks remain essentially unaffected, even after ball-on-disk tests conducted at 700 °C (Fig. 8(b)).

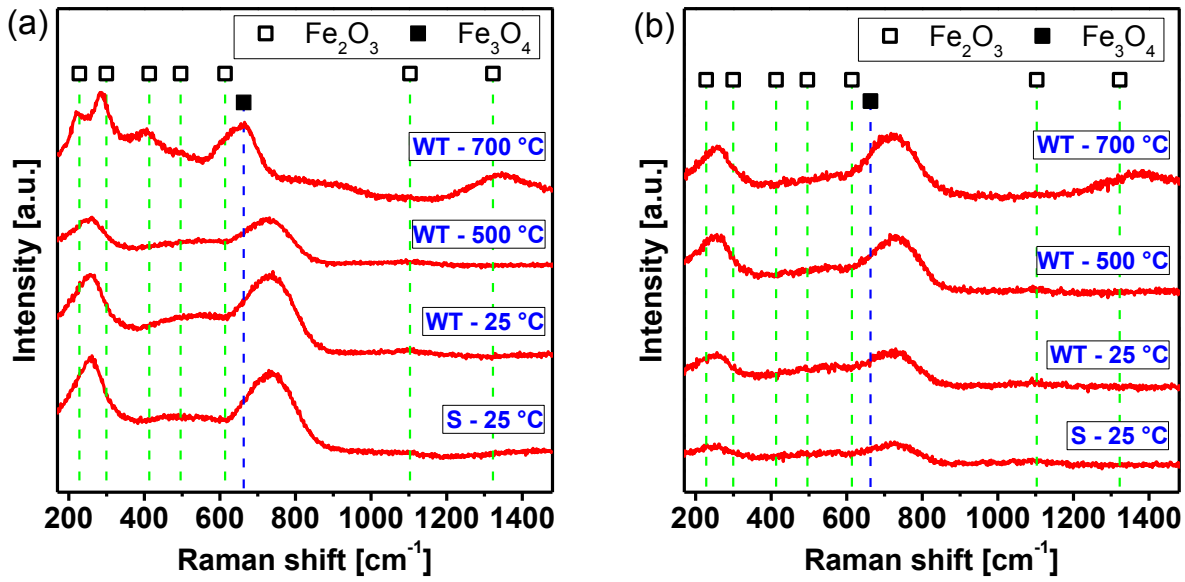

Figure 8: Raman spectra obtained after ball-on-disk testing at 25 , 500 and 700 °C of (a) $Al_{0.58}Cr_{0.32}B_{0.10}N$ single ("3.0 µm") and (b) $Al_{0.50}Ti_{0.50}N/Al_{0.58}Cr_{0.32}B_{0.10}N$ multilayer films ("Top", for denotation see Table 1). In addition, Raman spectra of the as-deposited films are shown. S: surface, WT: wear track.

4 Discussion

The dependency of the mechanical and tribological properties of Al-Cr-N coatings on the Al/Cr ratio is well established [2, 3]. Their hardness, oxidation resistance and thermal stability exhibit an optimum when the Al/Cr ratio is close to the transition zone yet with cubic structure [3, 21]. The Al-Cr-B-N films were synthesized from Al-Cr-B cathodes with an Al/Cr ratio of ~1.8, thus they show the fcc crystal structure as the solubility limit of Al in the CrN lattice is not reached (see Figs. 1(a) and (b)). As already established in an earlier publication [10], the addition of B results in formation of a nanocomposite structure consisting of fcc Al-Cr-(B)-N grains embedded in an amorphous BN_x tissue phase, where its thickness depends on the B content. A sufficiently high volume fraction of the amorphous BN_x phase leads to a complete encapsulation of the individual Al-Cr-(B)-N grains and hinder their further growth [6]. The reduction of the grain size is also accompanied by the loss of the (111) preferred orientation of the Al-Cr-(B)-N grains (see Figs. 1(a) and (b)).

In order to improve the adhesion of Al-Cr-B-N to the substrate, Al-Cr-B-N was grown on a well-established and adherent Al-Ti-N baselayer. The metastable $Al_{0.50}Ti_{0.50}N$ single layer films exhibit a single-phase fcc crystal structure and show a dense and columnar morphology [22]. The hardness and Young's modulus of the base layers, measured by nanoindentation, are ~30 and ~325 GPa, respectively, and correspond well to literature [23]. In contrast, Al-Cr-B-N single layer films exhibit significantly higher hardness and Young's modulus of 43 GPa and 625 GPa, respectively (see Fig. 4). These enhanced mechanical properties of Al-Cr-B-N have been attributed to a combined effect of a solid solution, Hall-Petch and nanocomposite hardening [10]. Solid solution hardening is caused by the substitution of Cr by Al atoms in the CrN lattice and the incorporation of B mainly on interstitial sites. Such alloying causes elastic strain fields due to the different size of incorporated and host atoms. The elastic strain fields subsequently hinder dislocation movement and thus remarkably increase hardness. Smaller grains, as evidenced by the increasing XRD peak broadening with raising B content (see Fig. 1), also lead to a hardness increase according to the Hall-Petch relation. A further contribution to hardness enhancement is the formation of a nanocomposite structure, where Al-Cr-(B)-N grains are surrounded by an amorphous BN_x tissue phase.

The combination of $Al_{0.50}Ti_{0.50}N$ and Al-Cr-B-N layers in a multilayer architecture results in a further improvement of the mechanical properties and enhanced wear resistance (see Figs. 4 and 7). The hardness of the multilayered films is consistently higher than that of the corresponding Al-Cr-B-N and Al-Ti-N single layer films and reaches values up to 50 GPa. The enhanced hardness of this multilayer arrangement with respect to the individual constituents is given by the reduction of the dislocation mobility at the interfaces between the individual layers [24]. This effect is the more pronounced the larger the difference in Young's modulus of the layers is, as demonstrated for the combination of Al-Cr-B-N (Young's modulus $\geq$ 550 GPa) and $Al_{0.50}Ti_{0.50}N$ (Young's modulus ~325 GPa). In addition, also the shear modulus and consequently the dislocation line energy of the alternating layers differ [25]. The disparity of the individual layers results in hindered dislocation movement through the interfaces. The resulting dislocation pile-up gives subsequently rise to strengthening of the material [24, 26].

The hardness of a multilayer material is also affected by the interface structure. The Al-Cr-B-N, Al-Ti-N and transition layers alternating in growth direction are all separated by well-defined and sharp interfaces (see Fig. 3(b)). There is no evidence from TEM investigations of porosity at the highly coherent interfaces between the individual layers, which is attributed to the effect of ion bombardment applied during deposition [12]. A slight difference in the lattice constants of the fcc phases in Al-Cr-B-N (~4.14 Å) and $Al_{0.50}Ti_{0.50}N$ (~4.17 Å) results in the development of coherency strain at the interface [27], which contributes to the hardness increase of the multilayer structure. Moreover, the growth of crystallites is affected by the interfaces, which control the subsequent competitive growth conditions (see Fig. 3(b)). The hardness increase is thus related to the effect of reduced grain size according to the Hall-Petch relation as the growth of crystallites is limited across interfaces (see the development of the peak broadening in Fig. 1). On the other hand, the elastic properties are less affected by the presence of interfaces, giving rise to a reduction of the Young's modulus of Al-Ti-N/Al-Cr-B-N multilayers due to the lower stiffness of the Al-Ti-N layers.

The reduction of the residual compressive stress observed for Al-Ti-N/Al-Cr-B-N multilayers with respect to the Al-Cr-B-N single layer films (see Fig. 5) is ascribed to the combined effect of the stress level in the individual layers, the thickness of the

layers and the constitution of the interface [28, 29]. The decrease of residual compressive stress (σ_{tot}) in the Al-Cr-B-N layers is determined by the B content. As the volume fraction of the amorphous BN_x phase increases with rising B content, Al-Cr-(B)-N crystallites become completely encapsulated; thus compressive stress is reduced since defects effectively annihilate within the BN_x tissue (see Fig. 5 and [10]). The residual compressive stress in $Al_{0.50}Ti_{0.50}N$ single layer films having a thickness of ~3 µm is with $\sigma_{tot} \approx 0.50$ GPa also very low. Consequently, the combination of low-stressed Al-Ti-N and Al-Cr-B-N layers in a multilayer arrangement results in formation of films with low residual compressive stress state, which is even more reduced for an increased volume fraction of Al-Ti-N layers (see Fig. 5). In addition, the residual compressive stress in the multilayer films can be evidently further reduced by decreasing the thickness of the sublayers (see Fig. 5) [28]. The multilayer films denoted with “5 nm” are characterized by a large number of interfaces, as these films are grown under continuous evaporation of both sets of Al-Cr-B and Al-Ti targets. Since these interfaces offer the possibility of stress relaxation [11], very low stress values are obtained. On the other hand, also the multilayer films with thicker top layer (“Top”) show a reduced residual stress level. The reason for this behavior is found in the gradual development of the film microstructure, including nucleation, island growth, coalescence of islands, formation of a continuous structure and subsequent film growth [30]. In the early stages of single layer film growth, a fine-grained structure is formed, which subsequently coarsens due to competitive growth of the individual crystallites. This increase in grain size with increasing film thickness is accompanied by a reduction of average residual compressive stress of the whole multilayer coating [28], as observed for the “Top” layer (see Fig. 5).

The positive effect of the multilayer architecture on the mechanical properties of the Al-Cr-B-N films is also reflected in their tribological performance. In contrast to Al-Cr-B-N single layer films, the wear resistance is significantly enhanced in the Al-Ti-N/Al-Cr-B-N multilayer films (see Table 2 and Fig. 7(b)). The enhanced wear resistance is attributed to the increased hardness and reduced Young’s modulus [31] and stresses.

5 Conclusions

Al-Ti-N/Al-Cr-B-N multilayer films with Al-Cr-B-N and Al-Ti-N individual layer thicknesses varying from ~5 to ~180 nm and from ~5 to ~60 nm, respectively, were deposited by reactive cathodic arc evaporation via two-fold substrate rotation. The multilayer films exhibit exclusively fcc structure; film growth is associated with a loss of preferred (111) orientation for a decreasing thickness of the Al-Cr-B-N layers. The increased number of layers results in an increased hardness (up to 50 GPa) and reduced compressive stresses (as low as -250 MPa). With this combination of properties, Al-Ti-N/Al-Cr-B-N multilayer films reveal significantly improved wear performance in comparison to Al-Cr-B-N and commercially applied Al-Cr-N and Al-Ti-N single layer films.

Acknowledgements

The authors are grateful to Dr. Ilse Letovsky-Papst (Institute for Electron Microscopy and Fine Structure Research, FELMI Graz, Austria) for TEM investigations. The ERDA work has been supported by the European Community as an Integrating Activity ‘Support of Public and Industrial Research Using Ion Beam Technology (SPIRIT)’ under EC contract no. 227012. Financial support of the Christian Doppler Society is also highly acknowledged.

References

[1] D. McIntyre, J.E. Greene, G. Håkansson, J.-E. Sundgren, W.-D. Münz, J. Appl. Phys. 67 (3) (1990) 1542.

[2] M. Kawate, A. Kimura, T. Suzuki, J. Vac. Sci. Technol. A 20 (2) (2002) 569.

[3] R. Franz, B. Sartory, R. Kaindl, R. Tessadri, A. Reiter, V.H. Derflinger, P. Polcik, C. Mitterer, in G. Kneringer, P. Rödhammer, H. Wildner, eds., Proc. 16th Int. Plansee Seminar, Plansee, Reutte (A), Vol. 2, 2005, p. 932

[4] P.H. Mayrhofer, C. Mitterer, L. Hultman, H. Clemens, Prog. Mater Sci. 51 (2006) 1032.

[5] S. Vepřek, Thin Solid Films 317 (1998) 449.

[6] J. Patscheider, T. Zehnder, M. Diserens, Surf. Coat. Technol. 146-147 (2001) 201.

[7] M.A. Baker, S. Klose, C. Rebholz, A. Leyland, A. Matthews, Surf. Coat. Technol. 151-152 (2002) 338.

[8] J. Musil, Surf. Coat. Technol. 125 (2000) 322.

[9] S. Vepřek, M.G.J. Vepřek-Heijman, P. Karvankova, J. Prochazka, Thin Solid Films 476 (2005) 1.

[10] C. Tritremmel, R. Daniel, M. Lechthaler, H. Rudigier, P. Polcik, C. Mitterer, Surf. Coat. Technol. 213 (2012) 1.

[11] H. Holleck, V. Schier, Surf. Coat. Technol. 76-77 (1995) 328.

[12] H. Holleck, M. Lahres, P. Woll, Surf. Coat. Technol. 41 (1990) 179.

[13] P.E. Hovsepian, W.-D. Münz, Vacuum 69 (2003) 27.

[14] P.H. Mayrhofer, C. Mitterer, Surf. Coat. Technol. 133-134 (2000) 131.

[15] W.C. Oliver, G.M. Pharr, J. Mater. Res. 7 (1992) 1564.

[16] E. Rabinowicz, Friction and Wear of Materials, John Wiley & Sons, New York, 1964.

[17] R.L. Boxman, P.J. Martin, D.M. Sanders, Handbook of Vacuum Arc Science and Technology: Fundamentals and Applications, Noyes Publications, New Jersey, 1995.

[18] M. Kathrein, C. Michotte, M. Penoy, P. Polcik, C. Mitterer, Surf. Coat. Technol. 200 (2005) 1867.

[19] Powder Diffraction File (Card 00-025-1495 for fcc-AlN, Card 00-011-0065 for fcc-CrN), International Center for Powder Diffraction Data, ICDD, PDF-2/Release 2007, 2007.

[20] I. Petrov, P.B. Barna, L. Hultman, J.E. Greene, J. Vac. Sci. Technol. A 21 (5) (2003) 117.

[21] H. Willmann, P.H. Mayrhofer, P.O.Å. Persson, A.E. Reiter, L. Hultman, C. Mitterer, Scr. Mater. 54 (2006) 1847.

[22] A. Hörling, L. Hultman, M. Odén, J. Sjölén, L. Karlsson, Surf. Coat. Technol. 191 (2005) 384.

[23] K. Kutschej, P.H. Mayrhofer, M. Kathrein, P. Polcik, R. Tessadri, C. Mitterer, Surf. Coat. Technol. 200 (2005) 2358.

[24] J.S. Koehler, Phys. Rev. B 2 (2) (1970) 547.

[25] J. Lin, J.J. Moore, B. Mishra, M. Pinkas, W.D. Sproul, Surf. Coat. Technol. 204 (2009) 936.

[26] J.-E. Sundgren, J. Birch, G. Håkansson, L. Hultman, U. Helmersson, Thin Solid Films 193/194 (1990) 818.

[27] P.C. Yashar, W.D. Sproul, Vacuum 55 (1999) 179.

[28] R. Daniel, K.J. Martinschitz, J. Keckes, C. Mitterer, Acta Mater. 58 (2010) 2621.

[29] M.N. Popov, J. Spitaler, M. Mühlbacher, C. Walter, J. Keckes, C. Mitterer, C. Draxl, Phys. Rev. B 86 (2012) 205309.

[30] P.B. Barna, M. Adamik, Thin Solid Films 317 (1998) 27.

[31] A. Leyland, A. Matthews, Wear 246 (2000) 1.